Studies of Laser Ablation, Biodiagnostics, and new Laser Surgery Applications under Conditions of Ultrafast Desorption by Impulsive Vibrational Excitation (DIVE)

Dissertation

zur Erlangung des Doktorgrades
an der Fakultät für Mathematik, Informatik und Naturwissenschaften
Fachbereich Physik
der Universität Hamburg

vorgelegt von

Stephanie Maier

aus München

Hamburg
2017

Gutachter der Dissertation:	Prof. Dr. R. J. Dwayne Miller Prof. Dr. Florian Grüner
Zusammensetzung der Prüfungskommission:	Prof. Dr. R. J. Dwayne Miller Prof. Dr. Florian Grüner Prof. Dr. Heinrich Schwoerer Prof. Dr. Arwen R. Pearson Prof. Dr. Sven-Olaf Moch
Vorsitzender der Prüfungskommission:	Prof. Dr. Sven-Olaf Moch
Datum der Disputation:	19. Februar 2018
Vorsitzender Fach-Promotionsausschusses Physik:	Prof. Dr. Wolfgang Hansen
Leiter des Fachbereichs Physik:	Prof. Dr. Michael Potthoff
Dekan der Fakultät für Mathematik, Informatik und Naturwissenschaften:	Prof. Dr. Heinrich Graener

Abstract

Minimal invasive procedures are becoming increasingly important for numerous surgical disciplines. Medical lasers contribute to this development providing a high precision and intrinsic sterility, and are therefore the tool of choice for many applications. In addition, laser-based systems offer additional advantages for real-time bio-diagnostics when coupled with mass spectrometry.

Ultrafast Desorption by Impulsive Vibrational Excitation (DIVE) is a recently developed, ultra-soft laser ablation mechanism with promising medical and bio-diagnostic applications. In the DIVE-regime a Picosecond Infrared Laser (PIRL) is used to ablate tissue. The PIRL selectively excites the vibrational modes of water molecules in tissue within only a few picoseconds and thus drives an ultrafast transition from the liquid to the gaseous phase. This enables a rapid ablation process avoiding thermal and shock wave induced collateral damage to the surrounding tissue. In particular, the soft ablation process extracts tissue constituents, such as small molecules, proteins and protein complexes, undamaged and with intact biological functions.

This thesis describes laser ablation characterization studies, bio-diagnostic techniques, and new laser surgery applications using the DIVE regime. The cutting speed is a critical parameter for the acceptance of a new surgical method in clinical daily routine. Therefore, the ablation rates and ablations depths as a function of PIRL peak fluence are studied for different soft tissues. Furthermore, limitations of future PIRL laser designs due to laser-induced optical breakdown in the ablated tissue are analyzed. A new surgical laser scalpel concept utilizing a tapered fibre tip is developed and compared to incisions performed by a classical scalpel. Further investigations within this work compare the efficiency of two laser ablation methods with infrared lasers of different pulse durations and comparisons are made for proteome analysis. Finally, two new PIRL-based surgical techniques are presented which treat otosclerosis in otorhinolaryngology and glaucoma in ophthalmology.

Overall, the results demonstrate the substantial benefits of the DIVE process compared to conventional laser ablation techniques and emphasize the unique characteristics of the PIRL laser. These capabilities further distinguish PIRL as a valuable tool for surgical laser applications and bio-diagnostics in the near future.

Zusammenfassung

Minimal-invasive Verfahren gewinnen zunehmend an Bedeutung in zahlreichen chirurgischen Fachdisziplinen. Aufgrund ihrer hohen Präzision und ihrer inhärenten Sterilität sind medizinische Laser für einige dieser Anwendungen das Werkzeug der Wahl. Darüber hinaus können laserbasierte Systeme in Verbindung mit der Massenspektrometrie zusätzliche Vorteile für die Echtzeit-Biodiagnostik bieten.

Ultraschnelle Desorption durch impulsive Anregung von Vibrationsmoden (DIVE) ist ein neu entwickelter und besonders schonender Laserablationsmechanismus, mit vielversprechenden Anwendungen in der Medizin und Biodiagnostik. Ein Pikosekunden-Infrarot-Laser (PIRL) wird zum Abtragen von Gewebe innerhalb des DIVE-Regimes eingesetzt. Der PIRL regt die Schwingungsmoden von Wassermolekülen im Gewebe innerhalb weniger Pikosekunden selektiv an und treibt so einen ultraschnellen Übergang von der flüssigen in die gasförmige Phase an. Dies ermöglicht einen schnellen Ablationsprozess, der Kollateralschäden im umgebenden Gewebe durch thermische Effekte und Stoßwellenausbreitung vermeidet. Entscheidend ist dabei, dass durch den sanften Ablationsprozess Gewebebestandteile wie kleine Moleküle, Proteine und Proteinkomplexe unbeschädigt und mit intakten biologischen Funktionen extrahiert werden.

Die vorliegende Arbeit umfasst mehrere Studien zur Charakterisierung der Laserablation, Biodiagnostik, und neuen chirurgischen Laseranwendungen unter Verwendung des DIVE- Ablationsmechanismus. Für die Akzeptanz neuer chirurgischer Methoden im klinischen Alltag ist die Schneidegeschwindigkeit von erheblicher Bedeutung. Die Arbeit untersucht deshalb Ablationsraten und Ablationstiefen für den Pikosekunden-Infrarot-Laser in verschiedenen Weichgeweben in Abhängigkeit von der Laser-Fluenz. Des Weiteren werden die Grenzen zukünftiger PIRL-Laserdesigns hinsichtlich einer laser-induzierten optischen Plasmabildung im abgetragenen Gewebe analysiert. Ein neues Konzept für ein chirurgisches Laser-Skalpell mit einer abgeschrägten Faserspitze wird entwickelt und mit den Inzisionen eines klassischen Skalpells verglichen. In weiteren Untersuchungen wird die Effizienz zweier Laserablationsmethoden mit Infrarotlasern unterschiedlicher Pulsdauern verglichen und Unterschiede im Hinblick auf eine Proteinanalyse dargestellt. Schließlich werden zwei neue Operationstechniken mit PIRL zur Behandlung von Otosklerose in der Hals-Nasen-Ohren-Heilkunde und Glaukom in der Augenheilkunde vorgestellt.

Zusammenfassend zeigen die Ergebnisse dieser Arbeit die erheblichen Vorteile des DIVE-Prozesses gegenüber herkömmlichen Laserablationsmethoden und betonen die einzigartigen Eigenschaften des Pikosekunden-Infrarot-Lasers (PIRL). Diese Besonderheiten zeichnen PIRL als ein wertvolles Werkzeug für chirurgische Laseranwendung und Biodiagnostik in der Zukunft aus.

Contents

1. Introduction and Relevant Literature

1.1. Overview of Medical Laser Applications

Despite the enormous developments since the realization of the first laser in 1960 by Maiman, the laser has not lived up its promise to replace mechanical surgical tools such as scalpels or electrosurgical devices. One reason might be the excessive collateral damage induced to tissue through a number of different mechanisms. There is still great motivation to develop lasers with characteristics that minimize collateral tissue damage as mechanical tools suffer from limited precision in comparison to the theoretical limits for laser cutting. As well, the diverse array of cold and hot surgical instruments cause different forms of extended tissue damage due to induced shear stress, shockwave formation and thermal injury [1, 2]. In spite of their theoretical advantages in terms of single cell precision, intrinsic sterility, and in many cases their hemostatic characteristics [3], lasers are only suitable for a limited number of medical procedures in daily clinical use. One reason for this is attributed to the fact that most available medical lasers do not achieve a cutting precision at the level of a single cell. Considerable collateral damage to the adjacent tissue originating from thermal and acoustic effects, and shock wave propagation significantly decreases the cutting accuracy. Currently only femtosecond lasers reach this degree of precision and exceed current mechanical instruments, however they have the disadvantage of creating a high ionizing environment in the surgical zone [4].

Nevertheless, many useful therapeutic laser techniques have been clinically established in a broad range of medical fields such as otorhinolaryngology, gynecology, urology, dental surgery, neurosurgery, orthopedics, dermatology, ophthalmology, angioplasty, and cardiovascular surgery. For the sake of completeness, it should also be mentioned, in addition to therapeutic laser treatments many successful diagnostic laser techniques exist such as confocal laser microscopy and optical coherence tomography.

Although new laser techniques are now rapidly developed in numerous medical fields, for decades the dominating medical field with the most successful laser applications

has been ophthalmology [5]. Particularly important surgical procedures in this field are refractive corneal surgery and the treatment of glaucoma or cataracts. In refractive corneal surgery the vision is corrected by reshaping the curvature of cornea. The term glaucoma summarizes eye diseases damaging the optical nerve, whereby most cases go back to an increased pressure inside the eye. In glaucoma laser treatment, blocked canals are opened or new openings are created to lower the intraocular pressure. Cataract is characterized by a turbidity of the lens and is treated by replacing the lens by an artificial lens implant. Femtosecond lasers are applied to open the lens capsule and fragment the lens for removal [6]. Also in dermatology, the laser became an invaluable tool for a broad range of applications like removing port wine stains by applying argon lasers in the visible spectrum [7]. In dental applications, the Er:YAG laser has shown potential as a useful tool for caries therapy [8]. The CO_2 laser is the standard laser in gynecology as well as otorhinolaryngology and used for multiple applications. However, these different laser applications are all limited in scope due to shock waves or plasma formation with inherent health risks of ionizing radiation. Laser applications are also found in tumor treatments such as photodynamic therapy (PDT) and laser-induced interstitial thermotherapy (LITT). In photodynamic therapy (PDT) a photosensitizer is injected into the bloodstream or directly applied to skin and accumulates over time preferentially in tumor cells as compared to healthy cells. Via light activation of the photo-sensitizing agent, toxic substances are created to trigger cell necrosis [9]. Laser-induced interstitial thermotherapy (LITT) is a minimally invasive surgery method, where the tumor tissue is heated via laser light typically provided by a Nd:YAG laser to above 60°C to denature the proteins and coagulate the tissue.

In several disciplines of surgery, minimally invasive procedures gain increasing importance. The Picosecond Infrared Laser (PIRL) is a promising tool for minimally invasive surgery due to the lack of collateral damage to the adjacent tissue. This results in a minimal damage of the extracellular matrix morphology and leads to healing with no visible scar tissue formation to the naked eye at the incision [39, 47]. This single attribute is important as it is scar tissue formation that generally adversely effects all surgeries to some extent. In addition, the picosecond time regime is long enough to avoid ionization of the tissue, which ensures there is no creation of toxic free radicals or the fragmentation of constituent proteins as is the case for femtosecond lasers. These properties make the PIRL an interesting tool for real-time bio-diagnostics by means of mass spectrometry to analyze the ablated tissue during laser surgery.

1.2. Thesis Structure

This thesis is organized as follows:

Chapter 2 presents ablation rates and depths for the PIRL in different soft tissues like cornea, skin and liver depending on Gaussian beam peak fluence. The obtained ablation rates are compared to other surgical laser systems.

Chapter 3 describes a new surgical laser scalpel with a tapered fiber tip.

Chapter 4 compares and discusses the efficiency of two infrared laser ablation methods with different pulse durations for proteome analysis.

Chapter 5 presents two new applications techniques for the PIRL in otorhinolaryngology and ophthalmology.

Chapter 6 concludes the results of this dissertation and gives an outlook.

1.3. Laser Tissue Interactions

When laser light is applied to biological tissue, various interaction mechanisms are present that depend on the applied power density, exposure time, and the tissue properties. The therapeutic laser-tissue interactions can be divided into the following categories [5]: Photochemical interactions, thermal interactions, photoablation, plasma-induced ablation, and photodisruption.

For the interaction of pulsed lasers with tissue the laser pulse duration, as well as the thermal and acoustic relaxation time of the tissue play a crucial role. The thermal relaxation time is:

$$\tau_{\text{therm}} = \frac{\delta^2}{4X}, \tag{1.1}$$

where δ is the optical penetration depth or absorption length and X the thermal diffusivity [10]. To minimize the thermal damage to near zero, the laser pulse duration should be smaller than the thermal relaxation time of the irradiated tissue [11]. This ensures that the temperature increase is almost confined to the irradiated tissue volume absorbing the optical power and that the resulting diffusion length is actually smaller than the penetration depth [5, 12].

The thermal relaxation time of water, the main component of most tissues, is ∼1 µs [5] close to the absorption peak at $\lambda = 3$ µm. Water has the highest absorption coefficient of all tissue constituents for $\lambda \sim 3$µm. Thus, typical thermal relaxation times in tissue are on the order of several microseconds at $\lambda = 3$ µm [13].

The acoustic relaxation time is [14]

$$\tau_{ac} = \frac{\delta}{v_s} \tag{1.2}$$

where v_s is the speed of sound. If the laser pulse duration is shorter that the acoustic relaxation time, stress confinement within the irradiated volume is reached. In this case, the tissue is heated faster than the stress wave propagates from the heated volume to the surrounding tissue. The stress wave is released by the ablation process and the adjacent tissue remains undamaged [15]. Using eq. 1.2, the acoustic relaxation time for $\lambda = 3$ µm in water of 37°C is half a nanosecond for $\delta = 1$ µm and $v_s = 1423.93$ m/s [16].

The speed of sound in tissue correlates with the water and collagen content. It is largely wavelength independent [17]. For example, the speed of sound in different parts of the eye varies between 1481 m/s and 1680 m/s [18] depending on the tissue composition. Thus, the 1 µabsorption depth of water can serve as a lower limit of the

acoustic relaxation time in eye tissue. With an average speed of sound of 1600 m/s in eye tissue, the minimal acoustic relaxation time is half a nanosecond for a wavelength of $\lambda = 3$ µm.

Photochemical interactions can be observed at relatively low power densities with less than 50 W/cm^2 and exposure times longer than 1s [5]. A typical application for this type of interaction is the already mentioned photodynamic therapy. Furthermore, a relatively new technique called optogenetics has obtained a great deal of attention in the last decade promising not only insights into brain structure and function, but also new promises regarding neurological therapeutic applications like treating chronic pain [19]. Optogenetics enables the modification of cellular behavior by illuminating light-sensitive proteins [20]. What these photochemical interactions have in common is that via light, certain molecules in the tissue are excited, to initiate specific chemical reactions within their environment.

Thermal interaction can be subdivided in numerous thermal effects like coagulation, vaporization, carbonization and melting. On the microscopic scale, all these thermal effects are two step-processes transferring the photon energy to kinetic energy of tissue molecules. The first step involves the absorption of photon energy leading to excited vibrational and rotational states of the absorbing molecule. By inelastic collisions the internal energy of the excited molecule is transferred to neighboring molecules [21]. Coagulation occurs above 60°C and proteins lose their three-dimensional structure. This process, also called denaturation, leads to necrotic tissue [5]. Under atmospheric pressure water molecules undergo a liquid-gas phase transition at 100°C, namely vaporization, and largely expand their volume. The conversion of organic material to carbonaceous substances by breaking organic molecules into simple matter is called carbonization and can be observed above 200°C as a thin carbon layer on the tissue [22]. Melting is the phase transition from solid to liquid and the melting point can strongly vary within different materials. As an example, enamel in dental tissue begins to melt at a temperature above 700°C [23]. For thermal interactions, the pulse durations are within the range of 1 µs up to 1 min, hence mostly longer than the thermal relaxation time of tissue. Usual power densities are 10 to 10^6 W/cm^2 and typical applications are laser-induced interstitial thermotherapy (LITT) or tissue cutting with a CO_2 laser [5].

In *Photoablation*, tissue is removed via UV light by breaking chemical bonds in the tissue, as the single photon energy of the applied laser light exceeds the dissociation energy of most molecular bonds in the irradiated volume. To understand the mechanism, Srinivasan studied the process in organic material depending on the energy density, also called fluence [24]. Beyond a certain threshold fluence, sufficient bonds per time in the tissue are cleaved to start the ablation process. As a consequence, the volume

of the irradiated material needs more space due to the accumulation of fragments and the excess energy after the bond cleavage is transferred to vibrational, rotationally and transitionally modes of the fragments [24]. UV light is strongly absorbed in biomolecules and consequently the absorption depths are around several micrometers [21]. Typical power densities range from 10^7 to 10^{10} W/cm^2 and pulse durations were within the nanosecond time domain [5]. Due to the short pulse duration, thermal damage is avoided and a very precise cutting process is attained. However, shockwave formation occurs in the adjacent tissue, but can be tolerated in certain applications. An example for this interaction mechanism is refractive corneal surgery with an excimer laser requiring a high level of precision. Another drawback of photoablation is the absorption of UV light by DNA causing mutagenic and carcinogenic effects in tissue [25].

One of the most important mechanisms for ultrashort laser pulse tissue interaction is *Plasma-induced Ablation* at pulse lengths from 100 femtoseconds to 500 picoseconds [5]. Typical power values for plasma-induced ablation are between 10^{11} to 10^{13} W/cm^2. For plasma-induced ablation with a femtosecond laser, no thermal coupling occurs outside of the ablation site, since the laser pulses are too short [26]. During this interaction, the atoms and molecules in the tissue are ionized. This occurs for instance, when the electrical field strength of the radiation exceeds the required one to remove electrons in atoms or molecules. This leads to dielectric breakdown, also called laser-induced optical breakdown (LIOB) in this context [15]. The threshold for laser-induced optical breakdown (LIOB) decreases significantly with shorter laser pulses [27] and lower pulse energies are necessary for ablation. The ionization can be initiated by q-switched or mode locked laser pulses. In case of q-switching, thermal ionization causes plasma formation, while with mode-locked laser pulses a number of photons are necessary for the initial ionization, namely multi-photon ionization [28]. The free electrons are strongly accelerated by absorbed photons and collide with other atoms creating more free electrons also known as avalanche effect. The plasma formation leads to tissue evaporation, cutting with a high precision and minimal collateral damage. The ablation mechanism is also applied in refractive corneal surgery using a femtosecond laser with a wavelength of 1053 nm to create the necessary flap for this procedure [29].

Photodisruption is also based on plasma formation, but utilizes predominately the mechanical effect of the emerging shockwaves and cavitation bubble formation caused by plasma expansion due to a rapid temperature rise during the breakdown. The propagation distance of shockwaves and the diameter of the cavitation bubbles rise with longer pulse durations and higher pulse energies [26]. Plasma formation is spatially confined to the excited volume, whereas the resulting shockwaves and cavitation bubbles propagate far into the adjacent tissue. When the cavitation bubbles collapse, so

called high-speed liquid jets are formed [30]. Cavitation bubbles cause macroscopic tissue damage, while shockwaves are mainly responsible for intracellular damages such as the rupture of cellular membranes and defects in cell organelles [31]. The power densities for photodisruption are higher than for plasma-induced ablation and extend to 10^{16} W/cm^2 [5]. Typical pulse durations are femtosecond to microseconds, although with longer pulse durations strong shockwaves are produced, e.g. for achieving stone fragmentation within the human body. A typical application is laser lithotripsy, where the laser light is guided via an optical fibre into the body to fragment urinary and biliary stones.

1.4. Introduction to Desorption by Impulsive Vibrational Excitation (DIVE)

Liquid water consists of a very complex network of H_2O molecules connected via fluctuating hydrogen bonds. The hydrogen bonds continuously break on the time scale of femtoseconds and reorganize within several picoseconds [32]. The efficient intermolecular energy redistributions of the OH-stretch vibration modes over numerous water molecules occurs within 50 fs and hence faster than the average hydrogen bond lifetimes. On a timescale of 200 fs the vibrational stretching modes are efficiently coupled into librational motions and directly to the O-O acoustic like motions [33]. The latter are translational motions, the very motions involved in driving ablation. The increased nuclear motions in terms of OH-stretch vibrations and librations weaken the hydrogens bonds. Furthermore, the vibrational energy is also transferred to intramolecular bending vibrations besides librational motions breaking hydrogen bonds and delocalizing the energy intermolecularly within 1ps [34]. Depending on the temperature, the OH-stretch thermalization time, τ_{th}, can last for several picoseconds [35]. Water is unique in that through the extremely strong anharmonic coupling of vibrational modes via the hydrogen bond interactions, it is possible to effectively and directly transduce absorbed photon energy in the form of vibrational energy to translational motions.

Moreover, liquid water possesses not only the fastest vibrational relaxation times known in biological materials, but also a high absorption coefficient allowing impulsive superheating [36]. Compared to a normal boiling process, liquid water is driven to a gaseous state in superheating without the formation of vapor bubbles. Since the vibrational relaxation processes and the coupling to librational motions are faster than the nucleation growth, the resulting formation of bubbles is avoided. During this thermodynamic change of state due to vibrational thermalization in the hydrogen bond network, temperatures can be as high as 2000°C within the excited volume.

According to Franjic and Miller [36], the impulsive limit is defined as a condition, in which the laser pulse duration, τ_p, is at least as long as the thermalization time of the vibrational states and shorter than the thermal, τ_{therm}, or acoustic, τ_{ac}, relaxation times in the irradiated tissue volume. This impulsive superheating ensures a rapid phase transition from liquid to gas and enables a very efficient tissue ablation process termed *Desorption by impulsive vibrational excitation (DIVE)* .

The Picosecond Infrared Laser (PIRL) with a wavelength around 3 µm is tuned to the intramolecular symmetric and asymmetric OH-stretching vibrations within liquid water, the main component in tissue. The pulse duration of the PIRL is on the picosecond time scale and fulfills the conditions for impulsive superheating as it is long enough to excite the vibrational modes, but it is also short enough to achieve thermal and stress confinement within the irradiated volume. This is in contrast to the nanosecond timescale that allows unarrested nucleation growth, forming bubbles, cavitation, and ensuing shock waves [37]. In the picosecond timescale not only the collateral damage of the surrounding tissue in terms of thermal effects and shock wave propagation is avoided, but also a very efficient ablation process occurs without energy leaking outside the excited volume. The applied optical energy moves out of the irradiated volume within the emerging ablation plume.

Inside the ablation volume, inhomogeneous stress fields arise due to the impulsively generated heat during the DIVE process [13]. The thermoelastic stress is created on the same picosecond time scale as the photon energy is thermalized, and GHz acoustic transients occur. With higher frequencies the acoustic transients are more attenuated in tissue and the created shockwaves are strongly weakened within a few micrometers. The inhomogeneity of the stress field results from an irregular distribution of vibrationally absorbing chromophores inside the tissue. In comparison, the emerging plasma in plasma-mediated ablation creates an uniform acoustic shockwave front, because of a loss of material structure initiated by the optical break down. As a result of the non-uniform thermoelastic stress field, photo-mechanical effects in the tissue appear. These effects contribute to the ablation process and reduce in consequence the ablation threshold.

Within the DIVE regime, optical energy is converted into heat causing the material ablation as a result of the thermally induced ultrafast phase transition. Thus the DIVE process can be most likely assigned to the thermal tissue interaction mechanisms, even if its short pulse durations and high power densities. Electronic excitations are completely avoided resulting in no unwanted chemical bond breaking, which causes cell damage as in the case of photo ablation.

Due to the very fast volume expansion in consequence of the DIVE process, the ablation itself is accompanied by rapid adiabatic cooling. Thus the time period during which the

biomolecules are exposed to high temperatures is considerable reduced. This strongly reduces thermal effects regarding modifications of molecules in the ablation plume. The extraction of intact biological material with conserved function via PIRL was demonstrated with viruses and yeast cells [38]. Specifically, the morphologic structure of a tobacco mosaic virus was analyzed via transmission electron microscope (TEM) for a non-ablated control and an ablated sample collected directly from the ablation plume. Comparing the two samples, no significant differences in the length of viral filaments were found. Additionally, the virulence of the tobacco mosaic virus in the ablation plume was tested by inoculating tobacco leaves with the collected virus. After incubation, the leaves showed clear signs of infections in the form of local lesions, whereby the intact function of the virus was demonstrated. Yeast cells, more precisely *S. cerevisiae* cells, were ablated from a frozen aqueous suspension and directly collected from the ablation plume. Confocal microscope pictures revealed that 70 % of the ablated cells showed equal shape and size compared to the non-ablated viable cells. Cultured on a growth medium, the ablated cells developed new colonies, demonstrating the viability following PIRL ablation.

1.5. Applications of DIVE in Surgery

The DIVE process was for the first time successfully applied to a medical application by Amini-Nik *et al.* in 2010 [39]. In mice, the wound healing of PIRL incisions was compared to cuts induced by a conventional medical Er:YAG laser with microsecond pulse durations and mechanical surgical tools. The widths of scars resulting from PIRL incisions were significantly smaller in contrast to the scars produced by other surgical modalities. In scars created by PIRL incisions, lower concentrations of messenger molecules, which are responsible for cell proliferation, were found in immunohistological studies. This shows the minimal invasive character of the PIRL ablation. The minimal damage to adjacent tissue was also visible by transmission and scanning microscope imaging. Due to the gentle ablation mechanism of PIRL, sharp edges with intact adjacent tissue and undamaged collagen layers were observable at the PIRL cuts.

In a laryngeal surgery trial, multiple cuts were made *ex vivo* by PIRL and a carbon dioxide (CO_2) laser in the laryngeal epithelium, epithelial connective tissue, and cartilage tissue [40]. For early stage larynx tumors, the CO_2 laser represents the gold standard of laser therapy. The PIRL featured a superior cutting precision and significantly reduced thermal collateral damage in the order of 10 µm in contrast to the CO_2 laser. In a second *ex vivo* study in human laryngeal tissue, the superiority of the PIRL in comparison to a CO_2 and an additional Er:YAG laser was reaffirmed [41]. The CO_2

and Er:YAG lasers were operated at typical settings for clinical usage. The cutting gaps of PIRL incisions were significantly narrower with smaller damage zones. Environmental scanning electron microscopy (ESEM) images revealed once again intact collagen fibres at PIRL cutting edges. In comparison, CO_2 and Er:YAG laser incisions exhibit considerable carbonization and melting of tissue. Via infrared thermography (IRT) the median temperature rise during cutting was measured for PIRL and Er:YAG laser cuts. For PIRL a temperature increase in the ablation zone of only $\delta T = 4$ K was calculated over a 10-ms interval in contrast to Er:YAG laser with $\delta T = 172$ K. However, these values should be considered with caution, since the theoretical temperature rise on the picosecond timescale should be in the range of 1000°C and the measuring frequency of the thermal camera was too slow. The point is that even so the time scale for such an elevated temperature is too short to lead to thermally activated damage as evident by absence of any collateral damage and ablation of entire proteins with intact biological functions.

Moreover, PIRL is an ideal tool for phonomicrosurgical procedures at vocal folds, since the PIRL reduces considerable the formation of scars. Scarring at vocal folds results in rigidity and stiffness of tissue, changing the vibrational characteristics and therefore the voice of patients. In *ex vivo* human vocal folds PIRL incisions were compared via histological evaluation in terms of HE staining and ESEM analysis to cuts made by a scalpel and CO_2 laser [42]. The PIRL showed smaller zones of tissue destruction compared to the standard tools and enabled an almost atraumatic laser application.

In ophthalmology, the first proof-of-principle experiments using the PIRL for corneal incisions were conducted in porcine eyes [43, 44]. The femtosecond laser, though well established in ophthalmology, did not become widely accepted in cornea transplantation due to a lack of improved outcome. With respect to mechanically guided transplantation of corneal material, no improvement in terms of astigmatism and visual outcome was found. As well, the femtosecond laser is limited in terms of cutting scarred tissue. The excimer laser was also not successful in clinical applications, because of various reasons such as a relative low cutting speed within the transplantation procedure. A reduced collateral tissue damage and contact-free laser cutting can improve the laser acceptance in cornea transplantation. In histological images, thermal effects were only observable in the first cell layer adjacent to the PIRL incision. Confocal laser scanning microscope (CLSM) and ESEM images revealed very precise cutting edges in corneal tissue. With PIRL contact-free deep penetrating cornea cuts were realized, avoiding the adverse flattening of the corneal geometry due to necessary docking systems with liquid interfaces in case of femtosecond lasers.

In *ex vivo* porcine skin, the heat generation within the ablation zone was also measured with a thermography camera for the PIRL and a conventional Er:YAG laser [45].

For PIRL the mean temperature rise in the ablation site was $\delta T = 1.7$ K and the maximum peak rise $\delta T = 2.1$ K in skin surface. For the Er:YAG laser, the values were $\delta T = 15.0$ K and $\delta T = 18.9$ K, respectively.

In a further study, bone ablation was compared by infrared thermography, ESEM, and histology for an Er:YAG laser and PIRL [46]. For these experiments, circular areas were ablated in *ex vivo* chicken bone. Morphological micro-structures such as canals for blood vessels and nerves were preserved within the PIRL incision after ablation and clearly visible in ESEM images. By contrast, the Er:YAG laser ablation revealed diffuse thermal injury in the incision zone. In histology, the thermal injury is clearly visible for the Er:YAG laser incisions, whereas in case of PIRL no obvious visible change of mineralized matrix was noted. The peak temperature rise in the bone surface was $\delta T = 1.6$ K for PIRL experiments and $\delta T = 13$ K for the Er:YAG laser procedures.

In an important comparative wound healing study with live rats, three different cutting mechanisms were compared [47]. Full-thickness cuts through all skin layers with a length of 1 cm were performed by the PIRL, a conventional electrosurgical device and a scalpel. After 21 days, all wounds were photo-documented and analyzed. Compared to the other two incision methods, the PIRL incisions showed no visible scarring to the naked eye. After staining the tissue, both width and area of the scarred tissue resulting from the full thickness cuts were determined. The scar area caused by PIRL incisions was 1.5 times smaller than the scar area of the scalpel incisions and 3.7 times smaller than the ones performed by the electrosurgical device.

1.6. DIVE in Combination with Mass Spectrometry

Mass spectrometry (MS) is an exceptional analytical method due to its sensitivity, detection limits, and broad application range in many disciplines such as physics, geology, medicine and many more. Especially in fields like proteomics, lipidomics, and metabolics, mass spectrometry became an invaluable tool in the last decades [48]. In addition, it is a promising method for near real-time tissue identification within operation theaters in the near future.

In order to analyze inorganic or organic compounds, in mass spectrometry the sample is usually transferred into the gas phase and ionized. In the next step, the ions are accelerated in an electrical field and separated by their mass-to-charge ratio. A typical mass spectrometer consists of an ion source, a mass analyzer, and a detector. Typically the choice of ionization techniques depends on the substance class of the analytes, whereas the quality and reliability of the analysis are defined by the combination of mass analyzer and detector [49].

The ionizing techniques can be categorized as soft and hard ionization depending on the fragmentation degree of the analyte [50]. A soft ionization technique at atmospheric pressure is Electrospray Ionization (ESI). This method is particularly suitable for the ionization of large polar biomolecules such as proteins [51]. In ESI, the analyte is diluted within a solvent at low concentrations and transferred into the gas phase through nebulization. Another prominent soft ionization method for complex biomolecules is matrix-assisted laser desorption/ionization (MALDI). With this method, the analyte is embedded in a matrix, which absorbs the laser light. As a result the energy is transferred to the matrix molecules, while the analytic molecules are preserved from decomposition during the ablation process [52]. Typically UV-lasers coupling to the electronic states of the matrix molecules or IR-lasers exciting vibrational modes are employed for MALDI. The pulse durations are normally in the nanosecond range to avoid thermal effects. In combination with these two ionizing techniques, a time-of-flight mass spectrometer (TOF-MS) is often used in biomedical applications. To analyze the mass of the ions, a packet of ions is accelerated by a defined electric field. The potential energy depending only of the charge of the ions is thereby converted into kinetic energy. By measuring the time until the ions reach the detector, the velocity of the ions is determined. The velocity correlates directly with the mass-to-charge ratio (m/z) of the accelerated molecules. Various mass spectrometers with more complex mass analyses systems exist, even able to run several rounds of mass spectrometry, also called tandem mass spectrometers. One of the more complex mass analyzers is an ion trap mass analyzer, also called the Orbitrap. In this device, the ions are trapped in an orbit around a central spindle shaped electrode surrounded by outer electrodes. By applying a voltage between the inner and outer electrodes, a radial electric field attracts the ions in direction to the inner electrode. The opposite force results from the tangential velocity in the form of the central force and depends on the ion mass. The ion trajectories are recorded and via Fourier transformation of the frequency signal, the mass-to-charge ratio is determined [49].

In the last decades mass spectrometry successfully entered clinical laboratories and advanced medical science. In particular, its high specificity and sensitivity clearly exceed other methods based on spectrophotometry, potentiometry or immunoassays [53]. The broad spectrum of clinical applications ranges from drug screening, toxicology studies to *in-vitro*-diagnosis of metabolic disorders [54]. Especially liquid chromatography-tandem mass spectrometry (LC-MS), Gas chromatography–mass spectrometer (GC-MS) and MALDI-TOF play a vital role in clinical applications.

Over time mass spectrometry evolved from analyzing extracted and purified samples to entire tissue samples [55]. New imaging techniques based on mass spectrometry were established, enabling the spatial visualization of chemical compounds in the sample. In biological and clinical applications this technique is very valuable, since the spa-

tially resolved molecular information can be associated with anatomical structures or pathological alterations. A successful technique in this field is MALDI imaging mass spectrometry (MALDI-IMS). The distribution of hundreds of unknown compounds can be identified in a single measurement via MALDI-IMS [56]. For mass spectrometry imaging the laser ablation can also be combined with subsequent Electrospray Ionization, namely LAESI-MS imaging.

Significant efforts utilizing distinct technical approaches have been undertaken to achieve the ultimate goal in cancer surgery of real-time *in vivo* tissue identification directly in the operating theater. This advance would allow much more precise cancer tissue removal with tumor free margins, lowering the risk for local tumor recurrence. Valuable time would be saved compared to elaborate histological investigations to identify tumor margins and cancer cell types. In the context of tissue recognition techniques, it is worth mentioning also further spectroscopic methods such as fluorescence, IR absorption and Raman spectroscopy. In brain tissue, fluorescence-guided surgery with 5-aminolevulinic acid already showed improved resections of contrast-enhanced brain tumors compared to conventional microsurgery guided by white light [57]. Since Raman spectroscopy allows to analyze tissue samples with regard to its chemical composition by monitoring molecular vibrations, it is also an interesting candidate for tissue identification. However, conventional Raman spectroscopy is too time-consuming and thus for image-guided surgery inapplicable.

New approaches to overcome the limitations of Raman spectroscopy have focused on using a nonlinear technique called coherent anti-Stokes Raman scattering (CARS) [58] and combining it with further nonlinear microscopy techniques. An interesting multimodal nonlinear imaging approach for tissue identification with sub-cellular spatial resolution is the combination of CARS, second-harmonic generation (SHG) microscopy, and 2-photon exited fluorescence (TREF) supplemented by advanced image processing algorithms [59]. In contrast to the fluorescence based method with 5-aminolevulinic acid, this method is label-free. Multimodal nonlinear imaging was tested in head and neck cell carcinoma as well as brain tumors and showed a sufficient chemical contrast for cancer imaging [60, 61]. The method was able to visualize the morphology and lipid distribution within the tissue.

However, fluorescence-guided surgeries with 5-aminolevulinic acid as well as multimodal nonlinear imaging lack the possibility of tumor typing. This enables the determination of original cancer cell types. The fluorescence labeling is not specific enough to differentiate between different cancer cell types. Multimodal nonlinear imaging and other imaging techniques like magnetic resonance imaging (MRI) and positron emissions tomography (PET) are also not capable of achieving the necessary specificity [61]. Only Infrared (IR) and Raman spectrometry can distinguish between different cancer

tissues, but face strong limitations regarding spatial resolution down to the cellular level, and efficiency.

First attempts using mass spectrometry in *ex vivo* and intra-operative cancer tissue identification have been undertaken by Balog *et al.* in 2013 [62]. In this study, an electrosurgical hand-piece is combined with a mass spectrometer, analyzing the emerging aerosol during dissection. The mass spectrometry analysis was focused on lipidomic profiles, especially various phospholipids with a molecular weight less than 1 kDa. By developing a database, the lipid profiles from the resected tissue can be categorized in near real-time into healthy and cancerous tissue. Moreover, additional *ex vivo* analyses of other samples demonstrated the huge potential of mass spectrometry to distinguish between primary and metastatic tumors. The obtained spectra were unique for each cancer type allowing even to identify the origin of metastatic tumors.

A further attempt of real-time tissue analysis via mass spectrometry *in vivo* was undertaken by Fatou *et al.* in 2016 [55]. For the first time a *in vivo* real-time analysis based on laser ablation and mass spectrometry was realized. The device consisted of an optical parametric oscillator (OPO) pumped by a Nd:YAG laser emitting nanosecond laser pulses with a wavelength around 3 µm and an ion trap mass analyzer. The ionization of analytes was implemented by *in-situ* gas phase ion production under laser ablation. No further ionization method was necessary to detect sufficient gas phase ions. Human skin samples were ablated and subsequently transferred to the mass spectrometer within a few milliseconds. The lipid molecular profiles were utilized to distinguish between male and female test persons. Further, distinct differences were measurable before and after pharmacological treatments with a drug or cosmetic treatments such as applying moisturizing hand cream in skin samples.

In a new concept, a handheld mass spectrometry system was developed for noninvasive *ex vivo* and *in vivo* cancer diagnosis in tissues [63]. A so-called MassSpec Pen delivered single water droplets on the tissue specimens to extract biomolecules and subsequently analyze these via mass spectrometry. In the mass spectra, potential cancer biomarkers were determined from metabolites, lipids and proteins. Benign and malignant thyroid tumors, and lung cancer were detected with an overall prediction accuracy of 96,3 %.

Since proteins and peptides work as diagnostic markers besides lipids in disease identification [64], DIVE mass spectrometry was tested to analyze both protein and lipid profiles in various tissues. In 2015, Kwiatkowski *et al.* showed that via DIVE ablation the necessary extraction process of proteins out of tissue for mass spectrometry analysis can be realized faster and more efficient than with conventional extracting methods [114]. Extracted proteins from mouse muscle and liver tissue were detected over a broad mass range from a few kDa up to several MDa in high quantities without signs of fragmentation. Most important, it was determined that the ablation process

gives a "snapshot" of the tissue's protein content – a potential complete fingerprint of the cell's phenotype. To test the intact chemical compositions, specific proteins were analyzed via MALDI-TOF after PIRL ablation and in a non-ablated control sample. The spectra obtained were almost identical confirming that proteins are not chemically altered during the DIVE ablation process. An intact enzymatic activity was evidenced by ablating trypsin and subsequent incubation with casein. In case of intact enzymatic activity of trypsin, casein is degraded and signals for intact casein is not detectable in LC-ESI-MS as in case of the PIRL ablated sample.

The successful protein extraction exploiting the DIVE process was also confirmed in human tonsil tissue [65]. DIVE tissue homogenization showed that a higher number of intact protein species in the relevant range of 30 kDa to 60 kDa can be obtained compared to conventional mechanical tissue homogenization. An explanation for this result is the ultrafast transfer of proteins from tissue to the frozen aerosol, reducing the time in which proteins are exposed to conditions in which the degradation by enzymatic reactions is possible. Moreover, the homogenate collected from the DIVE ablation contained less cell debris resulting in a higher condensate quality.

Lu *et al.* [66] demonstrated that via the DIVE process not only the laser extraction of proteins is feasible, but also the production of highly charged peptide and protein ions directly from bulk water for high sensitivity mass spectrometry. The DIVE-MS method was applied without any additional volatile solvent at a near neutral pH and no extra ionization device was needed.

In addition, the molecular dynamics during the ablation process were simulated for a model peptide in aqueous solution to characterize the DIVE process [67]. The experimental conditions within a TOF-mass spectrometer operating in vacuum with an applied electric field were investigated following ablation conditions in PIRL-DIVE. The simulations revealed that the desolvation of analytes is independent of the applied electric field within a TOF- mass spectrometer and comparable to the standard PIRL-DIVE ablation. Further, the work showed that direct desolvation and ionization were possible by DIVE and minimal fragmentation occurred. In contrast to ESI and MALDI, in DIVE-MS the optimization of the desorption and ionization process is independently possible. The desorption process can be adjusted by the PIRL pulse fluence and the subsequent ion separation process by a proper applied electric field within a mass spectrometer. Therefore the PIRL-DIVE ablation mechanism could represent a new highly sensitive source for quantitative mass spectrometry.

The combination of PIRL and mass spectrometry allowed for the differentiation between porcine brain tissues types by their lipid profile [68]. The collected condensate of the PIRL ablation plume was ionized via ESI and directly analyzed by an orbitrap

mass spectrometer. In the case of lipids, no additional sample preparation was necessary, since lipids have very intense signals and superimpose those of other molecular species such as peptides or proteins.

PIRL ablation with electrospray ionization (PIR-LAESI) was shown to be capable of tissue molecular imaging [69]. By means of PIR-LAESI the distribution of specific biological lipids and small molecules were mapped in mouse kidneys and zebra plant leaves and compared to other methods such as conventional LAESI-MS imaging. Via PIR-LAESI the limit of detection was improved by a factor of five with respect to nanosecond LAESI.

In summary, the DIVE process utilizing the PIRL is really unique as it combines the feasibility of cancer boarder recognition, tumor typing, and minimal scar tissue formation in surgical applications. Complemented with additional imaging techniques and precise robot guidance, the PIRL is a valuable tool for future medical applications.

2. Measurement of Ablation Rates in Different Tissues for a Novel Picosecond Infrared Laser (PIRL)

The following chapter will form the basis for a manuscript in preparation: S. Maier, D. Eggert, S. Kruber, N.-O. Hansen, J. Mehlan, H. Petersen, M. M. Fuh, H. Schlüter, and R. J. D. Miller, Measurement of ablation rates in different soft tissues for a novel Picosecond Infrared Laser (PIRL)

The author of this thesis independently performed the experiments, analyzed all data and drafted the manuscript. All co-authors contributed to the manuscript writing, and D. Eggert performed the Confocal Laser Scanning Microscopy measurements.

In this chapter, ablations rates and depths for the PIRL are analyzed in different soft tissues like cornea, skin and liver depending on the Gaussian beam peak fluence. The ablation rates for PIRL are compared to other surgical laser systems. Limitations for future PIRL laser designs are studied in terms of laser-induced optical breakdown in the ablated tissue.

2.1. Introduction

The ablated volume per unit time, the so-called ablation rate, is an important parameter in laser surgery for clinical applications. In numerous studies, the ablation rates were measured for ultraviolet to far-infrared wavelengths in different tissue types like skin, brain, bone or teeth [8, 71–74]. A very low ablation rate with a small ablation depth in the range of a few µm is advantageous in applications like refractive corneal surgery, where high precision is needed [5]. However, a too low ablation rate in other medical fields, e.g. dermatology or dentistry, will drastically lower the acceptance in the clinical environment due to a lack of efficient tissue removal. A precisely controllable ablation rate with high resolution is also interesting for real-time bio-diagnostics especially theragnostics [75] via mass spectrometry to characterize the ablated tissue,

i.e. during laser surgery. There are different approaches to determine the ablation rates in tissues and these can be mainly categorized in removed mass, ablation depth, and volume measurements [72]. To obtain values via the mass removal methods, digital scales are used, and for measuring the ablation depth histologic sections or scanning electron microscopes are employed [71, 76, 77]. If the ablated volume per pulse is very small, the measurement accuracy could be improved by accumulating and averaging over a series of laser pulses. Especially in this scenario, a high pulse-to-pulse stability and a well-defined transversal laser beam energy distribution, i.e. a flat top beam profile, is favorable to obtain uniform cuts or ablation surfaces for the ablation rate measurements [76]. The PIRL ablation rates are presented in this respect and the optimal performance for next generation PIRL scalpels is identified.

2.2. Materials and Methods

2.2.1. Laser System and Autofocus System

The laser system used for the experiments was a PIRL -HP3-1064 OPA -3000 (LMI Inc., Toronto, Canada) consisting of a diode pumped picosecond Nd:YAG laser used as a pump laser at a wavelength at 1064 nm, a 1650 nm seed laser and an optical parametric amplifier. Via the electrical current for the pump diodes within the Nd:YAG laser, the power output of the optical parametric amplifier was adjusted. The emitted laser pulses had a pulse duration of 400 ps, a Gaussian spatial, transversal beam shape, and a wavelength of 3000 $\pm$ 90 nm. With maximum pulse energies of around 700 µJ and a repetition rate of 1 kHz, the PIRL average output power was 0.7 W. The measured beam quality factor M^2 was around 10, and it was measured by a Silicon Microbolometer Beam Imaging Camera (WinCamD-FIR-2-16HR, DataRay Inc., Redding, USA), the associated software (DataRay v7.1H25Bk) and a translation stage (U Move M2DU, DataRay Inc., Redding, USA). Table 2.1 gives an overview of all laser settings and beam characteristics on the sample surface during the ablation experiments. The PIRL output was coupled in a home-build scanning system with an autofocus function, which kept the beam waist constantly on the tissue during the ablation of rectangular scan patterns. The beam diameter was measured at different power levels employing the beam imaging camera with a resulting accuracy around 10 µm.

In Figure 2.1, the spatial intensity profile of an emitted PIRL pulse is shown in x- and y- direction on the beam imaging camera for the beam spot at 2 J/cm^2. The blue

Parameters	**PIRL**
Wavelength	3 µm
Beam Diameter ($1/e^2$), profile	130-180 µm, higher Gaussian
Pulse width	400 ps
Repetition rate	1000 Hz
Pulse energies (E_p)	73-340 µJ
Average power	73-340 mW
Average pulse fluence (φ_a)	0.5-1.5 J/cm^2
Peak pulse fluence (φ_p)	1 -3 J/cm^2
Peak Power	0.18-0.85 MW
Peak irradiance (peak power density)	1.27-3.74 GW/cm^2

Table 2.1. – Laser settings and beam characteristics on the sample surface during ablation experiments.

data points show the measured intensities on the 17 x 17 µm pixels and the red line represents a Gaussian fit over the measured intensity data points.

For the different fluence levels, the following beam spot diameters were measured: 130 µm x 140 µm for 1 J/cm^2, 140 µm x 150 µm for 2 J/cm^2 and 160 µm x 180 µm for 3 J/cm^2. The energy measurement of the laser pulses was conducted with the precision energy meter (LabMax-Top with Energymax Sensor J-25-MB-LE, Coherent, Santa Clara, USA) and the energy was measured before each ablation of a sample. With over 60,000 measured pulses, the PIRL had a pulse-to-pulse stability around 4 % rms. For the three different fluences, the pulse energies were approximately 73 µJ, 165 µJ and 340 µJ.

2.2.2. Specimen Preparation

The porcine tissue samples were received from different local slaughter houses. The eyeball samples were ablated within 9 hours after harvesting and the liver and skin samples within 6 hours. This step was taken to keep the tissue as close to natural hydration as possible. The skin hairs had already been removed by the slaughter house via scalding. All tissue types originated from three different pigs to minimize inter-individual variability. The samples were kept at room temperature. Skin and liver samples were cut into sample sizes of 1 x 1 x 1 cm^3 and stored in DPBS (Dulbecco's Phosphate Buffered Saline 1 x, gibco^{TM} Thermo Fisher Scientific, Waltham, USA). Immediately before ablation, a film of an isotone NaCl solution (Isotone Irrigation solution 0,9 %, Braun) was put on the specimen and the skin and liver samples stayed

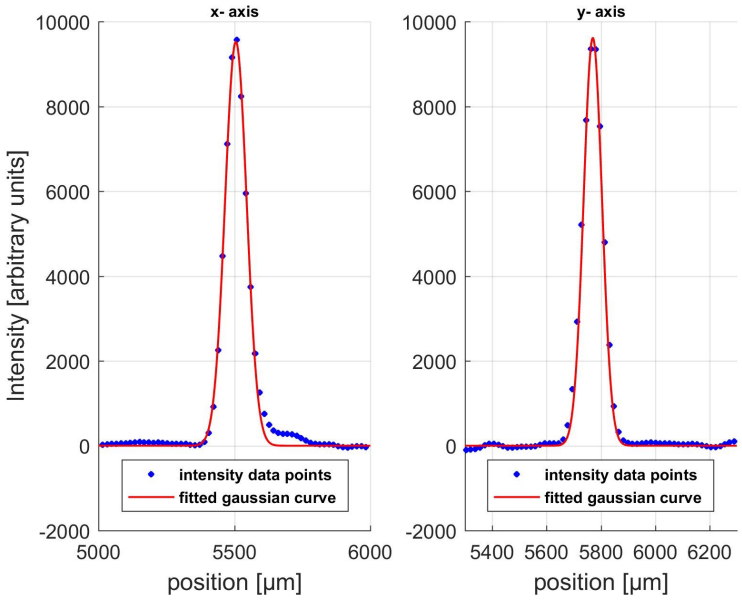

Figure 2.1. – The spatial intensity profile of an emitted PIRL pulse is shown in x- and y-direction on the beam imaging camera for the beam spot at 2 J/cm^2. The blue data points show the measured intensities on the 17 x 17 µm pixels and the red line represents the fitted Gaussian beam curves.

in DPBS during the ablation experiment with exception of the surface. After ablation, the tissue samples were immediately fixed in phosphate-buffered 3.5 % formaldehyde. Over all experimental steps the tissue samples were stored in a liquid environment to avoid a drying of the sample leading to a volume change, which would influence the calculated ablation rates.

2.2.3. Ablation Method

The ablation volume was determined for three different peak fluences of 1 J/cm^2, 2 J/cm^2 and 3 J/cm^2. The transversal intensity profile of the laser beam had an elliptical shape, as the cuts along both of the half axis differed.

The peak fluence, φ_p, on an irradiated sample area $A = \pi \cdot a \cdot b$ for an elliptical Gaussian beam profile is given by:

$$\varphi_p = \frac{2 \cdot E_p}{\pi \cdot a \cdot b}, \tag{2.1}$$

where E_p is the pulse energy and a,b are the beam waist radii in the focal plane axes of the beam focus.

The beam diameters were measured separately at different power levels relevant for the respective fluences to ensure a precise calculation of peak fluence. The laser output was attenuated by regulating the pump diode current at the Nd:YAG laser to achieve the desired fluence. To measure the depth of the ablation volume created by the laser pulses, a 2 mm x 2 mm rectangular scan was performed.

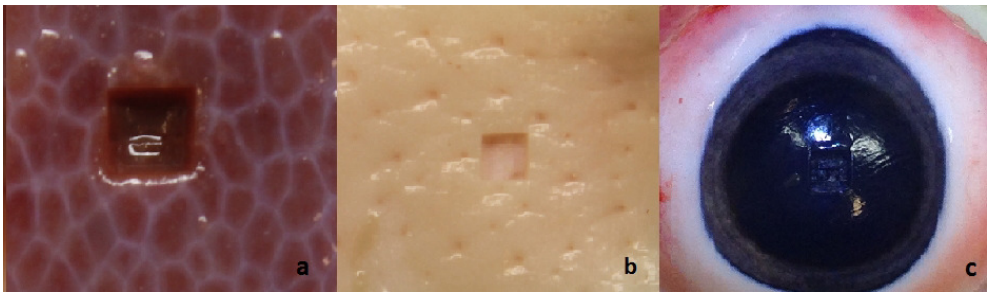

Figure 2.2. – A representative rectangular scan at the highest fluence on the different tissue samples: liver (a), skin, (b) and cornea (c).

For specifying a certain fluence range for the experiment, considerations about the limitation of the ablation process and the laser systems were made. The onset of the ablation starts at a certain threshold fluence, F_{th}, as a function of wavelength and pulse duration. For enamel in teeth, Franjic *et al.* demonstrated that the ablation threshold peak fluence for PIRL is around 0.5 J/cm^2 and about 6x smaller compared to an Er:YAG laser with a pulse duration of 250 µs [13]. According to Alster *et al.* the ablation threshold for the Er:YAG is 1.5 J/cm^2 in skin [78]. Due to the factor of 6 in the different threshold fluences as a consequence of the shorter pulse durations of PIRL, this would correspond to an average threshold fluence of 0.25 J/cm^2 and a threshold Gaussian peak fluence of 0.5 J/cm^2 in skin representing soft tissue. The lower limit of the peak fluence range was chosen to be 1 J/cm^2, to ensure being over the threshold fluence. Due to the limited beam quality and the maximum achievable output power of the laser system, the fluence range could not be expanded over 3 J/cm^2.

The ablation time was controlled with a beam shutter (SH05, Thorlabs, Newton, New Jersey, USA) and the associated shutter controller (SC10, Thorlabs, Newton, New Jersey, USA). The beam shutter itself has a temporal resolution of about 1 ms and a closing time of about 4 ms. This results in a minimal error of 5 ms and hence in the parts-per-thousand range for the ablation rate measurements. The shutter time was set to 160 s for 1 J/cm^2, 80 s for 2 J/cm^2 and 40 s for 3 J/cm^2, which corresponds to 160.000, 80.000 and 40.000 pulses, respectively, at a repetition rate of 1 kHz. For cornea samples the shutter time was reduced to 80 s for 1 J/cm^2, 40 s for 2 J/cm^2 and 24 s for 3 J/cm^2 due to the limited layer thickness of the tissue.

In initial experiments, an interlacing of the beam position with a displacement distance of 50 µm between the pulses, realized through scanning the beam at 50 mm/s on the sample stage, showed very smooth tissue removal and was chosen for the experiments. Figure 2.3 shows the overlapped fitted Gaussian beam curves at 2 J/cm^2 with a peak-to-peak-distance of 50 µm in x- scanning line direction and a black curve with the summation of the overlapped intensity beam profiles.

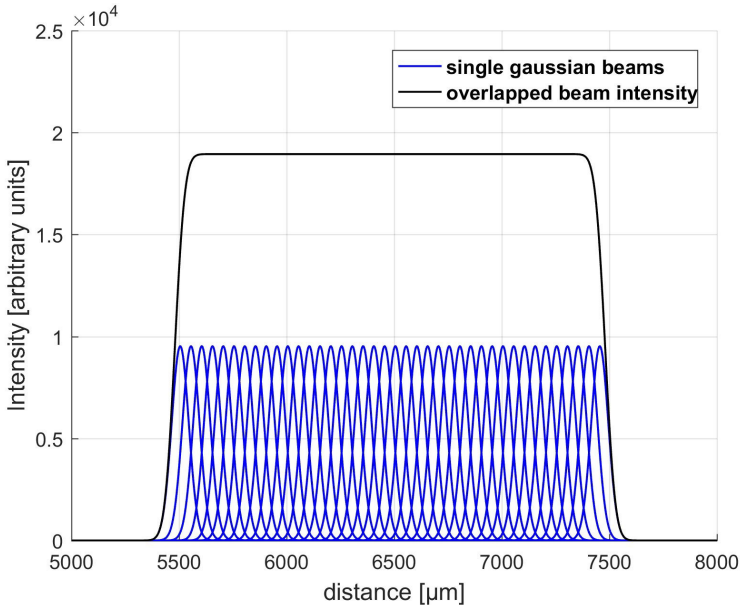

Figure 2.3. – The fitted Gaussian beam curves (blue) of 40 overlapped PIRL pulses for 2 J/cm^2 in x-direction with a peak-to-peak distance of 50 µm in one scanning line. The black line shows the summation of all overlapped intensity beam profiles.

In y- scanning direction, the laser pulses were also overlapped with a peak-to-peak-distance of 50 µm, but in addition also slightly offset relative to the previous scan line to obtain a smoother ablation of tissue. Several surface scans were conducted to ablate the tissue layer per layer. Three tissue samples of each tissue type, liver, skin, and cornea, were ablated for each fluence setting of 1 J/cm^2, 2 J/cm^2 and 3 J/cm^2, respectively. To measure the total ablated volume for each sample, Confocal Laser Scanning Microscopy (CLSM) was used. The measured total ablated tissue volume was divided through the number of laser pulses to calculate the average ablated volume for a single laser pulse.

2.2.4. Confocal Laser Scanning Microscopy (CLSM)

To image both the cell membranes representing the outer border of the cells and the nuclei of the cells, two different fluorescent markers were used. The plasma membranes of the cells were stained with CellMask Orange Plasma Membrane Stain (Thermo Fisher Scientific Inc., Waltham, MA, USA) at a concentration of 5 mg/ml in phosphate buffered saline (PBS, Sigma-Aldrich Chemie GmbH, Hamburg, Germany) for 15 min. The nuclei of the cells were stained with Hoechst 33342 (Thermo Fisher Scientific Inc., Waltham, Massachusetts, USA) at a concentration of 10 mg/ml in PBS. The tissues were imaged in glass bottom culture dishes (P35G-1.5-10-C, MatTek Corporation, Ashland, MA, USA) in wet state hydrated with PBS.

Three-dimensional images of stained tissues were acquired with a Confocal Laser Scanning Microscope (C2+, Nikon GmbH, Düsseldorf, Germany) equipped with a 4x objective (Plan Apo Lambda 4X/0.20, Nikon GmbH) and a 10x objective (Plan Apo Lambda 10X/0.45, Nikon GmbH). A 543 nm HeNe laser (Melles Griot GmbH, Bensheim, Germany) was used for excitation of the CellMask Orange Plasma Membrane Stain fluorescence and a 405 nm diode laser (Coherent Inc., Santa Clara, CA, USA) for Hoechst 33342. The 3-dimensional datasets were analyzed in Bitplane Imaris (v. 8.2.1., Bitplane AG, Zurich, Switzerland). The ablated volumes were reconstructed and measured using the "surface"-function of the software.

The accuracy of the method is limited by the irregularities in the tissue surface and the accuracy of the Confocal Laser Scanning Microscopy. In the experimental series the maximum measurement error for the volume measurement caused by the resolution limit of the Confocal Laser Scanning Microscope was ±1.32 %.

2.3. Results

2.3.1. Ablation Rate vs. Peak Fluence

Via Confocal Laser Scanning Microscopy the ablated volumes were imaged and showed a rather rough ablated structure in cornea and skin compared to a much smother structure in liver (Figure 2.4). The different ablation structures can be ascribed to varying water content in the ablated tissue types, as well as varying tissue structural composition. In soft biological tissues, cells are surrounded by an extracellular matrix (ECM) serving as structural and biochemical support. The ECM is a non-cellular complex network in tissue, consisting of fiber proteins like collagen and elastin, glycoproteins, proteoglycans and cell adhesion proteins [37, 79].

Both the ratio of ECM to cell and water content as well as the composition of the ECM itself vary between different tissue types [79]. In liver, the ECM ratio is considerably lower than in dermis, and corneal stroma. Scanning Electron Microscopy pictures of PIRL laser incisions in mice within first wound healing studies revealed intact collagen layers after ablation and give a hint for the reduced ablation of ECM components [39].

To determine the ablation rate depending on the laser peak fluence, a 3D-domain representing the ablated volume was modeled *in silico* into the ablated area and the volume in μm^3 was calculated using suited computer software (Bitplane Imaris). The total ablated volume was divided by the respective number of laser pulses for each fluence to obtain the average ablated volume per pulse. In the next step, the ablated volume per pulse was multiplied by the repetition rate to obtain the ablation rate in mm^3/s.

Figure 2.5 shows the ablation rates in cornea (a), liver (b) and skin (c) at different peak fluences 1 J/cm^2, 2 J/cm^2 and 3 J/cm^2, with mean values calculated from the three data points for each fluence. The error bars in x-direction originate from the accuracy of the beam diameter measurements and subsequent peak fluence calculations. In cornea, the mean values for the ablation rates range between 0.007 mm^3/s for 1 J/cm^2 and 0.057 mm^3/s for 3 J/cm^2, in skin between 0.006 mm^3/s for 1 J/cm^2 and 0.055 mm^3/s for 3 J/cm^2, and in liver 0.018 mm^3/s for 1 J/cm^2 and 0.105 mm^3/s for 3 J/cm^2, respectively. In cornea and skin the mean ablation rates are almost comparable, while in liver the mean value ablation rate is roughly doubled compared to skin.

In addition, the maximal deviation to the mean value was calculated for every fluence in the different tissue types. In cornea the percentile deviation of the mean value is

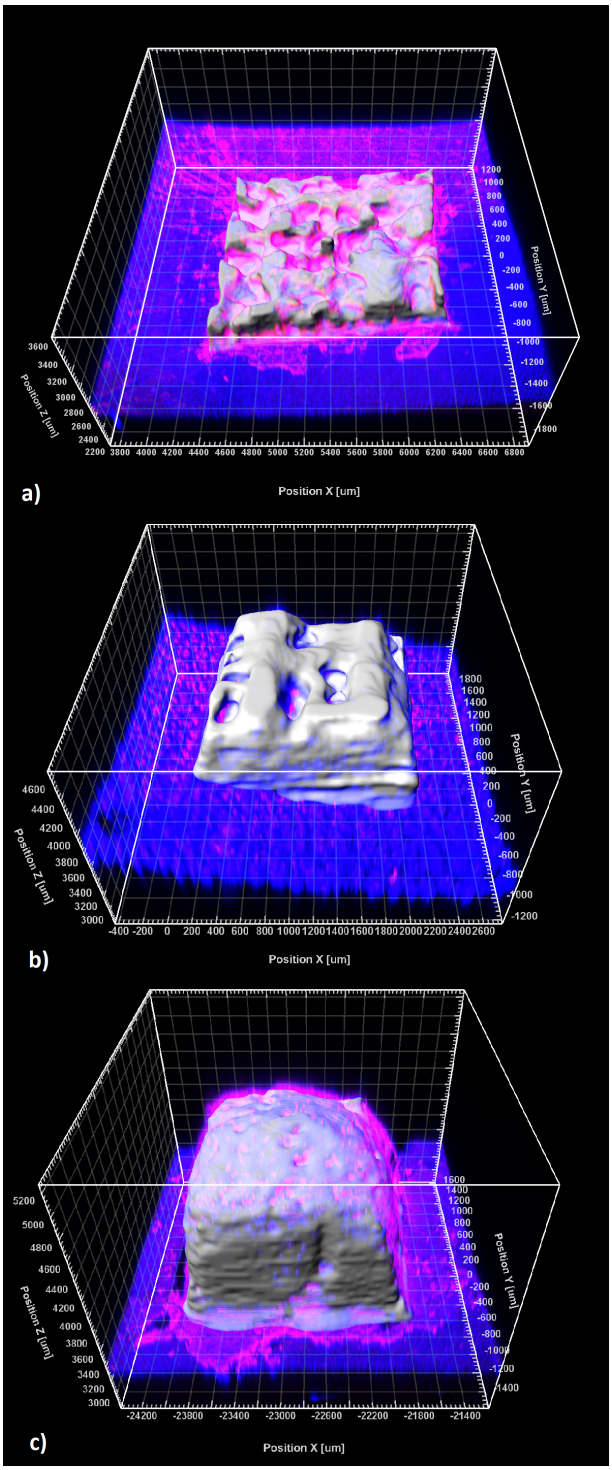

Figure 2.4 – 3D views of ablated cornea, skin and liver samples imaged by Confocal Laser Scanning Microscopy picture. Cornea, skin and liver samples were ablated with 2 x 2 mm scan and a peak fluence of 3 J/cm^2. Bottom-up views of 3D datasets of a representative cornea (a), skin (b) and liver (c) sample stained with CellMask Orange Plasma Membrane Stain (red) and Hoechst 33342 (blue). The stains were used to create the reference positions and modeling the respective surfaces and resulting volumes (grey) in the tissue samples. The surface after ablation in liver (c) is considerable smoother compared to cornea (a) and skin (b) with a higher collagen content.

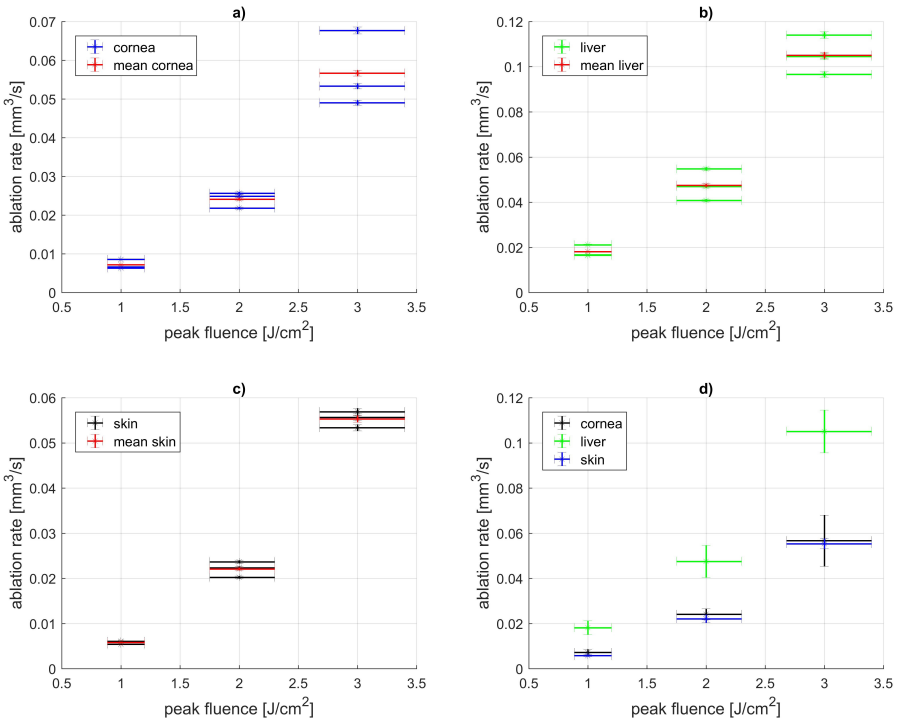

Figure 2.5. – Overview of ablation rates in different tissue types. Ablation rate in cornea (a), liver (b), and skin (c) at different fluences 1 J/cm^2, 2 J/cm^2 and 3 J/cm^2, with average values calculated from the three data points for each fluence. The average values from the different tissues are plotted on a graph (d). The error bars in x-direction indicate the measuring inaccuracy of the beam diameter measurements, in y-direction the measuring inaccuracy of the Confocal Scanning Microscope (a-c) and maximal deviation of the average value (d).

19 % for 1 J/cm^2, 10 % for 2 J/cm^2, and 20 % for 3 J/cm^2, in liver 17 % for 1 J/cm^2, 15 % for 2 J/cm^2 and 9 % for 3 J/cm^2, and in skin 7 % for 1 J/cm^2, 8 % for 2 J/cm^2 and 4 % for 3 J/cm^2. The percentile deviations of the average value over the whole fluence range differ strongly within one tissue type, however in cornea the highest deviations could be found in contrast to skin, where all deviations reside within the single-digit range. These deviations were attributed to inhomogeneous distribution of water in the tissue and degree above the threshold fluence.

2.3.2. Ablation Depth vs. Peak Fluence

For ablation processes, different theoretical models exist to obtain predictions for the removed material amount, depending on laser and tissue parameters. For pulse durations shorter than 100 ns and a wavelength with a very high absorption coefficient compared to the scattering coefficient in the tissue, typically all conditions for applying the so called Blow-off Model are fulfilled [37]. The reason for the pulse duration limitation to shorter than 100 ns for applying the Blow-off Model is that the tissue removal with forming an ablation plume starts only after the laser pulse is completely absorbed within the tissue. Thus, for the Blow-off Modell the Beer's Law is applicable to calculate optical penetration or ablation depth of the laser beam in the tissue [37]. The Blow-off Model states a semi logarithmic correlation between the ablation depth in medical applications, and the incident radiant exposure in J/cm^2. Alternatively, it could be presented as a linear relationship between the ablation depth and the logarithm of the fluence [76].

Due to Beer's law, the fluence inside the tissue *F(x)* can be calculated in dependency of the fluence at the surface, F_0, and the distance to the surface x [13, 76] by:

$$F(x) = F_0 \cdot e^{-\alpha x}, \tag{2.2}$$

where α expresses the absorption coefficient of the medium. In water the absorption coefficient for a wavelength of 2.94 µm is subject to dynamic changes depending on the incident fluence and the temperature [80, 81]. In Cummings and Walsh, the low-intensity absorption coefficient at λ= 2.94 µm of around 13,000 cm^{-1} for liquid water decreases to values lower than under 1000 cm^{-1} for high fluences, resulting in an absorption length L of 0.77 µm and 10 µm, respectively [81]. The absorption coefficient measured in water can only translate to an approximate absorption coefficient in soft tissue, as the water amount ranges between 70 % and 80 %. Therefore, the absorption coefficient for λ = 2.94 µm in tissue will be smaller and a higher absorption length is expected [80].

Based on the Beer's law the ablation depth d could be estimated by [76]:

$$d = \frac{1}{\alpha} ln \frac{F_0}{F_{th}}, \tag{2.3}$$

The applied energy density on the tissue surface, F_0, for a single pulse varies accordingly to the Gaussian intensity profile of the PIRL beam. To get a homogenous surface

abrasion the Gaussian beam pulses must be sufficiently overlapped, that the overlapping pattern of all laser pulses per layer form in summation a rectangle uniform energy density in both directions as shown in figure 2.3. If the overlapping distance is optimized, for every beam spot size an even distribution of energy density can be created at a minimum intensity level. At this minimum level, the arising energy distribution corresponds to the previously mentioned peak fluence, φ_0. Therefore, in Equation 2.3 the Gaussian peak fluence equals the applied energy density on the tissue surface, F_0, and the theoretical minimal ablation depth for a one layer abrasion can be calculated. For the threshold Gaussian peak fluence, F_{th}, 0.5 J/cm^2 was used. Since the applied peak fluences for the PIRL were very low compared to average fluences in the range of 10 J/cm^2 to 80 J/cm^2 in the work of Cummings and Walsh, an absorption length of 13,000 cm^{-1} was used for an estimation [81]. For these parameters the theoretical calculated minimal ablation depth for the peak fluences from 1 J/cm^2 to 3 J/cm^2 ranged from 0.5 µm to 1.4 µm.

The ablation depth for one layer with a peak-to-peak distance of 50 µm was estimated from the measured ablation volume. Therefore, the mean value of total ablated volume for each fluence was divided by the scan area and the number of ablated layers. Figure 2.6 shows the ablation depth for one layer in cornea, liver and skin. In cornea, the ablation depth ranges from around 3 µm to 19 µm, in skin from 2 µm to 19 µm and in liver from 6 µm to 36 µm.

To estimate the ablation depth at the peak of the Gaussian beam for a single laser pulse independently of the scanning pattern, it is assumed that the shape of the ablated volume is equivalent to a two-dimensional Gaussian function. The volume, V, under a two-dimensional Gaussian is defined as:

$$V = 2 \cdot \pi \cdot A \cdot \sigma_x \cdot \sigma_y, \tag{2.4}$$

where A is the height of the peak, and $\sigma_{x,y}$ the standard deviation in x- and y-direction. The standard deviation in x- and y-direction was calculated from the fitted Gaussian beam curve shown in Fig. 2.1 for the three beam sizes. Taking V for the measured ablated volume per pulse, the ablation depth, d, can be calculated resolving the formula above for the peak height, A, and setting A=d. In cornea, the ablation depth per pulse varied from 0.9 µm to 4.5 µm, in skin from 0.7 µm to 4.4 µm, and in liver from 2.2 µm to 8.3 µm as shown in Fig. 2.6.

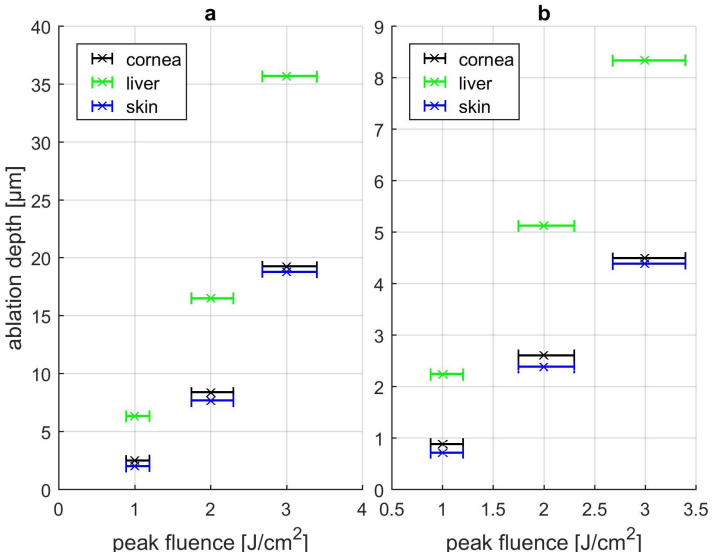

Figure 2.6. – Overview of ablation depth in µm for one layer in cornea, liver and skin for a scan pattern with a peak-to-peak distance of 50 µm (a). Ablation depth at the peak of the Gaussian beam for one laser pulse in µm in cornea, liver and skin (b). The error bars in x-direction result from the measuring inaccuracy of the beam imaging camera and in y-direction from the measuring inaccuracy of the Confocal Scanning Microscope.

2.4. Discussion

2.4.1. Choice of Method to Determine the Ablation Rate

The ablation rate of different tissue types (liver, skin, and cornea) was quantified in this study and the obtained data was compared to each other. Using Confocal Laser Scanning Microscopy for the determination of the ablated volume has some great advantages compared to other techniques in determining the ablation rate. Histologic sections are disadvantageous, because the samples are modified in size as well as shape during the histological processing [76]. The mass loss technique via digital balances has limitations particularly with soft tissues, since dehydration by evaporation of wet tissue occurs as soon as the surface of the wet tissue is exposed to air. Therefore, one of the big advantages of the ablation volume measurements via Confocal Laser Scanning Microscopy is the fact that the tissues are not altered in shape and size

after the irradiation and all following processing steps are conducted within a liquid environment.

2.4.2. Challenges of Gaussian Laser Beam Profile and Ablation Depth Determination

Due to the Gaussian fluence distribution, not the whole irradiated beam spot area was above the estimated ablation threshold of 0.5 J/cm^2 in soft tissue. For this reason, it should be distinguished between the measured 1/e^2 diameter of the laser beam and the effective ablative beam diameter on the tissue. The effective ablative diameter was calculated to be around 76 µm x 83 µm for 1 J/cm^2, 115 µm x 125 µm for 2 J/cm^2 and 152 µm x 170 µm for 3 J/cm^2. When the beam spot area for the effective ablative beam diameter was calculated and compared to the original measured beam area, the ratio ranged from 35 % for 1 J/cm^2 to 90 % for 3 J/cm^2. Therefore, at the lowest peak fluence, the greatest part of the applied energy is lost as absorbed heat in the non-ablative wings of the Gaussian beam profile. In principle, a flattop beam profile is clearly preferable to avoid the energy loss in the non-ablative wings and the resulting thermal collateral damage in the adjacent tissue [13].

If for technical reasons, a Gaussian beam profile has to be applied to the ablation process, a higher peak fluence improves the efficiency of the ablation with respect to the applied laser energy. The ablation rate in mm^3/s depends on the laser and effective ablative spot size. This dependence can be avoided by calculating the peak ablation depth per pulse, as this parameter is independent of the beam spot size. A semi logarithmic increase of the peak ablation depth with respect to an increased peak fluence can be expected.

The comparison of the ablation depth per pulse derived from the experimental data with the theoretical estimation shows a difference. The calculated ablation depth for a single pulse reaches up to 8.3 µm at the highest peak fluence in liver compared to the theoretical estimated ablation depth of 1.4 µm for relatively low fluences like 3 J/cm^2. This difference is a factor of around 6. An explanation for the deviation between the theoretical and calculated value can be a changed absorption length due the ultrafast liquid-gaseous phase transition of liquid water in tissue on the timescale of picoseconds. There is also dynamic blue shift in the water absorption spectrum as the water is heated and hydrogen bond breaking occurs [33]. The absorption coefficient of vaporized water at the used laser wavelength is considerable smaller and the water vapor becomes almost transparent compared to liquid water [76]. This dynamic effect in the water absorption spectrum as the ablation process evolves from superheating

the water to the phase explosion explains why a 400 ps laser pulse can penetrate deeper into the tissue than the expected theoretical value where these effects are neglected.

2.4.3. Influence of Tissue Constitution

To understand the different ablation rates at the same fluence, the structure of the different tissues, especially in terms of water and collagen content, is important. Porcine skin is an established animal model for human skin because it shows similar thickness, collagen content, and characteristics regarding water permeability [82–84]. Skin can be described as consisting of three layers: the epidermis, the dermis, and the subcutis. The water content in percent of wet mass in human skin ranges from 54 % in the stratum corneum up to 78 % in the stratum basale within the epidermis and is around 75 % in the dermis [85]. Since the stratum corneum is a very thin layer compared to the other layers, an average water content of around 75 % could be assumed for the ablated skin tissue. The collagen content in human skin can be specified in percentage of the dry fat-free weight and varies around 72 % at this condition [86]. In addition, the collagen content can be indicated as total percentage of the wet weight. In mature animals, up to 30 % collagen content of the wet weight was measured in skin [87]. The porcine liver has a water content of around 70 % to 80 % and the collagen content is 2.5 % of the dry fat-free weight [86]. Porcine eyes also show similarities with human eyes [88]. The water content in human cornea is around 86 % [89]. An exact percentage of collagen in human cornea wasn't found in literature; however in mature animals the collagen content of the wet weight is between 12 % and 15 % in cornea [87].

The water content in the ablated tissues ranges from 75 % to 86 % and cannot explain the almost doubling of the ablation rate between liver and skin tissue. It seems more likely that the collagen content plays a crucial role, because the collagen content of the dry fat-free weight differs considerable from 2.5 % in liver to 72 % in skin. Moreover, the surface structure of the ablated rectangle in the CLSM pictures is obviously smoother in liver with a low collagen content compared to skin and cornea, where remaining structures could be identified. This hypothesis is also supported by a study in which corneal stroma was ablated with an argon fluoride excimer laser with a wavelength of 193 nm. The ablated area was not smooth at lower fluences and as one possible explanation, a non-uniform macromolecular structure of collagen is mentioned [90].

2.4.4. Comparison of Experimental Ablation Rates Achieved with PIRL and Other Laser Systems

The ablation depth differs strongly in soft tissues depending on wavelength, pulse duration, applied fluence and repetition rate (Tab. 2.2). For a wavelength between 2920 nm and 2940 nm the ablation depths reported in literature already differ between 10 µm and 50 µm. In Kaufmann and Hibst, the ablation rate at the same fluence is being reduced with an increasing repetition rate, due to the absorption and scattering of light caused by the accumulated debris within the ablation plume in the beam path [91]. The expansion of a water plume in the DIVE regime was investigated by dark-field imaging and showed that the ablation plume mainly collapses within 20 µs [36]. Due to fast ablation process of PIRL, it can be expected that the repetition rate of 1 kHz did not influence the ablation rate measurements.

By means of the data in Tab. 2.2 the ablation rates in mm^3/s could be roughly estimated for the different laser parameters and tissues. In Kaufmann und Hibst, porcine skin samples were ablated and an estimated ablation rate is probably comparable to the present work [91]. Since the laser had a flat top beam, a cylinder-shaped volume was used to calculate the ablated volume per pulse. Under this assumption the ablation rate of the Er:YAG laser with a wavelength of 2940 nm ranged within 0.03 mm^3/s and 1.45 mm^3/s in porcine skin. In Walsh and Deutsch, the ablation rate in Guinea pig skin was compared between an Er:YAG and a TEA CO_2 laser and showed similar values [72]. Therefore, if the PIRL is compared to the Er:YAG and CO_2 laser, it shows a relatively low ablation rate in the range of 0.006 mm^3/s to 0.055 mm^3/s. It is noted that the degree above threshold is much higher, by nearly an order of magnitude over the used one for PIRL for this comparison. However, the Er:YAG and CO_2 laser systems are the benchmarks for an acceptable cutting speed. On this basis, an improvement of the ablation rate for PIRL is probably necessary for a successful clinical use in dermatology. The other attributes such as scar free and high precision however will lead to a number of important applications, from surgery near critical regions, for cosmetic reasons, and for micro-biopsies, even at the present ablation rates.

To estimate the ablation rate in soft tissue like calf brain for the wavelength of 2920 nm and picosecond pulses in Götz *et al.*, the ablation depth was multiplied with the spot size area calculated with a spot size of 25 µm. The obtained ablation rate was around 0.02 mm^3/s and was in a similar range as the PIRL. Also for the wavelength of 263 nm and 526 nm in calf brain with picosecond pulses a cylinder-shaped tissue removal was presumed and ablation rates between 0.016 mm^3/s for 526 nm up to 0.03 mm^3/s for 263 nm were calculated. For all three wavelengths in the picosecond regime the ablation rate is in a similar range as the PIRL. For refractive surgery in corneal stroma often

Reference	λ [nm]	Tissue	Pulse width	Rep rate [Hz]	Beam profile	Pulse energy	Spot size [µm]	Fluence [J/cm^2]	Ablation depth [µm]
Kaufmann and Hibst, 1996 [91]	2940	Porcine skin	150-450 µs	1-10	Flat top	300-600 mJ	2000	10-20	∼10-45
Walsh and Deutsch, 1989 [72]	2940	Guinea Pig Skin	1 µs	2	Flat top	Up to 1 J	1100	∼1-20	∼10-60
Götz *et al.*, 1995 [71]	2920	Calf brain	19 ps	1000	Gaussian	200 µJ	25-30	32 ±8	50
	263	Calf brain	19 ps	1000	-	12 µJ	20	4	100
	526	Calf brain	19 ps	1000	-	65 µJ	10	-	100-200
Loesel et , al. 1994 [92]	800	Calf brain	180 fs	100	Gaussian	165 µJ	20		200
	1053	Calf brain	30 ps	100	Gaussian	165 µJ	20	-	100
Fantes and Waring, 1989 [90]	193	Corneal stroma	14 ns	1	Flat top	-	3000	0.05-0.85	0.15-1
PIRL	3000	Porcine skin	400 ps	1000	Gaussian	73-340 µJ	130-180	1-3	0.7-44
		Porcine cornea							0.9-4.5
		Porcine liver							2.2-8.3

Table 2.2. – Overview of ablation depth found in literature data in different tissue types depending on different laser parameters. Empty fields indicate that no information for the respective parameter in the papers could be found. In the last row, the values are listed for PIRL. In case of the ablation depth for PIRL, the values represent the depth at the peak of the Gaussian beam for one laser pulse.

excimer lasers are used and in case of an argon fluoride excimer laser the ablation rate in Fantes and Waring was estimated to range from 0.001 mm^3/s to 0.007 mm^3/s [90]. For laser applications in cornea transplantation no ablation rate measurements with other laser systems are known to the authors' best knowledge. Thus, the ablation rate of PIRL is compared to an argon fluoride excimer laser for refractive surgery in corneal stroma. According to the low ablation rates in cornea for the mentioned excimer laser, the PIRL possess already a sufficient fast ablation rate for corneal surgery like cornea transplantation.

2.4.5. Limitations for Future Laser Designs

In Franjic *et al.* [13], it was already mentioned that lower energy densities during ablation reduce the residual damage to the surrounding tissue and for this reason PIRL may be preferable in some applications. An upper limit for the increase of the peak fluence is the laser-induced optical breakdown (LIOB), because it not only decreases greatly the ablation rate [76], but more important the reactive ions in the generated plasma cause biochemical damage to the structurally intact cells in the adjacent tissue leading to a slower wound healing process compared to mechanical tools [13, 93]. There are obvious inherent long term health risks with ionizing radiation effects that should be avoided. The LIOB is an irradiance-dependent nonlinear process, which depends not only on the pulse duration and laser fluence, but also on the wavelength. In the picosecond range the square-root law is applicable for the LIOB threshold in tissues like human enamel, human cornea and bovine brain [27]. As rule of thumb, power densities over 10^{11} W/cm^2 in solids and fluids exceed the LIOB threshold, but in case of 3 µm laser pulses the threshold for plasma generation should be considerable higher [5]. In human cornea, a LIOB threshold of 40 J/cm^2 at a pulse width of 200 ps for 1053 nm was measured by Loesel *et al.* [27]. In Götz *et al.* a power density of around $2x10^{12}$ W/cm^2 for a 3 µm laser wavelength with a pulse duration of 19 ps corresponding to a fluence of 32 ± 8 J/cm^2 was reported without observing a plasma spark [71]. Applying the square-root law on typical pulse durations for operating in the DIVE regime of about 10 ps to 400 ps, the maximum acceptable fluences are between 23 ± 6 J/cm^2 and 147 ± 37 J/cm^2. In figure 2.7, the maximum acceptable pulse energies in mJ to operate under the LIOB threshold for pulse durations between 10 ps and 400 ps are shown in dependency of the spot size diameter.

Pulse energies in the range of 1 to 2 mJ and a significantly improved beam quality are within reach by a new envisioned laser design using a straight forward approach to directly amplify 3 µm laser radiation from a seed laser. As visualized in figure 2.7, improvements in the laser beam quality even with the present laser platform creates

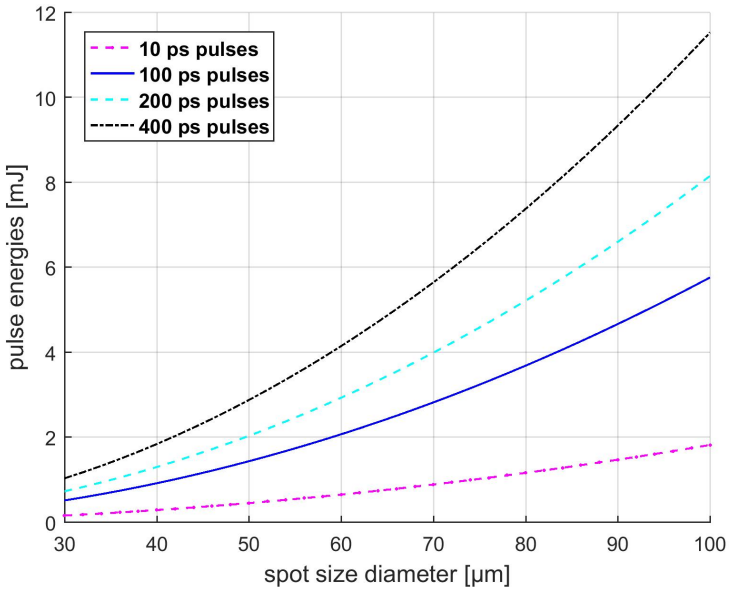

Figure 2.7. – Maximum acceptable pulse energies in mJ to operate under the LIOB threshold for four different pulse durations in dependency of the spot size diameter.

the possibility to reach LIOB threshold fluences for small spot size diameters under 40 µm so that some care is needed in choosing beam parameters.

2.5. Conclusion

This study evaluated the ablation rate of PIRL at a Gaussian peak fluence range of 1 to 3 J/cm^2 in different soft tissues by ablating small rectangular patterns with multiple scan area passes. Confocal laser scanning microscopy was used to measure the ablation volume for each sample and subsequently determine the ablation rate and ablation depth in the different tissue types like liver, skin and cornea. Compared to an Er:YAG laser, the ablation rate of the PIRL in porcine skin is at the low end of the ablation rate range and in porcine cornea it is comparable to an excimer laser. The ablation depth for one ablated layer with a close spatial horizontal overlap of laser pulses ranges from a few micrometers up to tens of micrometers depending on the applied Gaussian peak fluence. The ablation depth for one laser pulse is estimated

to reach from sub- micrometer scales up to several micrometers in different tissues and shows the possibility of high precision ablation for laser surgery with very high resolution. This study suggests that the ablation rate in skin is probably too low for clinical use and has to be increased by raising the repetition rate and pulse energy close to the laser-induced optical breakdown for cutting speeds are par to other surgical devices. However, the PIRL laser has already a sufficiently fast ablation rate for corneal surgery like cornea transplantation. In all surgical applications, the trade off in cutting speed and reduction in collateral damage may lead to wider applications of the PIRL scalpel. This work quantifies the cutting speed and allows straight forward extrapolations as to what is possible with increased beam quality and power of next generation PIRL systems.

3. Surgical Laser Scalpel with a Tapered Fiber Tip

The following chapter is based in part on the European patent: R. J. D. Miller, S. Uschold, S. Kruber, N.-O. Hansen, Laser Surgery Apparatus for Contact Laser Surgery, EP 306 7005 B1.

The author of this thesis performed all experiments, analyzed the data and drafted the invention disclosure for the patent application together with R. J. D. Miller. Confocal Laser Scanning Microscopy was performed by D. Eggert, and support by F. Tellkamp with Zemax simulations is acknowledged.

In this chapter, a new hybrid concept for a laser scalpel is presented in which an optical fibre with a custom designed blade-like tip is used to guide laser light to the tissue, while simultaneously, this tip is used to mechanically cut the tissue. Simulations with a raytracing software were used to calculate the light intensity distribution directly at the fibre endface and in the far-field. First cuts with the new tip design were performed in a proof-of-concept experiment in soft tissue and compared to cuts created by a conventional scalpel.

3.1. Introduction

A mechanical scalpel cuts skin by inducing high shear stress on a very small area to exceed the rupture limit of the tissue until it tears. The damage through a scalpel incision extends up to 400 microns into the adjacent tissue [39]. The extent of the damage influences the subsequent formation of scar tissue. New cutting tools can improve the outcomes of current mechanical tools and are subject of a number of studies.

First ideas of new fibre tip designs for medical applications date back to the year 1986, when Hussein *et al.* developed a so called hot tip consisting of an optical fibre with a simple metal end cap to treat plaque deposits in angioplasty. With this new fibre

tip design, the main existing limitations in laser angioplasty, namely vessel perforation and insufficient sizes of the created canals could be solved. In this approach, the laser energy of an Argon laser is absorbed in the metal cap at the end of the fibre, which creates a homogenous distribution of heat at the tip. The heat is subsequently conducted from the metal fibre tip to the occlusive tissue [94].

In other designs, focusing fibre tips were realized for flexible fibre systems used in laser induced shock wave lithotripsy. In this procedure, kidney stones and biliary calculi are fragmented by shockwaves. The fibre tip itself was polished to obtain a spherical surface creating a beam focus in a distance of several millimeters. A steady visual control was crucial, since a constant distance between fibre tip and stone has to be ensured [95]. In addition, first attempts exist to use a modified optical fibre tip to optimize the radiation delivery and to apply it as an in-contact scalpel for laser resections. In this indirect laser surgery, the fibre core was coated with an absorbing material and the subsequently heated tip was used for cutting the tissue [96]. As coating material, graphite microparticles with silicon organic varnish were applied [96–98], but also an absorptive carbon layer on the fibre end tip was investigated in an additional study [99]. The carbon layer was formed due to carbonization of the tissue during the laser resection. Moreover, reflective metal elements at the distal end of the fibres were used to guide the reflected laser light to the tissue. In Costello *et al.* [100], a prototype of a fibre tip with a reflecting gold alloy was used to effectively treat benign prostatic hypertrophy in 1992.

In addition, first efforts were made to develop exchangeable fibre tips with optimized geometries for distinct applications. In Stock *et al.* [101], conically shaped fibre tips revealed improved cutting qualities particularly with regard to improved regular and deeper cuts compared to a conventional cleaved bare fibre in soft tissue. An improvement in cutting with this tip design was achieved by increasing the laser fluence at the fibre end. The diameter of a cylindrical sapphire fibre was tapered from a 800 µm to 200 µm at the endface with a cone angle of 5°.

These studies showed that fibre tip shaping and coating can lead to significant improvements in performance. Coatings are typically easier and less expensive to apply than creating a fibre tip of specific shape. However, for in-contact procedures, the fabrication of friction resistant coatings can be challenging.

The principal idea of the fibre tip development presented in this chapter is to locally reduce the shear stress needed for cutting by heating the water in the tissue with an ultrafast laser. Due to material science experiments in solid states, it is known that the modulus of rupture decreases very rapidly at temperatures over 1000°C [102]. Since the main constituent in tissue is water, the point of rupture can be expected to be far below such a high temperature value. The temperature rise in tissue when

operating close to an average ablation fluence of 1 J/cm^2 was estimated for PIRL to be over 1000 K. In this consideration, an absorption depth of 1 µm was assumed and adiabatic expansion was neglected. For that reason, it is expected that the shear forces required to cut the tissue collapse to almost zero or at least dramatically decrease by applying the ultrafast laser heating of water in tissue. The simultaneous mechanical forces should cut the tissue.

3.2. Materials and Methods

3.2.1. Laser System

As in chapter 2, a PIRL -HP3-1064 OPA -3000 (Attodyne Inc., Toronto, Canada) was used for the experiments. Via the electrical current for the pump diodes within the Nd:YAG laser, the output power of the optical parametric amplifier was adjusted.

3.2.2. Fibre Tip Designs

The PIRL output was coupled into a sapphire multimode fibre (Photran LLC Inc., Poway, California, USA) with a 250 µm fibre core diameter and a length of approximately 1 m. Sapphire fibres were chosen for the experiment, because they are not only biologically inert, but also possess a very high damage threshold in the infrared region [103]. Moreover, the sapphire fibre is characterized by a low numerical aperture, and a very high heat resistance with a melting point of 2053°C. The refractive index is 1.71 for a wavelength of 3 µm [104]. The tapered fibre tips were produced by polishing the tip of the sapphire fibres via a fibre polishing machine with a polishing angle setting option (Trig^{TM} Bare Fibre Polisher, KrellTech, Neptune, New Jersey, USA). In a first step, diamond polishing films with a grid size of 30 µm were used to obtain the desired tip shape, and in the following step the tip surfaces were polished with a finer grid size of 1 µm. Two different fibre tips were produced to elaborate the best fibre tip design for the cutting process. In both fibre tip designs, two opposite sides were polished under an angle to obtain in one case a rectangular endface of the tip as cutting surface, and in the second case a tapered fibre tip without endface. The fibre tip with a rectangular endface is referred to blunt fibre hereinafter and the second tip design without endface is called sharp fibre tip. The endface size of the first fibre tip was measured via a calibrated light microscope (AZ100 Multizoom, Nikon GmbH, Düsseldorf, Germany) equipped with a 5x objective lens. Figure 3.1 shows a top view on the fibre tips as well as a side view turned by 90°.

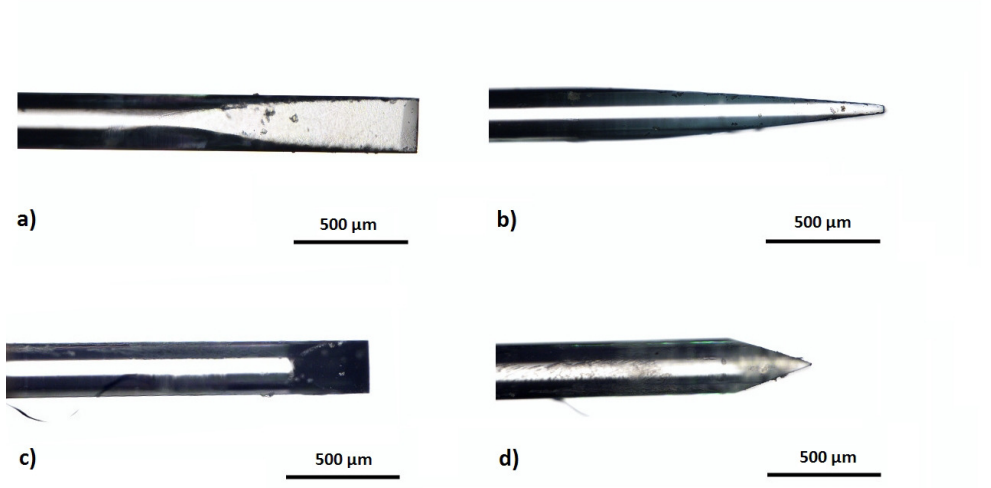

Figure 3.1. – Different views of the two fibre tip designs. Top view (a) and side view (b) on the blunt fibre tip. Top view (c) and side view (d) on the sharp fibre tip.

To obtain a good estimation of the small width of the fibre endface, the size was measured from opposite sides and an average value was formed. The blunt fibre tip had an endface of 25 µm in width and 250 µm in length. The angle of the blunt fibre tip was 5°. The angle was chosen to obtain total reflection within the shaped fibre tip, thus the reflected light exits at the plane endface. For that reason, a reflective coating can be avoided. The second fibre tip design without a rectangular front closely resembles the shape of a conventional scalpel like shown in microscopic investigations by McCarthy *et al.* [105]. For this fibre shape, only a bigger angle of at least 18° could be realized, without breaking the tip end during the polishing procedure.

The beam output of the fibre tips was visualized via a Silicon Microbolometer Beam Imaging Camera (WinCamD-FIR-2-16HR, DataRay Inc., Redding, USA). The average fibre output was measured by an energy meter (LabMax-Top with Energymax Sensor J-25-MB-LE, Coherent, Santa Clara, USA) over 60 sec before every cutting procedure. During the experiment, the average output pulse energies ranged from 53 µJ to 68 µJ at a repetition rate of 1 kHz. The energy per pulse was adjusted via the electrical current for the pump diodes within the Nd:YAG laser to obtain an average fluence of 1 J/cm^2 at the end of the blunt fibre tip.

3.2.3. Simulation of Laser Light Output for Different Fiber Geometries

To visualize the laser light output from the fibre tip to the tissue, simulations were performed using a commercial optical raytracing software (Zemax, Version Optical Studio 14.2, Radiant Zemax Europe Ltd. Stansted, United Kingdom) in "non-sequential ray tracing mode". This mode ensures that a single optical ray can intersect with an optical surface more than once. However, this mode is based on simple geometrical optics, and doesn't take into account diffraction phenomena. Since a multimode fibre was used and the width of the rectangular endface for the blunt fibre tip was more than 5 times larger than the used wavelength, diffraction phenomena were neglected in this first proof-of-principle study. The simulation layout for the fibre tip ray output and the contained components are shown in figure 3.2.

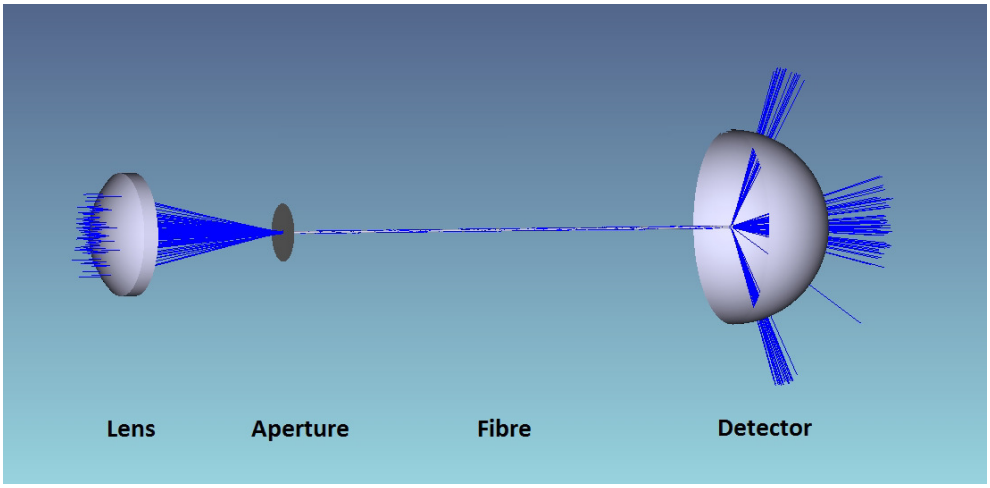

Figure 3.2. – Schematic of the simulation layout for the light output from the fibre tips consisting of a lens, an aperture, a fibre and a spherical detector. The blue lines indicate the simulated light rays.

As input light source, a circular collimated Gaussian beam was used with a Gaussian beam radius of 2.4 mm. The number of total rays for the simulation was 50 000. The next object in the simulation was a CaF_2 lens with a focal length of 20 mm to couple the laser light into the optical fibre. The geometry of the lens was modeled on the basis of geometric data of the lens. In a distance of 20 mm in z-direction, an aperture was placed with an inner radius of 0.125 mm representing the fibre radius. The resulting numerical aperture of 0.12 from the Gaussian beam radius of the input light source

and the focal length was matched to the numerical aperture of the sapphire fibre of 0.12. The numerical aperture of the fibre defines the maximal acceptance angle. The sapphire fibres with different shaped endfaces were externally modeled in a CAD-Program. The modeled fibres had a cylindrical shape with a diameter of 250 µm, a length of around 500 mm and were bent two times with a curvature radius of 50 mm to obtain a flattop beam profile within the sapphire fibres (Appendix A). The fibre tips were exactly formed like those which were fabricated for the laboratory experiments. The modeled fibres were loaded as step- files into Zemax and as refractive index 1.71 for 3 µm wavelength was used [104]. To obtain a beam image of the fibre tip output in the near- and the far-field, two different detectors were modeled. For the near-field, a rectangular detector with a size of 500 µm x 500 µm was directly placed at the fibre end. The second detector for the far-field had a spherical shape with a radius of 10 mm and the sphere center was at the fibre tip end.

3.2.4. Specimen Preparation

The new fibre tip designs were tested with samples of pig skin and liver tissue. All tissue samples were harvested in the morning and were used for experiments on the same day. The skin hairs were already removed via scalding. Until used in the experiments, the samples were kept at room temperature, and skin and liver samples were cut into sample pieces with uniform thickness to achieve an even horizontal surface on the sample stage for the subsequent experiments. The extracted specimens were stored in DPBS (Dulbecco's Phosphate Buffered Saline 1x, gibco^{TM} Thermo Fisher Scientific, Waltham, USA). Directly before the cutting experiments, a thin NaCl film (Isotone Irrigation solution 0,9 %, Braun) was put on the specimens. After cutting, the tissue samples were immediately fixed in phosphate-buffered 3.5 % formaldehyde.

3.2.5. Cutting Procedures

For the experiments the tissue samples were fixed under tension via pins on a cork plate. A polishing fibre adapter (KrellTech, Neptune, New Jersey, USA) with a conical ferrule was used as hand piece. While cutting the tissue, the optical fibre was positioned almost perpendicular to the tissue and the fibre tip was orientated in a way that the long side of the cutting surface was parallel to the cutting direction. The desired fibre tip orientation was verified by coupling incoherent white light into the fibre to obtain its orientation from the resulting light pattern at the end of the fibre tip. Two different cutting modes were tested: Free hand operation without defined speed and a fixed positioned fibre tip in combination with a moving translation stage with defined

speed. In the free hand operation, the fibre tip was moved by hand and pressed with sufficient pressure against the tissue to obtain a steady contact between fibre tip and tissue. In order to standardize the cutting tests, in the second mode, the fibre tip position was fixed in tight contact with the tissue so that enough tension was applied on the sample surface for cutting. The cork plate was mounted on a linear translation stage to move the sample with a defined speed. The speed of the translation stage was set to 1 mm/s as preliminary tests showed good cutting outcomes at this setting. Significantly faster cutting procedures led to increased tearing of the samples visible to the naked eye and broken fibre tips. In the literature, similar cutting speeds are reported: Bredikhin *et al.* used cutting speeds of 0.07 mm/s to 0.36 mm/s for experiments with an optical fibre tip outfitted with an absorptive layer and Stock *et al.* [101] 3 mm/s for the conical shaped fibre tip. Since the blunt fibre tip has negligible losses at the side faces due to the fibre angle, the whole emitted beam at the tip surface was measured for calculating the fluence with the energy meter and as rectangular area 25 µm x 250 µm was used. For the sharp fibre tip a fluence indication is not very useful, because no plane endface exits. Since one goal of the new fibre tip concept is to reduce the needed laser energy for cutting tissue, for the blunt fibre tip an average fluence of around 1 J/cm^2 was applied in the experiments. The same average pulse energy was also used in case of the sharp fibre tip to apply a comparable amount of energy to the tissue. The fibre tip was moved several times over the same incision to achieve a sufficient cutting depth. The translation stage was moved to create a 10 mm long cut. For each fibre tip shape and operation mode, three tissue samples were cut in skin and liver. In addition, cuts with a conventional scalpel were performed in skin by an experienced surgeon to compare the cutting outcomes.

3.2.6. Confocal Laser Scanning Microscopy (CLSM)

Three-dimensional images of the ablated tissues were acquired with a Confocal Laser Scanning Microscope (C2+, Nikon GmbH, Düsseldorf, Germany) equipped with a 4x objective (Plan Apo Lambda 4X/0.20, Nikon GmbH). Beforehand the plasma membranes of the cells were stained with CellMask Orange Plasma Membrane Stain (Thermo Fisher Scientific Inc., Waltham, MA, USA) diluted 1:1000 in phosphate buffered saline (PBS, Sigma-Aldrich Chemie GmbH, Hamburg, Germany) for 15 min. Hoechst 33342 was used to stain the cells' nuclei. The tissues were imaged in wet state in PBS. A 543 nm HeNe laser (Melles Griot GmbH, Bensheim, Germany) was used for excitation of the Orange Plasma Membrane Stain fluorescence. A 405/488/543/640 beamsplitter (Nikon GmbH) combined with a 595/50 bandpass emission filter (Nikon GmbH) was used to separate the excitation from the emission light.

3.3. Results

After cutting numerous samples, the intactness of the fibre tip and signs of abrasion on the tip were reviewed under a light microscope. Figure 3.3 shows a blunt fibre tip after cutting liver and skin samples. The edges of the fibre were completely intact, only the number of smaller scratches increased and tissue residues were found to stick to the tip. However, two blunt fibre tips broke during cutting skin tissue in preliminary experiments using the translation stage with higher speed. After cutting, no severe damage of any shaped fibre tip was observable in liver tissues.

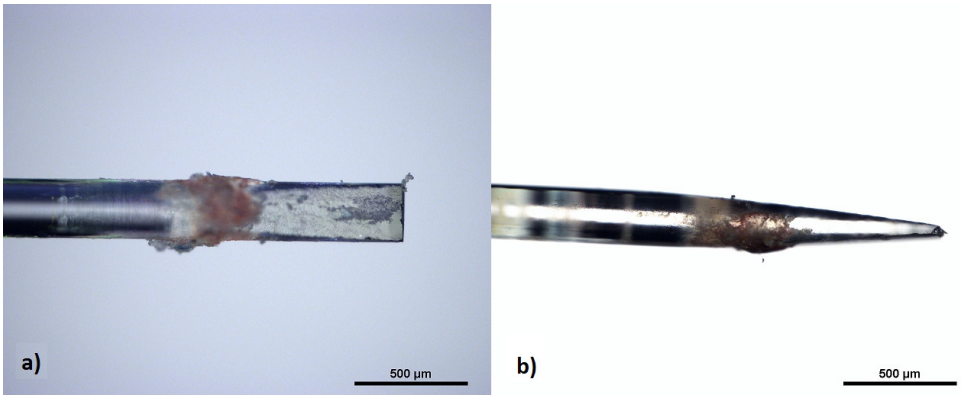

Figure 3.3. – The blunt fibre tip after cutting liver and skin tissues. Top view (a) and side view (b) on the polished fibre tip showing that the number of smaller scratches increased compared to microscope images captured before cutting. In addition, tissue residues were found to stick to the tip.

3.3.1. Simulation and Measurement of Laser Output Beam Profiles for Different Fiber Tip Geometries

For the different fibre tip geometries, the distribution of the calculated rays is shown from the side, at the end of the fibre tip and in the far-field for the transition to air in figure 3.4. The same views are also shown for the interface between the two fibre tips and water representing the tissue in figure 3.5.

The side view on the blunt fibre tip (a) in air shows that a large proportion of the laser light leaves the fibre tip at the flat end. In contrast to the sharp fibre tip (b), where a large fraction of the laser light leaks out from the polished side areas as expected

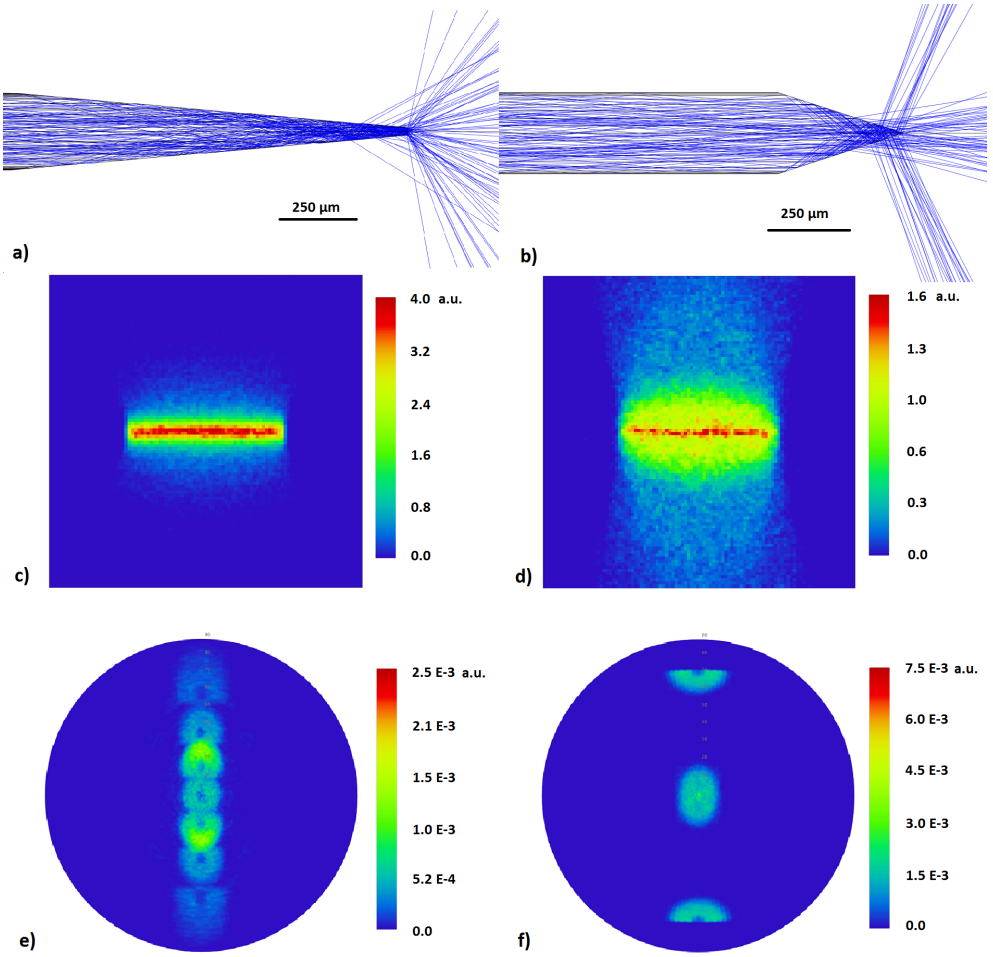

Figure 3.4. – The distribution of the calculated rays is shown in air from the side, in the near-field and far-field. A side view on the simulation of rays propagating to the blunt (a) and the sharp (b) fibre tip is presented. The laser light intensity distribution in the near-field directly at the fibre end tip is shown on the rectangular detector for the blunt (c) and sharp (d) fibre tip. The laser light intensity distributionin in the far-field is shown on the spherical detector in a distance of 20 mm from the fibre end tip for the blunt (e) and sharp (f) fibre tip. The color bars represent arbitrary intensity units.

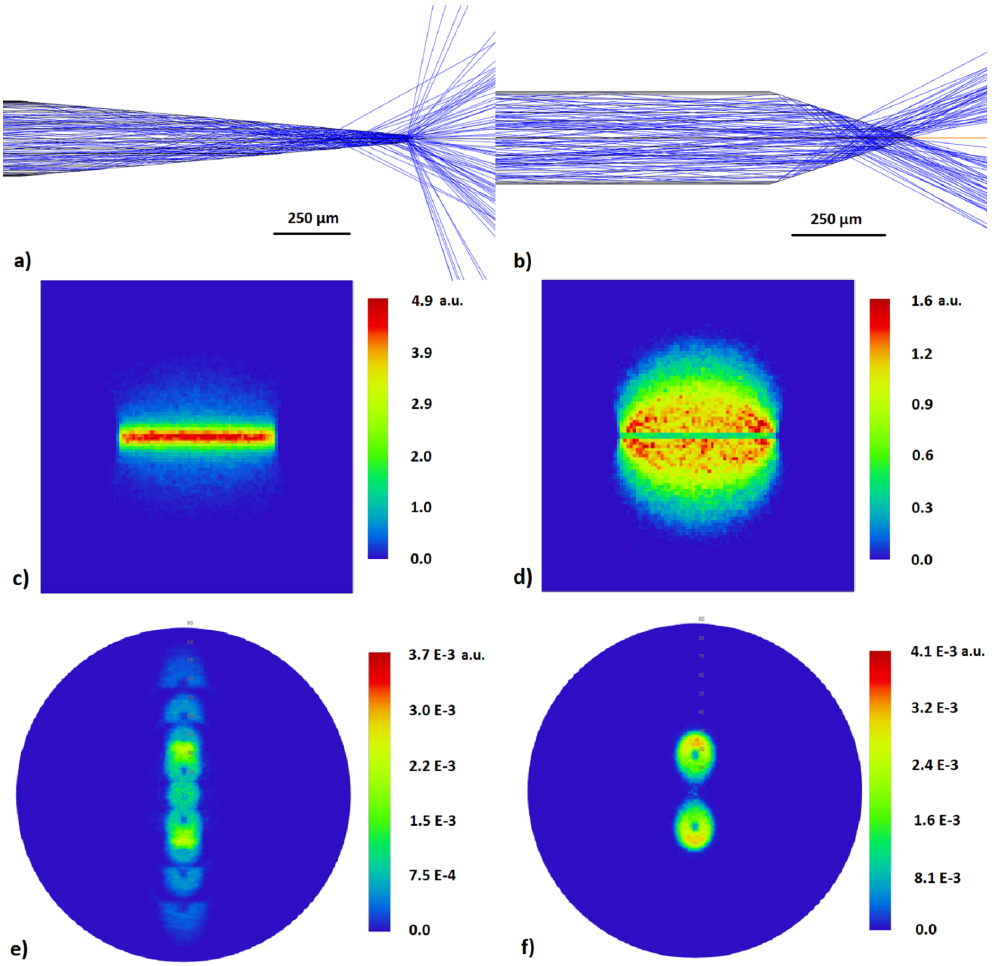

Figure 3.5. – The distribution of the calculated rays is shown in water from the side, in the near-field and far-field. A side view on the simulation of rays propagating to the blunt (a) and the sharp (b) fibre tip is presented. The laser light intensity distribution in the near-field directly at the fibre end tip is shown on the rectangular detector for the blunt (c) and sharp (d) fibre tip. The laser light intensity distributionin in the far-field is shown on the spherical detector in a distance of 20 mm from the fibre end tip for the blunt (e) and sharp (f) fibre tip. The color bars represent arbitrary intensity units.

due to the fibre angle of 18°. The intensity distribution of the laser light directly at the fibre tip end in the near-field exhibits an almost rectangular intensity distribution for the blunt fibre tip (c). For the sharp fibre tip (d), intensity maxima are visible at the sharp edge at the end of the fibre tip decreasing outwards in the near-field. Since the intensity distribution is less spatial confined in case of the sharp fibre tip (d), the maxima show a lower intensity than in case of the blunt fibre tip (c). In the far-field, several beam spots are visible in the simulation for the blunt fibre tip (e) and three spots perpendicular to the sharp edge for the sharp fibre tip (f). The number of beam spots and their spatial arrangement depend on the fibre tip angle. The flatter the angle, the more beam spots arise in the far-field. An explanation for this pattern is that with a flatter fibre angle, the laser light is reflected more often on the tapered fibre tip surface and in consequence more beam spots occur in the far-field.

For the transition of the laser light from the fibre to water with a refractive index of 1.27 at a wavelength of 2.94 µm, in case of the blunt fibre tip the laser light intensity distribution is only slightly changing compared to the the laser light intensity distribution in air. However, for the sharp fibre tip the laser light intensity distribution is different in the near- and far-field. The exit angles of the rays are considerable different and all rays exit in side-direction, however, not as steep as in air. For this reason, no intensity maxima are observable at the sharp edge and the area of the intensity distribution is smaller. In the far-field, instead of three beam spots only two are visible and located far closer. To calculate an exact fluence for the sharp fibre tip, the shown near-field image is impractical, since the rays are divergent and have already exited the side surface before. However, it can be estimated that the fluence is significantly lower. Thus the tissue cut is dominated by the mechanical forces of the sharp edge of the fibre tip and the laser light is playing a minor role.

To qualitatively verify the simulations, the laser output was measured in the far-field. For this purpose, a beam imaging camera was placed in a distance of a few mm from the fibre tip. Images of the near-field were not captured, since the camera sensor is very expensive and can be easily damaged by the fibre tip. Due to the spherical shape of the detector in the simulations and limited detector size of the beam imaging camera, a picture with all beam spots in a line as shown in 3.4 could not be captured for the blunt fibre tip. However, the pattern was clearly visible on a mid-infrared viewer card and could be also seen, when visible light was coupled into the fibre. Figure 3.6 shows the beam imaging pictures in the far-field on the beam camera for light with a wavelength of 3 µm (a) and the output after coupling visible light into the fibre (b). In both cases, several beam spots in a line are visible for the blunt fibre tip.

The images from the beam camera are consistent with the simulation. The blunt fibre tip showed several beam spots, while the sharp fibre tip had only three beam spots.

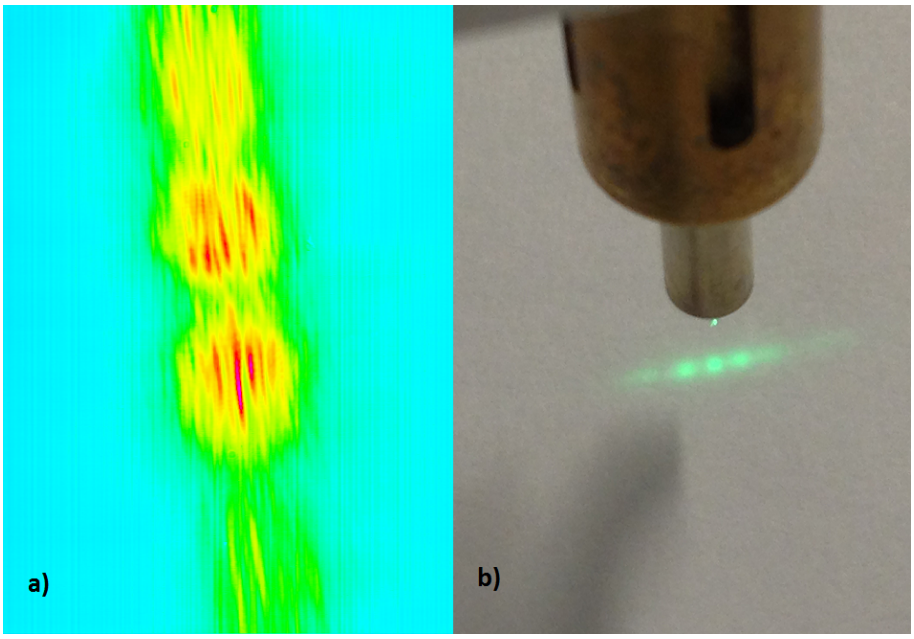

Figure 3.6. – Beam output after the blunt fibre tip imaged on the microbolometer camera (a) and after visible light was coupled into the fibre (b). Several beam spots in a line are visible on the beam imaging camera and show a qualitative agreement with the simulations. The interference patterns within the beam spots result from camera artifacts. Visible light shows similar patterns in the far-field for the blunt fibre tip.

3.3.2. Cutting Results

Although the tissue samples were fixed on the cork very carefully to avoid unevenness at the sample surface, it was difficult to receive reproducible results with the fixed handpiece and the moving stage. The unevenness of the surface was still in some samples too high and as a result very irregular cuts in terms of cutting depth were observable. In conclusion, only the second operation mode was further evaluated, where the fibre tip was manually pressed against the tissue to compensate the inequality of the tissue surface.

The induced incisions were photo-documented and are presented in figure 3.7. Since the tapered fibre tips were manually guided, only a qualitative evaluation of the induced cuts is reasonable. Both in liver and skin tissues, the incisions conducted by the two

fibre tips designs showed no relevant difference to the naked eye. In liver, the cuts were relatively uneven for both tip designs, whereas in skin the cutting surfaces seemed to be smoother.

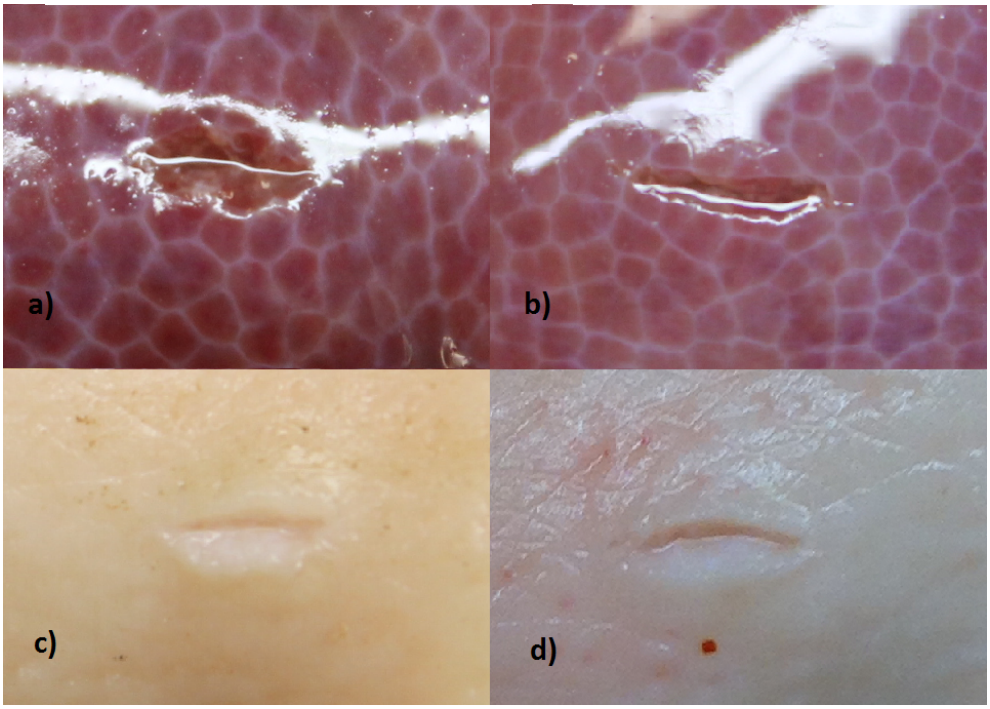

Figure 3.7. – Representative incisions created by the new fibre tip designs with a length of around 5 mm. Top views on cuts with a sharp fibre tip in liver (a) and in skin (c). In comparison, incisions created by a blunt fibre tip in liver (b) and in skin (d). The samples were fixed by pins to create tension on the tissue surface. No significant differences between the performed incisions by the two distinct tip designs were observable by the naked eye.

The tissue cuts performed by a scalpel and by the sharp fibre tip were investigated in greater detail, since the fibre tip shape is almost equal to the one of the scalpel and no significant difference in cutting compared to the other fibre tip design was observable. Via CLSM the cutting width was estimated for incisions made by the scalpel and the sharp fibre tip in skin. A representative picture for a scalpel cut in skin tissue is displayed in figure 3.8 and a picture for the best incision created by the shaped fibre tip in figure 3.9.

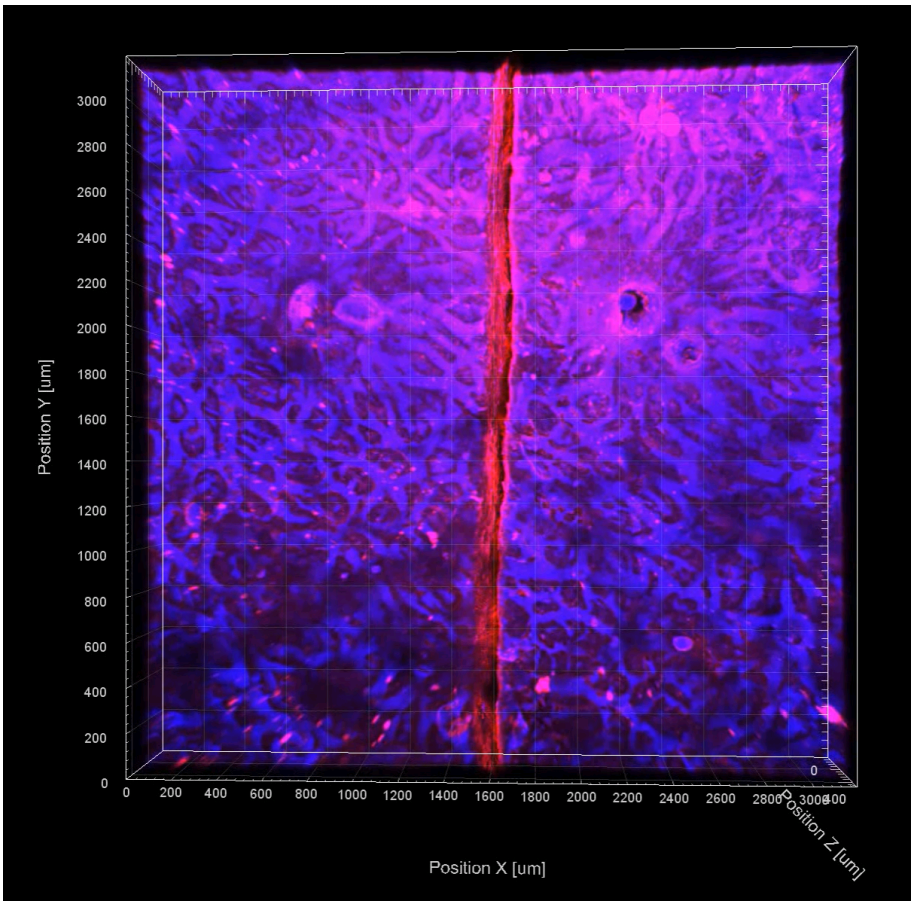

Figure 3.8. – Top view of a 2D dataset of a representative incision with a scalpel in skin imaged by Confocal Laser Scanning Microscopy (CLSM). The sample was stained with CellMask Orange Plasma Membrane Stain (red) and Hoechst 33342 (blue) for the CLSM image. The scalpel cut had an approximated cutting width of around 100 µm on the skin surface and was relative straight and even.

The scalpel cut was relative straight and even with an approximated cutting width of around 100 µm on the skin surface, whereas the incision induced by the shaped fibre tip is more unsteady and wider with an estimated width of 300 ± 100 µm. The red cut surface of the scalpel incision indicates no tissue damage and no statement regarding the cut quality can be made. It results only from the fact that the surface was not shadowed during imaging.

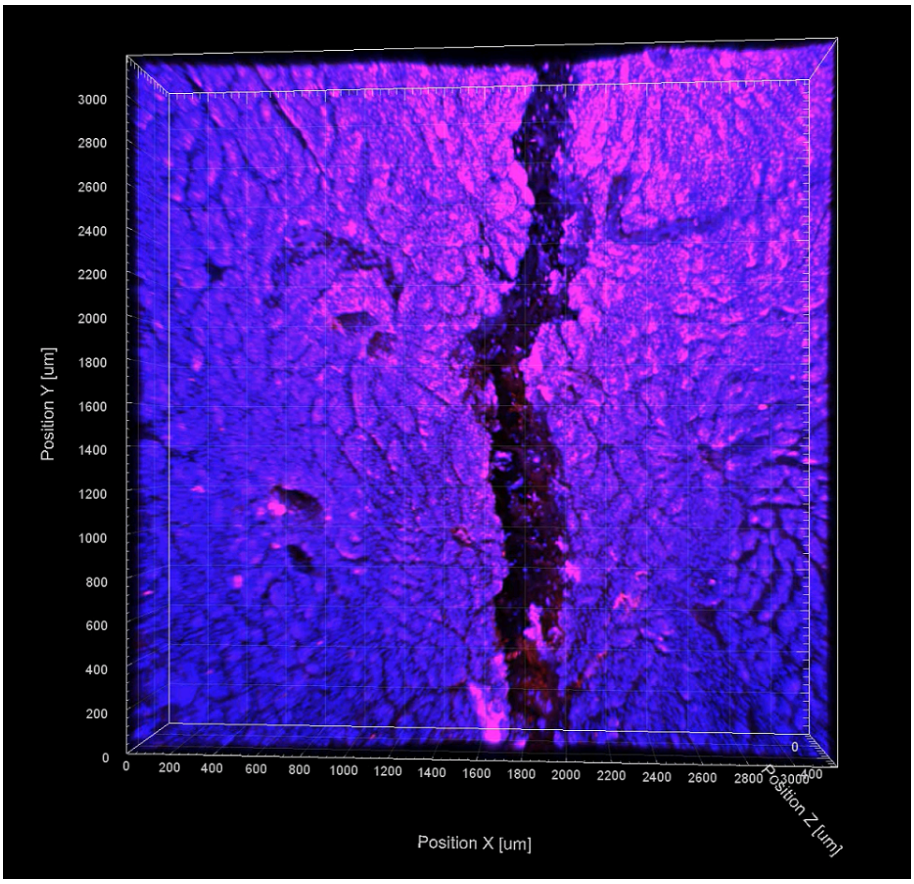

Figure 3.9. – Top view of a 2D dataset of an incision with a tapered fibre tip in skin imaged by Confocal Laser Scanning Microscopy (CLSM). The sample was stained with CellMask Orange Plasma Membrane Stain (red) and Hoechst 33342 (blue) for the CLSM image. The incision induced by the shaped fibre tip is more unsteady and wider with an estimated width of 300 ± 100 µm compared to the scalpel cut.

3.4. Discussion

The present experiments for cutting tissue by a hybrid laser and mechanical method can only be evaluated as a first proof-of-principle approach. Nevertheless, observed outcomes warrant a more detailed discussion of some aspects.

The optical simulations with simple ray tracing allowed visualizing the laser light intensity distribution for the two different tip geometries in the near-field directly at the end of the shaped fibre tips and in the far-field. For the cutting application only the near-field intensity distribution is relevant, since the laser light is absorbed in tissue within a few micrometers for the 3 µm wavelength. The simulations for the far-field and the subsequent measurement of the laser output were only used to qualitatively verify the simulations. Although a larger ratio of the laser light leaves from the polished side areas in case of the sharp fibre tip compared to the blunt fibre tip, the first one seems to be more mechanically stable as it cuts tissue. However, the geometrical design regarding internal laser light reflection within the shaped fibre tip is superior in case of the blunt fibre tip. Moreover, the laser light is directly emitted at the 25 µm wide cutting surface. This design represents more the original idea of combining laser light with the mechanical cutting forces.

Another important aspect is that conventional laser surgery normally cuts by ablation and the depth of cutting is limited by scattering as the cut gets deeper. Typically, the laser is used in a mode in which the top tissue region must be widened as the cut is made deeper. This process leads to much slower cutting, and much more loss of tissue than would be necessary. The present fibre tip design provides a self-guided shear force application that opens up the tissue during the cutting process to allow in principle deeper cutting without widening the incision width at the surface. However, the estimated cut width of up to 400 µm for the shaped fibre tip is wider than expected, since the fibre diameter above the shaped fibre tip is 250 µm. This can result from free hand operation and the cutting procedure itself, where the fibre tip was moved several times over the same incision to achieve a sufficient cutting depth. Although the cut width is larger than the width of the scalpel cut, it is still smaller than a cut performed with a fibre tip having a strong absorbing coating. In Bredikhin *et al.* [96], the width of the incision was around 870 µm, when such a device was employed.

Moreover, an advantage of the fibre tip over a metallic scalpel is that the cutting edge does not get blunt after a short period of time and is reusable. However, a disadvantage compared to the metallic scalpel is that the fibre can break, if it is not applied with care. Another disadvantage with respect to the conventional scalpel is the obtained non-straight cutting line of the incision using the shaped fibre tip guided by free hand. The *in vitro* test cuts on porcine oral mucosa made with a shaped fibre tip tapered from a 800 µm cylindrical sapphire fibre to a diameter of 200 µm in Stock *et al.* [101] revealed very irregular cutting lines as well. Nevertheless, the test cuts with the conically shaped tips showed a better cut quality and led to an increase in efficiency with regard to cut depth compared to cuts with a plane bare fibre. The applied output power of the conical shaped fibre tip on porcine oral mucosa was relatively high with 5 W and 7 W in contrast to the applied PIRL power of 60 to 70 mW.

For all other laser classes not using plasma-induced ablation, irradiations of the tissue at dose levels higher than 1 J/cm^2 are needed to effectively ablate the tissue. The new design in case of the blunt fibre tip enabled to deposit the laser energy at the end of the fiber tip within a width of tens of micrometers at the interface to the tissue. This reduces the required pulse energies to achieve a sufficient fluence for ablation. With this new tip design the needed laser power for cutting can be reduced and low-power lasers could be theoretically used. However, this tool is more suitable for microsurgical procedures; the relatively low cutting speed suggests an application in the microsurgical field.

For further experiments, the shaped fibre tip can be guided by a robotic arm to further reduce the width of incisions and achieve more straight cutting lines. With distance measurement via OCT, the fibre tip could be guided with steady contact to uneven tissue. However, the decisive experiments will be *in vivo* studies with the influence of blood, since bleeding is always an issue in surgical operations. Other fibre tip designs address this issue by strongly coagulating the tissue with the disadvantage of extensive tissue damage zones.

3.5. Conclusion

In a first straight forward approach, a new cutting method for soft biological tissue combining laser light and mechanical shear force through a shaped optical fibre has been examined. Two shaped fibre tip designs were realized by polishing two opposing sides of the fibre tip to obtain a 25 µm wide endface or a fibre tip with a sharp edge without a planar endface. The laser light intensity distribution was calculated via an optical ray-tracing software in the near- and far-field for the two fibre tip geometries to choose sufficient pulse energies for tissue cutting. Tissue cuts in skin and liver conducted with the shaped fibre tip designs showed no relevant difference between both. The incisions performed with the sharp fibre tip were imaged by Confocal Laser Scanning Microscopy. Although the cuts were more irregular and the cut width wider compared to a scalpel cut, the new cutting method delivered more precise cuts compared to other incisions performed by other fibre tip designs in literature. With the PIRL-DIVE laser tissue interaction characteristics in mind, the envisioned advantages of such an approach are unique. The main advantage of the new fibre tip designs is envisioned that the needed laser energy could be reduced compared to cuts with plane bare fibres or free beam applications. However, the current approach doesn't coagulate the tissue in order to stop bleeding. It should nevertheless be relatively straight forward to use standard wavelength division multiplexing fibre optic components to enable the use of additional laser wavelengths at 400 nm or 532 nm for controlled coagulation to

stench bleeding. Another advantage over a conventional scalpel is that the diamond tip doesn't get blunt during the cutting procedure. After this first proof-of-principle experiment, additional optimizations such as the use of robotics for better controlled cutting are necessary in further *in vitro* experiments. The effects of the fibre orientation angle regarding cutting depth can be evaluated in these experiments.

4. Proteome Analysis of Tissues in Bio-diagnostics: Comparison of Two Infrared Lasers

The following chapter will form the basis for a manuscript in preparation: A. Krutilin[1], S. Maier[1], R. Schuster, S. Kruber, M. Kwiatkowski, W. D. Robertson, D. R. J. Miller, and H. Schlueter, Sampling of Tissues with Laser Ablation for Proteomics: Comparison of Picosecond Infrared Laser (PIRL) and Microsecond Infrared Laser (MIRL).

The author conceived the experiment, led the experimental campaign with contributions from all co-authors, and contributed to data analysis and manuscript writing.

This chapter compares the ablation pattern results, the weight range of extracted proteins collected within the ablation plume, the number of identifiable proteins, and the enzymatic activity in three different tissues for two 3 µm lasers with pulse durations in the picosecond and microsecond range.

4.1. Introduction

Proteomics is the science of the entire set of proteins and has been a fast growing field in life science over the last decades. Proteins are crucial for almost every biological function, from controlling gene expression as transcript factors to catalyzing cellular reactions as enzymes [106]. And mass spectrometric analysis techniques enable unique understanding of complex biological processes in terms of composition, structure and function of the proteome [107]. Moreover, proteins and peptides are biochemical markers for various diseases and morphologic structures. As already mentioned in chapter 1, MALDI- mass spectrometry imaging introduced in 1997 by Caprioli *et al.* [108] is a prominent application in medicine for analyzing distributions of biomolecules in tissues.

[1] authors contributed equally.

In order to extract proteins out of their native environment for disease-related biochemical analysis, a crucial first step is the homogenization, i. e. the disruption of cells in the sample. Normally this step is realized by mechanical methods as using metal beads or mortar and pestle [109, 110]. In the following step, the proteins must be separated from DNA, RNA and other small organic molecules.

Today, laser-assisted homogenization allows fast and effective protein extraction. Specifically, lasers with a wavelength of 3 µm tuned to the OH-vibrations are effective tools for the extraction of biomolecules. Direct analysis of biological materials in their native environment with mass spectrometry, so-called ambient mass spectrometry, was conducted by Park *et al.* [111] using an infrared optical parametric oscillator (OPO) laser system at 2.94 µm wavelength with a pulse width of 5 ns and a pulse energy of 1.75 mJ. Via the laser the biomolecules were ablated from a sample and the ejected biological material was captured in a solvent droplet positioned above the sample surface. Subsequently, the droplet was analyzed on a MALDI target or flow-injected via Electrospray into a mass spectrometer. Pure peptides, proteins and complex biological samples were ablated and the authors stated that mass spectrometry analysis showed little to no signs of sample degradation for either peptides or proteins or fragmentation of biomolecules.

A laser ablation sampling technique for MALDI- mass spectrometry of tissue samples was developed by Donnarumma *et al.* [112]. The new sampling technique used the same laser system as Park *et al.* [111] to analyze rat brain, lung tissue, and tryptic peptides. In contrast to conventional MALDI-MS analysis, the samples were ablated by a laser, subsequently vacuum captured and then analyzed by MALDI-MS. The new method showed a greater signal intensity and lower background for tissue samples compared to conventional MALDI-MS analysis. In a further study, the infrared laser showed a higher reproducibility compared to ultraviolet laser capture microdissection [113]. Moreover, Kwiatkowski *et al.* showed that a sample preparation procedure via DIVE laser ablation with the PIRL laser extracts not only proteins over a broader weight range compared to mechanical methods, but also more efficient in terms of protein yield [114]. In addition, the procedure is less time consuming compared to conventional techniques.

Given the DIVE concept is not only capable of ultrafast protein extraction, but also promising for surgery, the PIRL has been compared in several studies to a conventional Er:YAG laser with microsecond pulse durations as a surgical tool [39, 41, 45, 46]. However, to the best knowledge of the author laser-driven protein extraction with a conventional microsecond Er:YAG laser has not been investigated so far. For this reason, the extraction of proteins from tissues was compared between the PIRL ablation and conventional Er:YAG laser ablation in this study. In previous studies, the maximum

temperature rise within the ablation site was measured via a thermography camera and ranged in case of PIRL ablation from $\delta T = 1.6$ K to $\delta T = 4$ K and for Er:YAG ablation between $\delta T = 13$ K and $\delta T = 172$ K in different tissues [40, 45, 46]. However, these values should be considered with caution, since the temporal resolution was in the 10 millisecond time interval for the thermography camera and the theoretical temperature rise on the picosecond timescale should be in the range of 1000°C neglecting the cooling effect due to adiabatic expansion. Therefore, much higher peak temperatures inside the ablation side are possible for ablation with PIRL, but also with an Er:YAG laser.

The thermal denaturation of proteins depends not only on the absolute temperature rise within the ablation zone, but also on deposition time of the applied energy in terms of laser pulse duration. Thermal denaturation or degradation in proteins can be distinguished in unfolding events losing their tertiary and quaternary structure or bond breaking events in the primary structure, respectively. Temperature spikes of up to 290°C over tens of nanosecond were necessary to produce an irreversible loss of enzyme activity [115]. A possible speed limit for thermal unfolding of large proteins was stated to be in the order of 10^{-8} seconds. For this reason, for the protein extraction via PIRL intact enzyme activity is expected in contrast to conventional Er:YAG lasers.

4.2. Materials and Methods

4.2.1. Laser Systems and Ablation Chamber

A prototype picosecond infrared laser (PIRL -HP3-1064 OPA -3000, Attodyne Inc., Toronto, Canada) and a commercial Er:YAG laser (MEY-1-A EX-2, J Morita Mfg Corp., Kyoto, Japan) were used to perform the ablations. Both lasers emitted Gaussian shaped beams with a wavelength of 3000 ± 90 nm for the PIRL and 2.94 µm for the Er:YAG laser. The pulse widths of the PIRL and Er:YAG laser were 400 ps and 300 µs, respectively. Both lasers were coupled to a home-build scanning system with an autofocus function, which kept the beam waist constantly on the tissue during the ablation of rectangular scan patterns with a size of 4 mm x 4 mm. Within the scan patterns the consecutive laser pulses were overlapped with a peak-to-peak distance of 50 µm (PIRL) and 200 µm (Er:YAG laser). The beam spot sizes in the focus of both lasers were measured by a Silicon Microbolometer Beam Imaging Camera (WinCamD-FIR-2-16HR, DataRay Inc., Redding, USA). Since the Er:YAG laser and PIRL had different pulse durations, the threshold of the fluence needed for initiating the ablation process was for PIRL lower than for the Er:YAG laser with a longer pulse

duration [92]. Moreover, the Er:YAG laser had a considerable smaller repetition rate than PIRL. To collect enough sample material in a short time period for the subsequent mass spectrometry analysis in case of the Er:YAG laser, a higher fluence was chosen for the experiments. For that reason, the laser pulses for ablation were adjusted to achieve an average fluence of 1 J/cm^2 for PIRL and 40 J/cm^2 and 60 J/cm^2 for the Er:YAG laser on the sample stage. It was expected, that the higher fluences for the Er:YAG laser compared to the PIRL had no crucial influence on the experiment, since the peak irradiance per pulse, for PIRL was with 2.53 GW/cm^2 still orders of magnitude higher than for the Er:YAG laser with 0.19-0.38 MW/cm^2. However, the particle size in the ablation plume correlates with the penetration depth of applied laser pulses [37]. Thus, a higher fluence as in case of the Er:YAG laser led to a higher penetration depth and bigger particles in the ablation plume. The energy measurement of the laser pulses was conducted with a precision energy meter (LabMax-Top with Energymax Sensor J-25-MB-LE and J-25-MB-HE, Coherent, Santa Clara, USA) and the energy was measured before each ablation of a sample for 60,000 pulses (PIRL) and 1200 pulses (Er:YAG laser). Tab 4.1 shows an overview over all laser settings and beam characteristics.

Parameters	**PIRL**	**Er:YAG laser**
Wavelength	3 µm	2.94 µm
Pulse width	400 ps	300 µs
Repetition rate	1000 Hz	25 Hz
Beam Diameter ($1/e^2$)	$\sim$ 170 µm	$\sim$ 250 µm
Pulse energies (E_p)	230 µJ	28-56 mJ
Average pulse fluence (φ_a)	1 J/cm^2	40-60 J/cm^2
Peak pulse fluence (φ_p)	2 J/cm^2	80-120 J/cm^2
Peak power (P_p)	0.575 MW	93-187 W
Peak irradiance (I_p)	2.53 GW/cm^2	0.19-0.38 MW/cm^2

Table 4.1. – Laser settings and beam characteristics on the sample surface during ablation experiments for PIRL and Er:YAG laser.

The frozen tissue samples were placed inside a home-built ablation chamber on a copper block, which was constantly cooled down to -10°C via a Peltier element. The ablation chamber was connected by a PTFE tubing to a home-built cryo-trap consisting of a modified 15 ml falcon tube placed approximately 1 cm deep in liquid nitrogen and to a membrane pump (MZ 2 C VARIO, Vaccuubrand, Wertheim, Germany). Due to the vacuum, the ablation plume was collected, transported to the cryo-trap, and captured inside the falcon tube. The ablation time, 260 seconds, was controlled with a beam shutter (SH05, Thorlabs, Newton, New Jersey, USA) and the associated shutter controller (SC10, Thorlabs, Newton, New Jersey, USA). Image 4.1 shows a schematic

diagram of the ablation and collection setup.

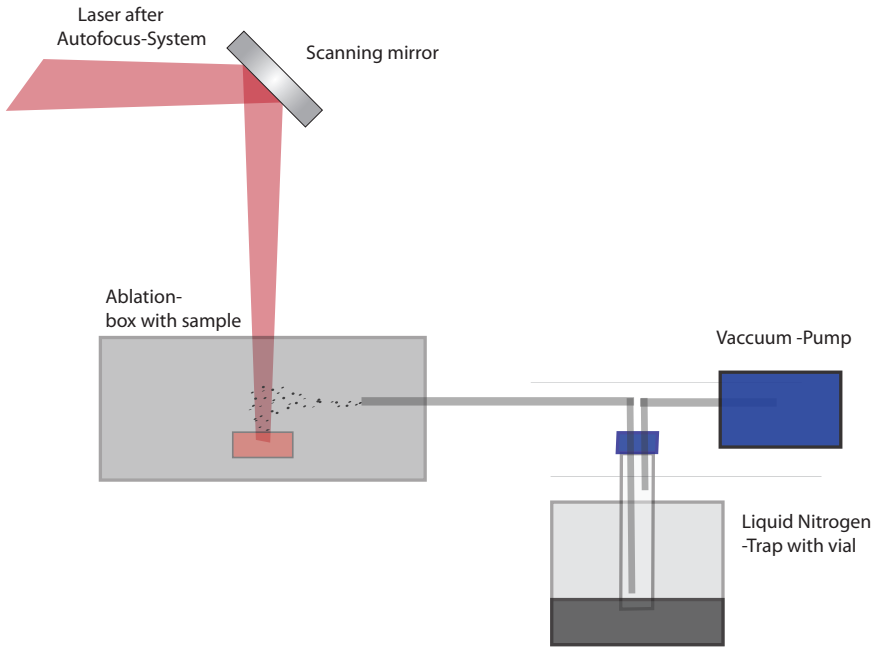

Figure 4.1. – Ablation and collection setup for the proteome analysis: The laser after the autofocus system, a scanning mirror to ablate a rectangle pattern, an ablation box with the cooled sample, a vacuum pump to transport the collected ablation plume, and a cryo-trap to capture the ablated sample.

4.2.2. Sample Preparation

Rat tissue samples from Wistar rats were received from the research animal husbandry of the Medical Center Hamburg-Eppendorf (UKE). The experiments were performed following the principles of the 3Rs in animal testing, namely replacement, reduction, and refinement. Thus, only tissue samples of rats were used that had been sacrificed for other projects. Fresh muscle, liver and kidney tissues were cut in four pieces, immediately frozen in liquid nitrogen and stored prior to ablation at -80°C. This freezing

immediately stops degradation processes in the samples and biochemical analyses are often performed after tissue samples were frozen. All muscle and liver tissue samples were analyzed by electrophoresis to cover the extracted protein weight range, while mass spectrometry was applied to investigate the number of identified proteins. Kidney samples were used to test the enzyme activity, since kidney tissue possesses high concentrations of enzymes [116]. The laser ablation and subsequent tissue analysis were conducted for both lasers within the same rat individual. After ablation, the frozen condensates were stored within the falcon tubes at -80°C.

Liver and Muscle Tissue

All frozen condensates of the ablated muscle and liver tissues were divided into two aliquots to subsequently perform a SDS-PAGE gel electrophoresis and a shot gun LC-MS/MS analysis.

For the SDS-PAGE gel electrophoresis, the frozen condensate was incubated with 100 µl heated Laemmli Buffer (Appendix B) for 5 minutes at 95°C to stop enzyme activity. To separate the proteins from the other constituents, the specimens were centrifuged at 15,000 x g for 3 minutes. The supernatants were transferred into a separate reaction vial and stored at -20°C. In order to prepare a comparable amount of protein in each SDS-PAGE well, the protein concentration was measured with a 2D Quant Kit (GE Healthcare Life Science, Freiburg, Germany).

For the shot gun LC-MS/MS analysis, the second aliquot was mixed with 6M Urea in a ratio of 1:1 and centrifuged at 15,000 x g for 3 minutes. The supernatants were transferred to a separate vial and stored at 4°C until the tryptic digestion. The tryptic in-solution digestion was performed in accordance with Wisniewski *et al.* [117].

Kidney Tissue

Prior to the enzyme activity tests, the homogenates were stored at -80°C. Without any additional treatment the kidney tissue homogenates were incubated with Angiotensin-I (Ang 1-10, c=10^{-5} M in ultrapure water in a ratio of 1:9) at room temperature. The enzyme activity and its resulting degradation products were tested at different time points of 0h, 3h, 6h, and 24h. At each time point aliquots were mixed with a MALDI matrix (2,5-dihydroxybenzoic acid (DHB) c=20 mg/ml in 50 % ACN, 0.1 % TFA) in a volume ratio 1:2, which inhibited the enzyme activity.

4.2.3. Analytic Methods

As analytical methods, SDS-PAGE gel electrophoresis, shotgun LC-MS/MS and MALDI-TOF were applied.

The SDS-PAGE for the muscle and liver ablation products was prepared for a qualitative comparison, since only the extracted protein distribution based on weight can be determined. In the shotgun analysis, proteins can be identified in complex compounds by proteolytic digestion to determine their amino acid sequences and post-translational modifications [118, 119]. Therefore, normally high performance liquid chromatography is combined with mass spectrometry as in case of a LC-MS/MS analysis. The MALDI-TOF analysis was used to determine the enzyme activity by measuring the degradation products of angiotensin I (Ang 1-10).

SDS-PAGE Gel Electrophoresis

In each SDS-PAGE well, 30 µg homogenate was loaded onto the gel (Criterion^{TM} XT 10 % Bis-Tris gel, BioRad, Munich, Germany). For the electrophoresis, a voltage of 120 V was applied for 60 minutes. The protein staining (40 % MeOH, 10 % acetic acid, 0.025 % Coomassie Brilliant Blue G250, dissolved in ultrapure water) was performed overnight.

Shotgun LC-MS/MS Analysis

The LC-MS/MS data were acquired using reversed-phase ultra high-performance liquid chromatography (Dionex UltiMate 3000 RSLCnano, Thermo Scientific, Bremen, Germany) coupled via electrospray ionization (ESI) to a quadrupole orbitrap mass spectrometer (Orbitrap Fusion, Thermo Scientific, Bremen, Germany).

The same protein concentrations were injected into the LC-MS/MS system to ensure same conditions for the homogenates from the PIRL and Er:YAG laser ablation. After the injection with a total volume of 5 µl, the samples were loaded on a trapping column (nanoACQUITY UPLC Symmetry C18 trap column, Waters, Manchester, UK, further parameters in Appendix B) at a flow rate of 5 nl/min with a 2 % Buffer B (99.9 % H_2O, 0.1 % formic acid) for 5 minutes. In the next step, the analytes were transported to the separation column (nanoACQUITY UPLC column, BEH 130 C18, Waters, Manchester, UK, further parameters in Appendix B) and passed through with a flow rate of 200 nl/min. A 60 minutes separation gradient from 2 to 50 % of Buffer B was used to elute the proteins. For spray generation, a fused-silica emitter (I.D. 10 µm, New Objective, Woburn, USA) was used at a capillary voltage of 1650 V. LC–MS/MS analysis with the orbitrap was performed on MS level over a m/z range from 400 to 1500, with a resolution of 70,000 FWHM at m/z 200 (transient length = 256 ms, injection time = 100 ms, AGC target = 3e6). For data acquisition, the

mass spectrometer was performed in positive ion mode. In the LC-MS/MS raw data analysis, the proteins were identified from the raw data with the MaxQuant Software (Version 1.5.2.8, Max Planck Society, Munich, Germany) and the identification of peptides and proteins was carried out by the Andromeda search engine against the *rattus norvegicus* Uniprot-Swiss-Prot database (www.uniprot.org, downloaded January 29, 2016, 7934 sequence entries). The search parameters were defined to allow a precursor tolerance of 10 ppm and MS/MS tolerance of 0.6 Da, variable modifications of methionine oxidation as well as carbamidomethylation for cysteine residues, and two missed cleavages. Only those proteins were taken into account, which at least were identified with two or more unique tryptic peptides.

MALDI-TOF Analysis

The MALDI spectra were recorded via a TOF-mass spectrometer (Bruker UltrafleXtreme Smartbeam II Laser, Bremen, Germany) and each spectrum was generated through 2000 shots in partial sample mode. The instrument was operated in positive reflector ion mode, a repetition rate of 20 Hz, 40 % laser intensity, 20 kV first acceleration voltage, 18.5 kV second acceleration voltage, 250 ns extraction delay, and 500 to 5040 m/z range. Further parameters for the MALDI mass spectrometry measurement are in Appendix B).

4.3. Results

The ablated area exposed significant differences regarding thermal damage for the Er:YAG laser and PIRL. In figure 4.2, the tissue after ablating a 4 x 4 mm area is shown for PIRL and the Er:YAG laser. The ablated PIRL surface exhibited no signs of tissue burning to the naked eye, whereas in case of the Er:YAG laser brown burned tissue was visible. Due to the higher fluences in the case of the Er:YAG laser, the ablation depth per pulse was considerable higher on the order of several tens of micrometers compared to PIRL [81]. Therefore, a precise layer-by-layer ablation with an ablation depth per laser pulse of a few micrometers as in case of PIRL was not achieved in this experiment for the Er:YAG laser. The extracted proteins were qualitatively analyzed in SDS-PAGEs and an additional shotgun analysis was performed.

4.3.1. SDS-PAGEs and Shotgun Analyses

To obtain a first view on the kDa weight range of extracted proteins, SDS-PAGEs were conducted with a protein standard (SeeBlue Plus2 Pre/Stained Standard, Thermo

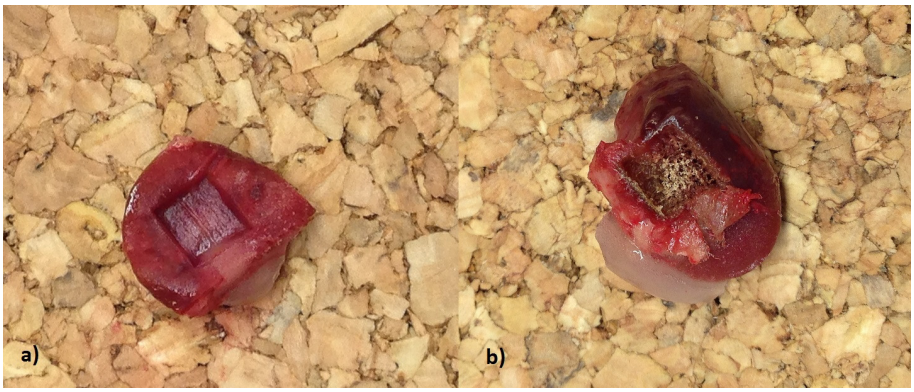

Figure 4.2. – Kidney tissue after PIRL (a) and Er:YAG laser (b) irradiation. A 4 x 4 mm area was irradiated in both cases and the ablated surface of the Er:YAG laser showed in comparison with PIRL clear signs of thermal damage by brown burned tissue residues. The adjacent tissue after PIRL irradiation indicated no significant alteration for the naked eye and appeared red and moist for the naked eye.

Scientific, Braunschweig, Germany). In addition, the homogenization techniques were compared with respect to the number of extracted proteins for the PIRL and Er:YAG laser in a shotgun analysis. To ensure equal conditions, the same concentrations were applied in both analytical techniques. Representative results of the protein extraction for both lasers are presented in form of the obtained SDS-PAGEs and VENN-diagrams in case of shotgun analysis in figure 4.3 for muscle tissue and in figure 4.4 for liver tissue. Two ablated PIRL samples with an average fluence of 1 J/cm^2 (I. and II.), a protein standard (PS), two Er:YAG laser samples with an average fluence of 40 J/cm^2 (III.) and 60 J/cm^2 (IV.) were applied in a separate loading pocket on each SDS-PAGE and were additionally analyzed via LC-MS/MS.

In case of both lasers, the SDS-PAGEs revealed a large number of bands reaching from a few kDa up to approximately two hundred kDa. A comparison between the SDS-PAGE patterns of the PIRL and Er:YAG laser ablated samples showed that distinctive bands from the PIRL extraction were also visible in the Er:YAG laser sample both in muscle and liver tissue. Even bands around 200 kDa were in the Er:YAG laser samples for both tissues. From these patterns, it can be concluded that both lasers were capable of extracting proteins over a similar weight range. However, the Er:YAG laser patters showed in the range under 10 kDa noticeable blurring in muscle tissue (Figure 4.3). To investigate the blurred area, bands in the range of 3 kDa to 6 kDa were cut off for both laser samples and tryptically digested after Wisniewski *et al.* [117]. LC-MS/MS analyses were performed and the data sets were searched against semitryptic

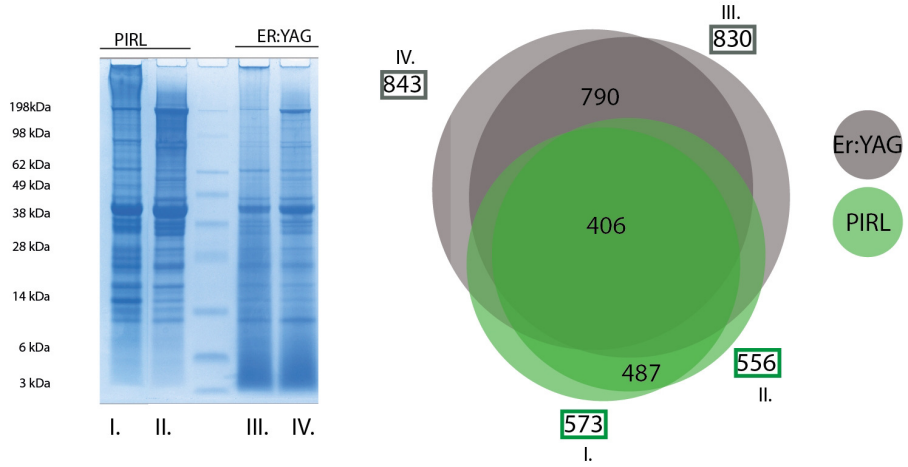

Figure 4.3. – SDS-PAGE and VENN-diagram of shotgun analysis of rat muscle tissue with PIRL (green) and Er:YAG laser (grey) system. The SDS-PAGE and the shotgun analysis were performed with two ablated PIRL samples with an average fluence of 1 J/cm^2 (I. and II.), a protein standard (PS), two Er:YAG laser samples with an average fluence of 40 J/cm^2 (III.) and 60 J/cm^2 (IV.). The comparison of the SDS-PAGE band patterns for both lasers indicated that similar proteins were extracted. In the PIRL condensates 573 proteins (I.) and 556 proteins (II.) were identified, in Er:YAG laser condensates 830 proteins (III.) and 843 proteins (IV.). The overlap of identical proteins within the two Er:YAG laser condensates was 790 proteins, and in case of PIRL 487 proteins. The overall overlap between all samples was 406 proteins.

and unspecific peptides. No significant amounts of peptides were found in both cut-off bands. This indicates that other molecules such as carbohydrates are responsible for the blurred area.

By means of the shotgun analysis, in the PIRL condensates of ablated muscle tissue 573 proteins (I.) and 556 proteins (II.) were identified, in the Er:YAG laser condensates 830 proteins (III.) and 843 proteins (IV.). Thus, higher protein numbers were observed in the Er:YAG laser samples. The energy pulse variation and the resulting varying fluence in case of the Er:YAG laser seemed not to play a role, since an almost similar number of proteins were detected. Within the Er:YAG laser samples, 790 identical proteins were determined and 487 identical proteins within the two PIRL condensates. Between all PIRL and Er:YAG laser samples an overlap of 406 identical proteins was found.

In rat liver tissue, the SDS-PAGEs showed a similar result than in muscle tissue (Figure 4.4). Over the full kDa range, proteins for both lasers were found. However, the blurred area under 10 kDa was not recognizable in the Er:YAG laser samples in contrast to muscle tissue.

In contrast to muscle tissue, the PIRL condensates of the liver tissue showed a remarkable higher number with 890 identified proteins (I.) and 810 proteins (II.) compared to condensates of the Er:YAG laser with 426 proteins (III.) and 535 proteins (IV.) in the shotgun analysis. The overlap of identical proteins between the PIRL samples was 771 proteins and between the Er:YAG laser samples 380 proteins. The overall overlap of identical proteins in all four samples was 326 proteins.

4.3.2. Test of Enzymatic Activity

In a last step, the enzymatic activity of proteins in the condensate of the tissue aerosol was examined. Therefore the condensate of the ablated kidney tissue was incubated with angiotensin I (Ang 1-10). Angiotensin I is a prohormone in mammalian species and plays an important role in the renin angiotensin system (RAS) [120]. This system is a key factor for regulating the blood pressure and homeostasis. Angiotensin I can be processed into further angiotensin peptides by many proteases and in rats only N-terminal proteolytic cleavage exits [121]. Possible degradation products for Angiotensin I (Ang 1-10) as consequence of proteolytic activities are listed with mass-to charge relation and associated peptide sequence in appendix B.

The incubated Angiotensin I (Ang 1-10) and the degradation products were analyzed for PIRL and the obtained MALDI-TOF mass spectra are presented in figure 4.5. Only the strongest signals of the degradation products are labeled in the following spectra.

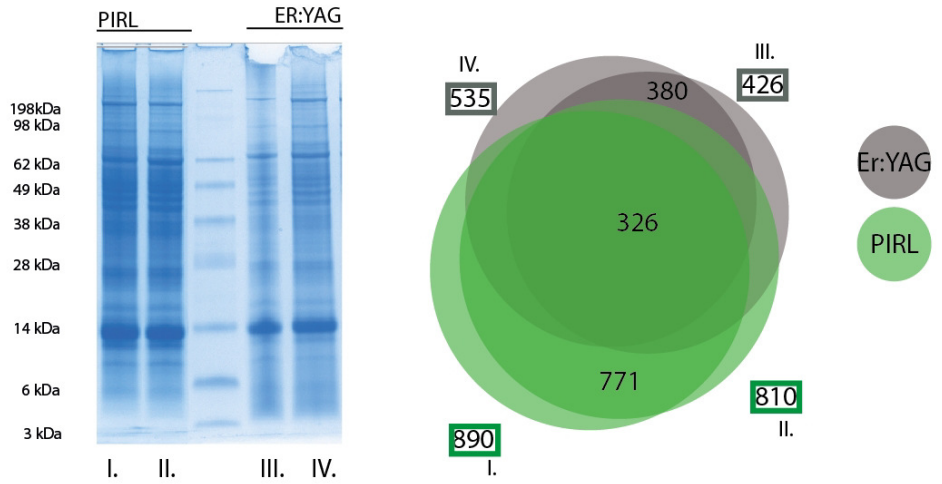

Figure 4.4. – SDS-PAGE and VENN-diagram of shotgun analysis of rat liver tissue with PIRL (green) and Er:YAG laser (grey) system. Two ablated PIRL samples with an average fluence of 1 J/cm^2 (I. and II.), a protein standard (PS), two Er:YAG laser samples with an average fluence of 40 J/cm^2 (III.) and 60 J/cm^2 (IV.) were used for both analytic methods. For both lasers, similar proteins were extracted and related SDS-PAGE band patterns were visible. In contrast to muscle tissue, no blurred area under 10 kDa for the Er:YAG laser samples were visible. The numbers of identified proteins in the PIRL samples were 890 (I.) and 810 (II.), in comparison to the Er:YAG laser samples with 426 (III.) and 535 (IV.) The overlap with regard to equal proteins within the PIRL and Er:YAG laser samples were 771 and 380, respectively. In all four samples 326 identical proteins were found.

In the first MALDI spectrum, already a second small peak for Ang 2-10 (m/z 1181.7.5) besides the initial Angiotensin I (Ang 1-10, m/z 1296.7) is visible. The spectra after 3h and 6h show similar signals and two additional peaks for Angiotensin II (Ang 1-8, m/z 1046.5) and Ang 1-7 (m/z 899.5). These signals are clear indications of at least three proteases with intact enzyme activity. In the last MALDI spectrum of the incubate after 24h, only an increase of the peak signals for the mentioned Angiotensin degradation products are visible and no further strong signals for additional angiotensin types were identified.

In contrast, the MALDI-TOF mass spectra of the incubate with the Er:YAG laser condensates are shown in figure 4.6 and only reveal a signal of Angiotensin I (Ang 1-10, m/z 1296.7). The degradation products of angiotensin as in the case of the PIRL ablation were not detected indicating an inactivity of the angiotensin peptide metabolizing enzymes.

As a negative control, the same concentration of Angiotensin I (Ang 1-10) was diluted in purified water (18.2 MΩ·cm) and MALDI-TOF spectra were recorded at 0h, 3h, 6h and 24h (Appendix B). The obtained spectra displayed intact Angiotensin I (Ang 1-10) at all time points and ensured that Angiotensin I (Ang 1-10) was not degraded by other environmental influences.

4.4. Discussion

This study investigated, to the best knowledge of the author for the first time, direct protein extraction from tissue via laser ablation with microsecond pulse durations. Typically, the microsecond regime is known for large coagulation zones in the adjacent tissue during the ablation process [41]. In direct comparison to PIRL, the large extent of damage in the remaining tissue is obvious by the naked eye. However, in a first qualitative analysis in form of a SDS-PAGE a similar weight range of proteins was extracted for both lasers and bands in the 200 kDa area were also visible for the Er:YAG laser. Since discrete instead of diffuse bands occurred in this area, it can be assumed that intact proteins were present. In a further study by Kwiatkowski *et al.* [114], the successful extraction of even larger proteins such as myosin-4 (Mr= 222.7 kDa) and the muscle-associated protein titin (Mr= 3.9 MDa) was shown for the PIRL ablation.

Within this study, the highest total number of identified proteins within two technical replicates was 929 proteins in liver tissue for the PIRL ablation. In a further study with human tonsils, a total number of up to 2085 identified proteins was extracted by PIRL within three biological replicates [65]. Since in this study only technical replicates and no biological replicates were used, the amount of 929 identified proteins is reasonable

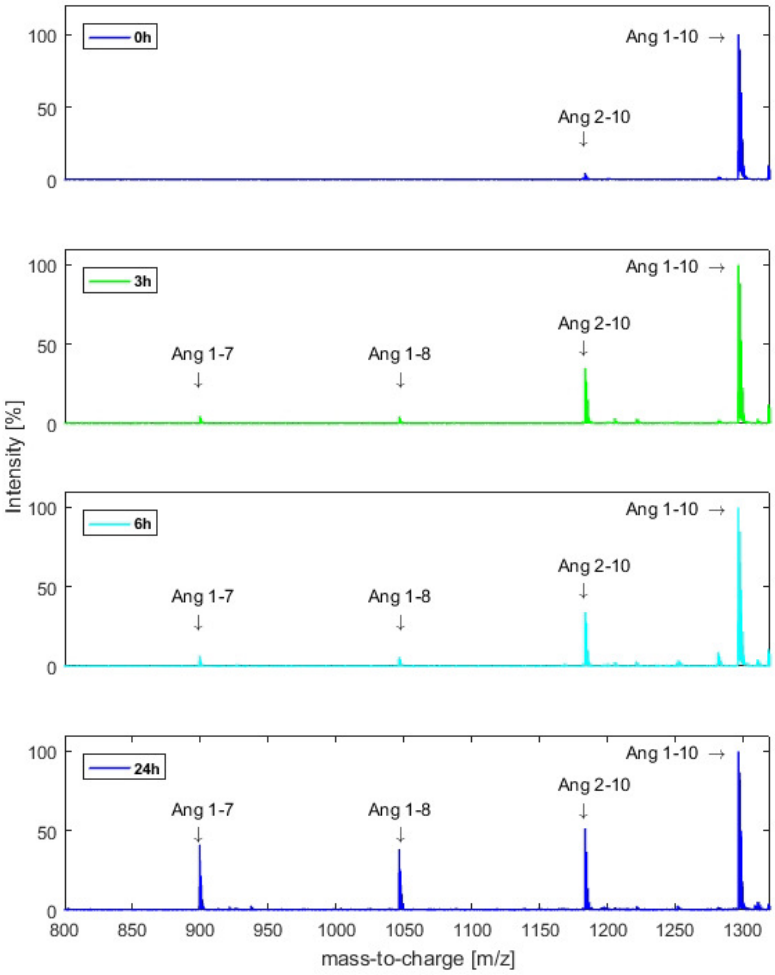

Figure 4.5. – MALDI-TOF mass spectra of angiotensin 1-10 (c=10^{-5}) incubated with ablated rat kidney after PIRL ablation. Reaction products were detected by MALDI-TOF MS after 0h, 3h, 6h, and 24h. All measured signals are labeled with an arrow and the associated angiotensin name. The detected signals clearly indicate an intact enzyme activity within the PIRL condensate.

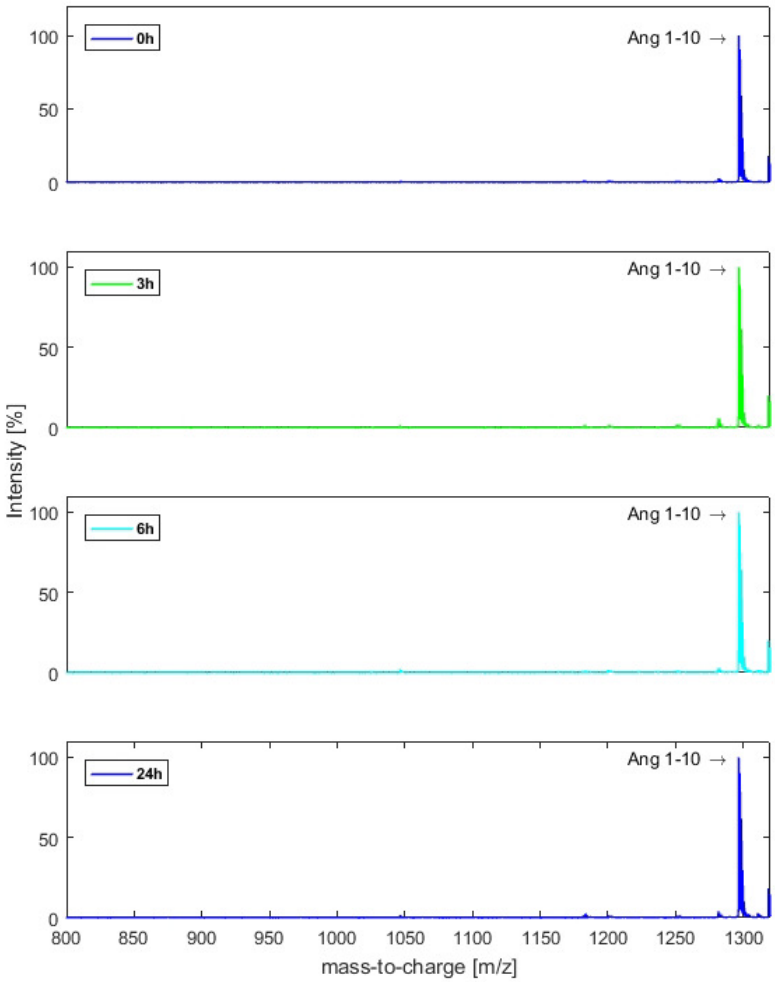

Figure 4.6. – MALDI-TOF mass spectra of angiotensin 1-10 (c=10^{-5}) incubated with ablated rat kidney after Er:YAG laser ablation. Reaction products were detected by MALDI-TOF MS after 0h, 3h, 6h, and 24h. Over time only the signal of angiotensin 1-10 is visible. This shows that the enzyme activity is not any longer intact.

in case of the PIRL ablation. The identified protein number in the condensate of the aerosol obtained by irradiation was higher in muscle with the Er:YAG laser and in liver with the PIRL. To identify a relation between the number of identified proteins and the different structure of the tissues for both lasers, additional analyses in further tissue types are necessary. In the shotgun method, the number of identifiable proteins within technical replicates varied by around one hundred proteins for both lasers in the two tissue types. To assess the reproducibility of the two laser homogenization methods, the share of equal identified proteins within two technical replicates was compared to the overall identified number of proteins in both samples for each laser. In case of PIRL, for muscle tissue a quota of 76 % was calculated and in liver tissue 83 %. For the Er:YAG laser, 89 % was determined in muscle tissue and 65 % in liver tissue.

The measured intact enzyme activity after PIRL ablation indicates an unaltered tertiary structure of the proteins in contrast to the Er:YAG laser ablation. Already Kwiatkowski *et al.* proved intact enzyme activity in the captured condensate after PIRL ablation [114]. Moreover, the comparison of a conventional mechanical homogenization method and the DIVE technique revealed less degraded protein species by proteolysis due to a different work flow in Kwiatkowski *et al.* [65]. In the PIRL application, the proteins were immediately frozen after ablation and proteolytic degradation was stopped without permanently damaging the enzyme activity as in contrast to the Er:YAG laser ablation. This unique feature of the applied PIRL homogenization method can enable analysis of new biological questions in pathologically identified regions by extracting intact functioning proteases by simultaneous temporarily arresting their enzyme activity. However, the author cannot exclude that the enzyme denaturation, as a consequence of the Er:YAG laser ablation, is also beneficial for certain metabolic research to obtain a time-depended snapshot without any later protein alterations due to intact proteases.

The extent of which the PIRL and Er:YAG laser homogenization influences post-transitional modifications (PTMs) such as phosphorylation or glycosylation relevant for cell signaling was not explicitly answered within this study. However, in earlier experiments, it was proven for the PIRL condensate that the tertiary structure with PTMs was maintained [65, 114].

The almost fragmentation-free transfer of complex biological molecules via laser ablation from tissue samples was already shown in numerous studies. In 1989, the biological material transfer from frozen aqueous solution via laser ablation with tens of nanoseconds pulse durations was successfully proven for double-stranded DNA molecules with up to 100 base pairs without fragmentation [122]. Moreover, the extraction of intact biological material with conserved function via PIRL was demonstrated with viruses

and yeast cells [38]. In addition, intact protein ferritin molecules with a large mass (approximately 440 kDa) were identified in the collected ablation plume on TEM images and sustained fluorescence was observable after the ablation of a fluorescent labeling protein called recombinant green fluorescence protein (rGFP). The latter clearly indicated an intact tertiary structure of the protein after PIRL ablation. Numerous further studies revealed for MALDI-MS analysis with nanosecond lasers, the almost fragmentation-free protein transfer out of tissue samples [113, 123]. However, in the previously mentioned studies the enzyme activity itself was not evaluated, because MALDI-MS spectra reveal only the masses of the proteins/peptides and provide no information on the tertiary structure of the proteins. In addition, the MALDI-MS analysis requires an acid MALDI matrix degrading enzymatic activity. Usually, MALDI ions are transported into vacuum, where enzymatic tests are extremely difficult to perform.

Since a time period of tens of nanoseconds was stated as a speed limit for thermal unfolding of large proteins, the maintained 3D- protein structure with intact enzyme activity after PIRL ablation can be explained due to the short laser pulse duration of the PIRL in the picosecond regime and the absence of thermal damage to the adjacent tissue. An additional explanation for the intact proteases can be the relatively low temperature rise within the ablation site due to adiabatic expansion. Further studies with nanosecond lasers for the fragmentation-free protein transfer would be interesting with regard to enzyme activity.

4.5. Conclusion

The protein extraction capabilities of two infrared lasers with different pulse durations using various analytical approaches were demonstrated in this study. For the first time, protein extraction for a microsecond infrared laser with a wavelength of 3 µm was tested and compared to a novel Picosecond Infrared Laser. Although a similar weight range of extracted proteins for both lasers in two different tissues was discovered, a clear difference in enzyme activity after ablation was found. In contrast to the microsecond Er:YAG laser, the homogenates after PIRL ablation still exhibited intact proteases. This imposingly reveals the softness of the PIRL-DIVE process compared to the other ablation process via Er:YAG laser, since the obtained enzyme activity clearly indicates an intact 3D-structure in terms of the tertiary structure of proteins.

5. New Applications of DIVE in Medicine

In previous experiments, the DIVE ablation process was successfully applied in different medical fields. As already mentioned in the introduction, the PIRL was compared to other cutting tools in wound healing studies, in laryngeal surgery, in a phonomicrosurgical application at vocal folds, in bone cutting and corneal incisional surgery. Two proof-of-principal experiments with PIRL are presented in this chapter to improve current laser applications for stapedotomy to treat otosclerosis in otorhinolaryngology and sclerostomy in glaucoma treatment in ophthalmology.

5.1. Stapedotomy with PIRL

This section is based on the accepted paper: H. Petersen[1], A. Gliese[1], Y. Stober, S. Maier, N.-O. Hansen, S. Kruber, D. Eggert, M. Tóth, T. Gosau, H. Schlüter, K. Püschel, U. Schumacher, R. J. D. Miller, A. Münscher, C. Dalchow, Picosecond Infrared Laser (PIRL) application in stapes surgery - first experience in human temporal bones, Otology & Neurotology, 2017.

The author of this thesis defined experimental parameters, together with H. Petersen performed the experiments, and contributed to the manuscript.

5.1.1. Introduction to Stapedotomy

In a healthy ear, the sound-waves passing the auditory canal are converted at the eardrum into vibrations. These vibrations are transmitted from the eardrum via the auditory ossicles to the inner ear. In figure 5.1, the anatomy of the ear is shown, including the middle ear with the auditory ossicles consisting of malleus, incus and stapes. Otosclerosis is a genetically caused middle ear disease and manifest itself in

[1] authors contributed equally.

an abnormal bone growth around the smallest bone within the auditory ossicles, the stapes bone. The stapes bone with its stirrup-shape is connected by its footplate to the oval window as a membrane-covered opening to the inner ear. An abnormal bone growth results in a fixation of the stapes bone preventing a free move of the auditory ossicles and the transmission of sound to the inner ear.

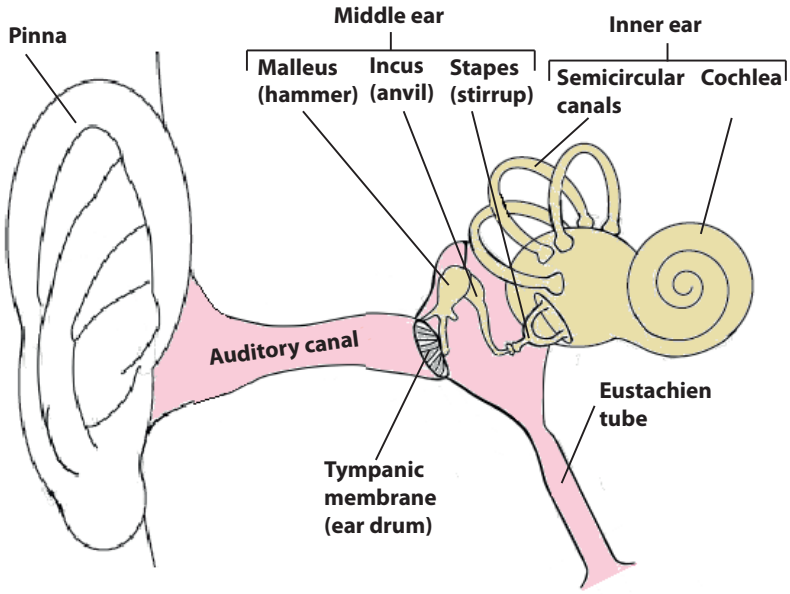

Figure 5.1. – The anatomy picture of ear shows the relevant parts for hearing in the outer, middle and inner ear. In the middle ear the auditory ossicles are located consisting of malleus, incus and stapes.

A surgical treatment for otosclerosis is stapedectomy to achieve improved hearing. The modern re-constructive stapes surgery as stapedectomy was firstly introduced by John J. Shea *et al.* in 1956 replacing the otosclerotic stapes bone by a Teflon prosthesis fixed to the incus [124]. Over time numerous improvements of the prosthesis were accomplished with regard to materials and design [125]. In case of stapedectomy, the stapes bone is completely or partly removed and replaced by a prosthesis.

Another improved surgery and new standard operative procedure for the treatment of otosclerosis is stapedotomy, where the anterior crus of the stapes bone is fractured and a perforation is made into the footplate to place a piston-shaped prosthesis. Compared to stapedectomy, the treated patients with stapedotomy showed less inner ear lesions with better hearing at high frequencies [126]. The perforation of the footplate, the so-

called fenestration, can be conducted via a mechanical perforator, a drill or laser. The first laser application was performed by Perkin *et al.* with an argon laser in 1978 [127]. The use of lasers is superior to conventional drills, since they increase the precision and can be used in a vibration-less, non-contact mode, lowering the risk of inner ear damage in consequence of footplate fracture or mobilization. The study of Perkins showed a lower risk of negative results, less postoperative balance disturbance and improved hearing in treated patients compared to conventional methods. As a consequence numerous other lasers were tested for stapedotomy such as CO_2 laser, Excimer laser, Ho:YAG laser, KTP laser, Er:YSGG laser, and Er:YAG laser [128–130]. One of the most successful ones are up to date the Er:YAG laser, KTP laser, and argon laser. The application of current lasers theoretically risks inner ear damage due to thermal effects, acoustic effects, and pressure waves [125, 128, 131–133]. However, recent studies exist with good postoperative results without signs of relevant inner ear damage [134, 135]. On the basis of the gentle ablation without thermal and acoustic damage, PIRL has great potential for stapedotomy.

5.1.2. Materials and Methods

On nine human stapes, footplate perforations were performed with the PIRL and an Er:YAG laser to study the feasibility and compare the results in terms of microscopic and histological quality.

Laser Systems and Fibres

A prototype Picosecond Infrared Laser (PIRL -HP3-1064 OPA -3000, Attodyne Inc., Toronto, Canada) was used for the experiments. As mentioned before, the pulse width was around 400 ps and Gaussian shaped laser pulses were emitted with a wavelength of 3000 ± 90 nm and a repetition rate of 1 kHz.

The used commercial Er:YAG laser (MEY-1-A EX-2, J Morita Mfg Corp., Kyoto, Japan) had in comparison with PIRL a longer pulse width of 300 µs, a slightly shorter wavelength of 2.94 µm, and a lower pulse frequency of 1 Hz, but also emitted a Gaussian shaped beam.

Both laser outputs were coupled into optical fibres. For the PIRL a sapphire multi-mode fibre (Photran, LLC, Poway, California) was used with a core diameter of 250 µm and a length of approximately 1 m. Before the experiment, the sapphire fibres were polished with diamond polishing films with a grid size of 1 µm. The average laser output after the fibre for the stapes perforation was measured with an energy meter (Energy Max Sensor J-25MB-LE, Coherent, Santa Clara, California, USA) for 60 seconds and was roughly 0.330 mJ. The resulting average fluence was around 0.7 J/cm^2

and was in a similar range compared to first bone ablation with PIRL using an average fluence of 0.88 J/cm^2 in Jowett *et al.* [45]. The Er:YAG laser output was coupled into a commercial hand piece with a 600 µm glass fibre tip at the end (C600F, J Morita Corp., Kyoto, Japan). The fibre output of the Er:YAG laser was chosen after a literature research to be equivalent to typical average fluences in laser stapedotomy with an Er:YAG laser. Hence, the experiment for the Er:YAG laser was divided in two groups with pulse energies of 30 mJ and 60 mJ, corresponding to an average fluence of 10 J/cm^2 and 22 J/cm^2, respectively. For the Er:YAG laser a different energy meter(Energy Max Sensor J-50MB-IR, Coherent, Santa Clara, California, USA) was used.

Surgical Procedure

The nine human cadaver footplates were stored before the experiment within their surrounding anatomic structures in 4 % formalin. They were prepared before the experiment to easily access the footplate with the fibres. The whole study was divided into three groups: a PIRL group, and two Er:YAG laser groups with the mentioned pulse energies of 30 mJ and 60 mJ. In each group, three stapes perforations were performed and the laser application was controlled via a shutter to exactly determine the applied number of laser pulses. The laser fibre was first put in contact with the stapes footplate, before the shutter was opened. The shutter time was set to 1 sec and after every second the perforation process was controlled by naked eye using magnifying glasses. As soon as a perforation diameter equivalent to the fibre diameter was reached or no improvement in the perforation size was observable, the ablation was stopped. For every tissue sample the exact time with corresponding laser pulses was documented.

Analysis of Tissue Effects

After ablation, the stapes bones were isolated and stored in 10 % phosphate buffered saline. The stapes fenestrations were in a first step imaged with an Environmental Scanning Electron Microscope (Phillips XL30, Fei, Hilsboro, Oregon, USA) in two different magnifications (100x and 800x). The gaseous secondary detector of the ESEM was operated at a pressure of 1.5 Torr, a spot size of 5 (software setting), and a beam potential of 20 kV. By means of the ESEM, the size and shape of the perforation as well as the structure of the tissue after ablation were investigated. In a second step, a histological investigation was conducted to determine the thermal damage and the integrity of tissue on the cellular level. Therefore, the tissue samples were decalcified for 24 hours in 10 % ethylenediaminetetraacetic acid (EDTA) and consecutively in 70 % propanol for 12 hours. Afterwards the tissue samples were embedded in paraffin, cut in sections, stained with hematoxylin and eosin (H.E.) and studied with a light microscope (Zeiss Axio Plan 2 Microscope System, Oberkochen, Germany).

5.1.3. Results

Both the sapphire fibre and the glass fibre could be easily placed on the stapes footplate. An overview of the applied laser parameters in the different experimental groups for PIRL and Er:YAG laser is shown in table 5.1.

Laser	**Pulse Energy** (mJ)	**Frequency** (Hz)	**Amount of Pulses**	**Fluence** (J/cm^2)	**Total Energy** (mJ)
PIRL- 250 μm sapphire fibre	0.323	1000	2000	0.7	646
	0.357	1000	3000	0.7	1071
	0.309	1000	3000	0.6	927
Er:YAG- 600 μm glass fibre	30	1	20	10	600
	30	1	15	10	450
	30	1	15	10	450
Er:YAG- 600 μm glass fibre	60	1	3	22	195
	60	1	3	22	195
	60	1	4	22	260

Table 5.1. – Laser settings on the sample surface during ablation experiments.

In case of the PIRL group, 2 sec or 3 sec were necessary to perforate the stapes footplates corresponding to 2000 or 3000 laser pulses. Hence, the total needed energies were in the range of 636 mJ to 1071 mJ. In the Er:YAG laser group with pulse energies of 30 mJ, an amount of 15 to 20 laser pulses were needed for footplate fenestration resulting in a total applied energy between 450 mJ and 600 mJ. Compared to the Er:YAG laser group with 30 mJ, the Er:YAG laser ablation with 60 mJ required 3 and 4 laser pulses for perforation. This is a significantly lower number and also the needed total energy was considerable smaller. Overall, it is deducible that with lower pulse energies the necessary total energy for the stapes perforation was increased.

Tissue Effects after Footplate Fenestration with PIRL

On the ESEM images displayed in figure 5.2, the PIRL perforations revealed a relative round shape with precise edges and the perforation diameter for the three tissue samples were measured to be 330 µm, 330 µm and 200 µm. Severe bone damages or bigger cracks were not observable at the surrounding bone tissue. Of particular interest is the cutting edge surface, since it showed an intact micro-structure with undamaged bone fibres. This clearly demonstrates the gentle ablation by PIRL without signs of coagulation or tissue disruption. In addition, the HE-stained tissue samples showed no evidence of thermal damage in form of carbonization. Besides, the cut surface

displayed an angled edge and the perforation diameter increased in size in direction of the inner ear. An explanation for this fact can be the exit angle of the fibre output resulting in a growing light cone with increasing distance of the fibre end.

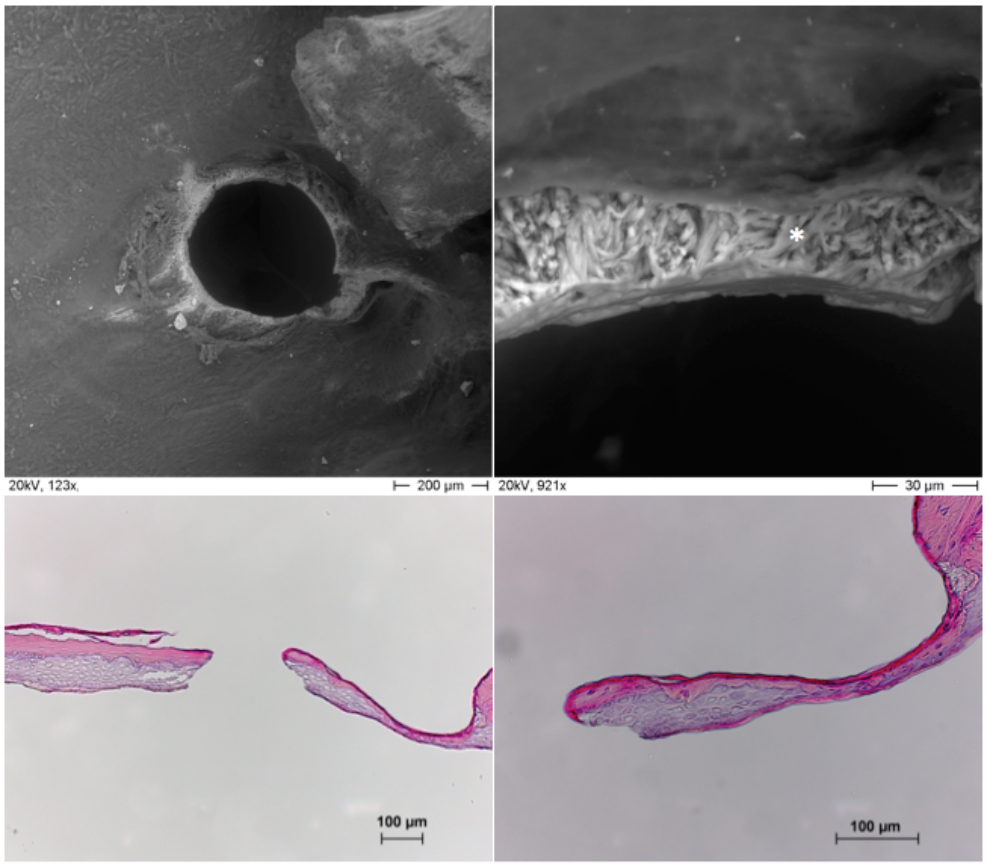

Figure 5.2. – Tissue effects after fenestration with PIRL. The ESEM images showed a round shape with precise edges for the PIRL perforation at a 123-fold magnification. At the cutting surface intact bone fibres (*) were visible. HE-staining indicated no evidence of thermal damage.

Tissue Effects after Footplate Fenestration with Er:YAG laser at 30 mJ

The ESEM and histological pictures of the Er:YAG laser stapes fenestration with a pulse energy of 30 mJ are displayed in figure 5.3. The Er:YAG laser perforation under ESEM showed an ablation zone considerably bigger than the ablated hole within the

stapes footplate.

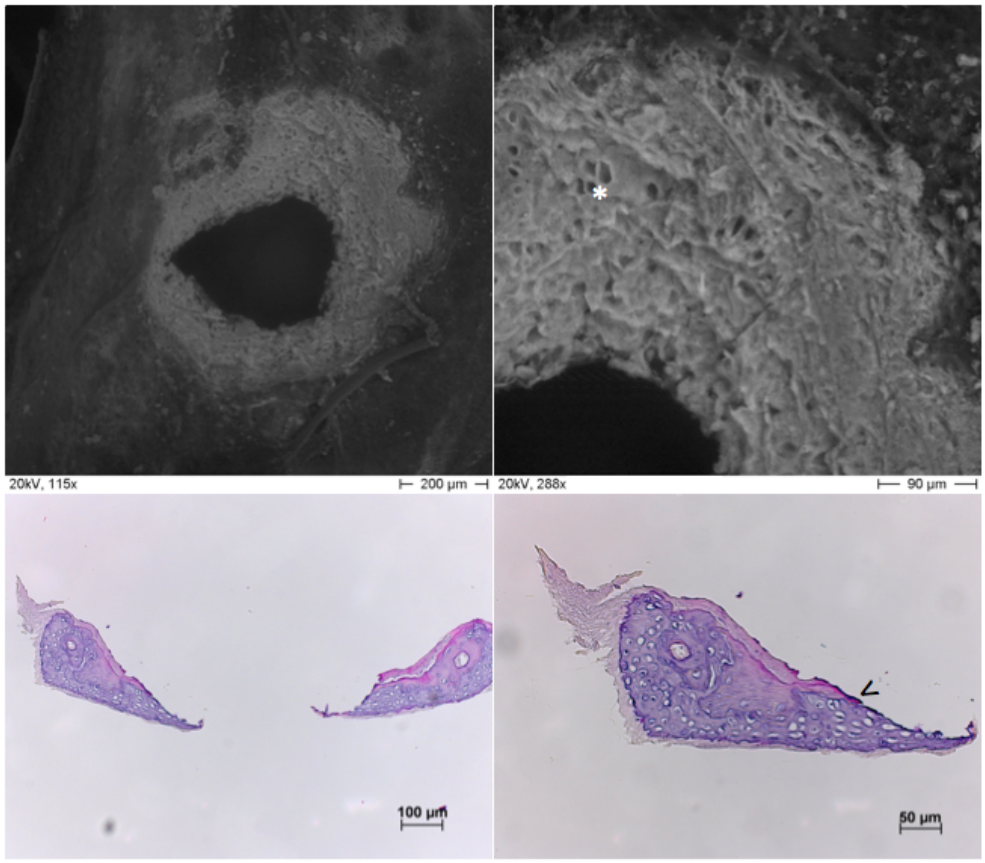

Figure 5.3. – Tissue effects after fenestration with Er:YAG laser at pulse energies of 30 mJ. ESEM pictures revealed an ablation zone considerably bigger than the ablated hole within the stapes footplate. Moreover, the perforation was not uniformly round shaped and the cutting surface showed an amorphous structure. However, intact canals within the bone were visible (*). The HE-stained tissue samples showed minimal thermal damage in terms of carbonization (<).

The measured perforation diameters for the three bone samples were 450 µm, 260 µm and 450 µm in contrast to the ablation zones with diameters of 890 µm, 610 µm and 680 µm. Furthermore, the perforations were not as close to uniform circular shapes as in case of footplate perforations conducted by PIRL. When the cutting surface of the Er:YAG laser ablation is compared to the PIRL ablation, instead of

intact bone fibres an amorphous surface was recognizable. The perforation margins in the histological investigations with HE-staining were smooth and thermal damage in terms of carbonization was only minimal apparent. The cutting edges showed an angel and the thickness of the footplate decreased towards the center hole like it did after perforation by using PIRL.

Tissue Effects after Footplate Fenestration with Er:YAG laser at 60 mJ

Under the ESEM, the Er:YAG laser perforations with pulse energies of 60 mJ showed a reasonable round form, but the perforation margins were uneven (Figure 5.4).

Bursted edges at the margins were clearly visible as well as cracks in the lateral damage zone. However, the ablation zone was not significantly larger than the ablated hole. The cut surface showed also no intact bone fibres as before after footplate perforation with the Er:YAG laser at 30 mJ. The histological images indicated carbonization in the dark areas at the cut surface.

5.1.4. Discussion

Over the last decades, the laser-based stapes surgery has been tested with several different lasers in numerous *ex-vivo* and *in-vivo* studies. In principle, the ideal laser for stapes surgery avoids to adversely affect the inner ear function and creates a highly precise perforation in a short application time. The inner ear function can be injured by laser applications in a number of ways. One possibility is the deep penetration of laser light inside the cochlea due to its low absorption coefficient of the containing fluid in case of visible lasers such as argon or KTP lasers [136]. Secondly, lasers with long pulse durations such as typical CO_2 lasers can indirectly harm the inner ear structures due to heat generation during bone ablation. One of the most serious complications in laser stapedotomy is the hearing loss caused by the inner cochlear fluid becoming overheated and damaging the hair cells [137]. A third damage mechanism is the acoustic shock wave formation during the stapes perforation, which can also harm the inner ear structures.

The Er:YAG laser is an efficient tool in stapes surgery, because of its minimal thermal effects to adjacent tissue [131, 133, 138, 139]. However, in several studies the produced acoustic shockwaves by Er:YAG lasers were associated with impaired inner ear function [130, 132, 140]. In literature, both the influence of single pulse energy and the total applied energy were evaluated regarding signs of inner ear damage such as persistent tinnitus, transient dizziness, and deterioration of bone conduction.

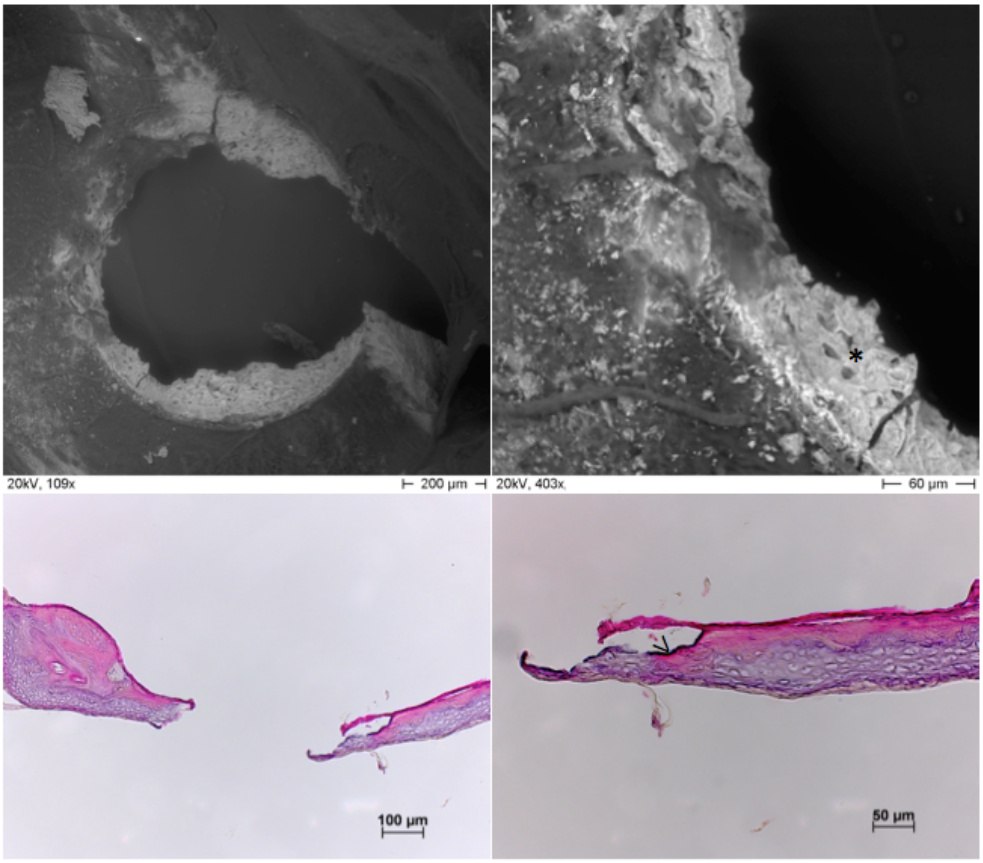

Figure 5.4. – Tissue effects after fenestration with Er:YAG laser at pulse energies of 60 mJ. ESEM images revealed for the footplate perforations an almost round form, but the perforation margins were irregular and bursted edges were visible. At the cut surface, intact bone fibres were not observable. Intact bone canals were occasionally visible (*). By means of HE-staining thermal damage was detected at the cut surface (>).

The chosen pulse energies of 30 mJ and 60 mJ for the Er:YAG laser in this study represent recommended pulse energies in other studies and are also comparable to applied fluences in clinical use. The pulse energies used for stapedotomy with the Er:YAG laser ranged from 10 mJ to 450 mJ [132, 137, 141], however the upper limit for preventing inner ear damage varies in literature. In Arnoldner *et al.* [142] each pulse should be restricted to a pulse energy of 15 mJ to avoid the formation of high pressure

waves damaging the cochlea. For an acceptable total amount of energy, Parilla *et al.* [140] stated 500 mJ, since patients with higher applied total energies postoperatively complained about persistent tinnitus. In a further study, Syfter *et al.* [137] proposed that a single laser pulse should not exceed a pulse energy of 35 mJ and the total applied energy should be limited to 400 mJ. Häusler *et al.* [132] introduced a fluence in the range of 10 to 17 J/cm^2 producing pressure waves between 140 dB and 160 dB as a limit for clinical applications. In Lippert *et al.* [139], a pulse energy of 60 mJ was recommended for an optimal footplate perforation, however this was the lowest pulse energy tested within this human clinical trial.

Both in the Er:YAG laser experimental group at 30 mJ and the PIRL experimental group, the total energy amount needed for an acceptable perforation size exceeded a limit of 400 mJ. Moreover, the footplate perforation in case of the Er:YAG laser group at pulse energies of 30 mJ recommended in literature showed an incomplete perforation under the electron microscope. The perforation diameters in the range of 260 µm and 450 µm were considerable smaller than the 600 µm diameter of the glass fibre. The ablation pattern with damaged tissue in the edge region indicates that the beam profile of the fibre output had not a perfectly flat top shape and a higher beam intensity existed in the center. In comparison, the stapedotomies with the Er:YAG laser at 60 mJ revealed almost completely round footplate perforations with acceptable sizes in the range of 480 µm and 650 µm. In addition, the applied total energy remained under the acceptable limit of 400 mJ. Nevertheless, the electron microscope images exposed bursted edges and cracks in the lateral zone. For these reasons, the recommended pulse energy of 30 mJ could not be fully confirmed for avoiding inner ear damage due to the higher needed total energy. However, also footplate perforations at a pulse energy of 60 mJ exposed clear signs of lateral injury and were stated in literature to cause hearing impairment, if only a single laser pulse was applied.

In spite of the similar wavelength, the PIRL possess different ablation dynamics due to its shorter pulse durations compared to the Er:YAG laser. Therefore, the total energy limit of 400 mJ is not applicable for the PIRL, since the laser pulse duration is shorter than the acoustic relaxation time and stress confinement occurs within the irradiated tissue. This means that the total energy deposited by PIRL is used to ablate the tissue. Moreover, the arising GHz acoustic transients are strongly attenuated in tissue within a few micrometers [13]. The gentle and precise ablation of PIRL was shown in this study by round shaped perforations with clear margins and intact bone fibres. The application time for the PIRL stapedotomy was very quick and lasted only a few seconds. The only current disadvantage of the PIRL was the limited fibre diameter of 250 µm and the resulting fenestration size of 330 µm. Normally, the shaft of the stapes prosthesis is around 400 µm. Sapphire fibres with a bigger diameter up to 500 µm are available, however higher pulse energies are necessary to achieve similar fluences in the

range between 0.5 J/cm^2 and 1 J/cm^2 like in this study. A new PIRL laser design aims to reach the required pulse energies of 1 to 2 mJ by directly amplifying the 3 µm laser radiation instead of the current OPA system.

5.1.5. Conclusion

For the first time the PIRL was used in the perforation of the footplate in stapes surgery on human cadaver tissue and the outcomes were compared to a conventional Er:YAG laser. The recommended pulse energy of 30 mJ for the stapedotomy with an Er:YAG laser delivered only insufficient footplate perforations in size. Stapedotomies with a higher pulse energy of 60 mJ with the Er:YAG laser reached an acceptable perforation size, but caused bursted edges and cracks in the lateral zone of the perforation. In comparison with the stapedotomies conducted by the Er:YAG laser, the footplate perforations realized by PIRL showed superior results regarding precision and thermal damage in electron microscopy and histological examinations. In addition, the PIRL enabled a gentle, ultrafast ablation with almost completely confinement of the deposited energy in the ablation site leading to strongly reduced shockwave effects. This characteristic of the PIRL laser could potentially contribute to overcome the previous problems found in literature with laser stapedotomy resulting in inner ear damage. Further studies are necessary to evaluate the improved non-traumatic ablation of PIRL with a view of inner ear structures.

5.2. Picosecond Infrared Laser - Fibre-Assisted-Sclerostomy (PIRL-FAST): A Proof of Principle Analysis

The following section is based on the submitted paper: J. Mehlan, S. Maier, N.-O. Hansen, T. Gosau, D. Eggert, M. Spitzer, H. Petersen, S. J. Linke, and R. J. D. Miller, Pikosekundenlaser- Faser-assistierte Sklerostomie (PIRL- FAST): Ein erster Machbarkeitsnachweis, Der Ophthalmologe, 2017

The author defined the experimental laser parameters, performed all experiments together with J. Mehlan, and contributed to the manuscript.

5.2.1. Introduction to Sclerostomy

The term glaucoma describes a group of eye diseases leading to a loss of vision caused by damage to the optical nerve. Glaucoma is worldwide the most frequent cause of blindness [143]. In most cases, an increased pressure inside the eye, namely intraocular hypertension, is responsible for the optical nerve injury [144]. As cut-off point for the intraocular pressure (IOP) to diagnose glaucoma, a value of 21 mmHg is used in Western population [145]. So far, the intraocular pressure (IOP) is the only modifiable parameter to influence the disease [146]. Other forms of glaucoma with normal or decreased IOP do exist however.

The eye consists of different chambers filled with fluids (see figure 5.5). In the posterior chamber between iris and lens, an aqueous fluid, the so- called aqueous humour, is produced in the ciliary epithelium. Two different physiological outflow drainage systems exist for this chamber water [147, 148]. First, the fluid can leave the eye in the anterior chamber via the dominating drainage route comprising of the trabecular meshwork, the Schlemm's canal and the intra- and episcleral veins. A second physiological outflow path is the uveoscleral route via the vessels of the ciliary body, the iris, and the choroid.

The increased pressure inside the eye is typically caused by a blockage of the described drainage systems. In glaucoma with intraocular hypertension, a distinction is made between different forms, also referred to the open angle glaucoma or closed angle glaucoma. The most common form is open angle glaucoma, a blockage of the trabecular meshwork and the Schlemm's canal [149]. In the other form, the blockage results from the iris being pressed on the trabecular meshwork [150].

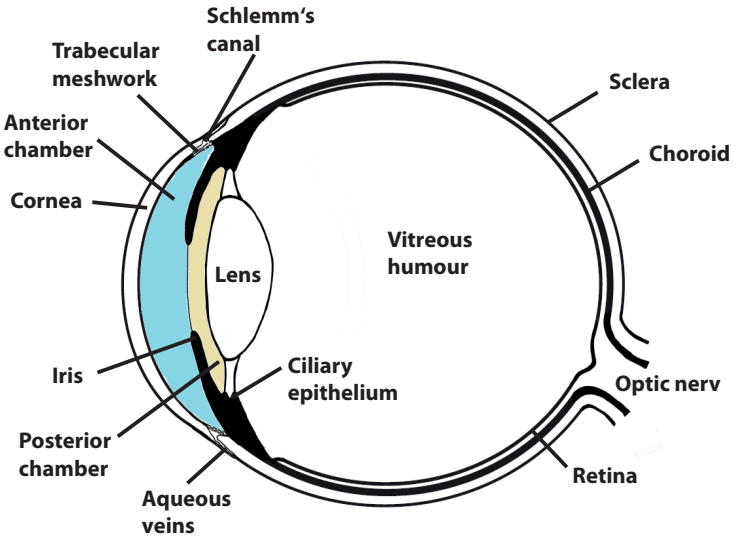

Figure 5.5. – The anatomy of eye illustrates the parts and chambers relevant for glaucoma. In the ciliary epithelium located in the posterior chamber, an aqueous fluid is produced and drained off via the trabecular meshwork, the Schlemm's canal and the aqueous veins.

Therapeutic procedures for glaucoma caused by intraocular hypertension are medications or surgical treatments. To initiate a treatment, patients are usually given pressure-lowering eye drops to reduce for example the production of aqueous humour. In surgical treatments, the trabecular meshwork can be reopened in a trabeculectomy or the iris is perforated to facilitate the outflow of the aqueous humour. Recent developments in terms of pressure-lowering eye surgery point towards minimally invasive procedures with the aim to attain a maximum IOP-reducing effect with little collateral damage [146]. One of those modern methods is sclerostomy, where an opening is created into the sclera to reduce the intraocular pressure. Two categories for the procedure to perforate the sclera exist: *ab interno* from inside the eye towards the sclera surface and in the opposite direction, *ab externo*, from the sclera surface into the anterior chamber.

Lasers increasingly gain importance in glaucoma surgery, especially in incisional operations such as sclerostomy for patients with chronic forms of glaucoma. Laser sclerostomy is less invasive than standard Glaucoma incisional operations, where openings or fistula are created in the transition zone between cornea and sclera [151]. However, all sclerostomy procedures and conventional techniques face a common problem: the

success rates are reduced due to cell proliferation and scar formation in the opening [152]. A truly permanent outflow channel for the aqueous humour and a balanced pressure relation in the treated eye cannot be maintained.

In 1985, March and Gherezghiher performed the first laser sclerostomy in primate species applying a nanosecond Nd:YAG laser. The established perforation stayed open over a period of six months [153, 154]. In the same year, the authors additionally performed a first proof-of-concept laser experiment with a Nd:YAG laser on one living human eye [155]. Since then, numerous lasers such as Nd:YAG laser, Holmium laser, Excimer laser, and Er:YAG laser have been used for sclerostomies and tested with regard to collateral damage [155–159]. A central goal in some of these studies was to lower thermal effects and collateral damage to the adjacent tissue. By reducing these effects, surgical complications such as subconjunctival scarring and filtration failure could be theoretically minimized and the success rate enhanced [156, 159]. For this reason, the DIVE process is a promising mechanism for sclerostomy, since the PIRL cuts very precise and theoretically avoids laser-damaging effects such as thermal effects and shock wave propagation.

5.2.2. Materials and Methods

The sclerostomies were conducted as full-thickness sclera perforations in fresh enucleated porcine eyes with the PIRL. The aim was to evaluate the practicability of the Picosecond Infrared Laser-Fibre-Assisted Sclerostomy (PIRL-FAST) with regard to the area of the created opening into the sclera and the resulting collateral damage zone. However, the optimal perforation size with PIRL necessary for long-term drainage must be later evaluated in further *in vivo* studies.

Laser System and Fibre

As at section 5.1, a PIRL -HP3-1064 OPA -3000 (Attodyne Inc., Toronto, Canada) was used for the experiments. The PIRL output was coupled into a single-crystal unclad sapphire multimode fibre (MicroMaterilas Inc., Tampa, Florida, USA) with a 200 µm fibre core diameter and a length of approximately 1 m. By polishing the end faces of the sapphire fibres with diamond polishing films with a grid size of 1 µm, the fibres were prepared for the experiment. The average fibre output was measured by an energy meter (LabMax-Top with Energymax Sensor J-25-MB-LE, Coherent, Santa Clara, USA) over 60.000 laser pulses before every perforation with the sapphire fibre. During the experiment the average output power ranged from 150 µJ to 250 µJ and was adjusted via the electrical current for the diodes within the Nd:YAG laser.

Sample Preparation and Analysis

Fresh enucleated porcine eyes from a local slaughterhouse were used for the experiment. The harvested porcine eyes were cooled at 4°C until the operation at the same day. Shortly before the surgical procedure, the eyes were positioned in a special mount to hold the eyes in place for the perforation. Immediately after the sclerostomy, the eye samples were preserved and stored in 3.5 % phosphate buffered formaldehyde. In the course of the histological examination, the samples were cut in 4 µm thick slices and stained with hematoxylin and eosin (H.E., Merck, Darmstadt, Germany). Every tenth slice was placed on a glass slide and analyzed histologically. The produced specimens were scanned and digitized with a MIRAX SCAN device (Carl Zeiss Microimaging GmbH, Jena, Germany). All measurements and analyses of the histological specimens were performed with the CaseViewer software (3DHISTECH, Budapest, Hungary). For each prepared histological slice on a slide, the mean diameters of the perforations were determined, as well as the area of the created sclerostomy, and the collateral damage zone. In addition, an image of the PIRL-FAST was captured with an Environmental Scanning Microscope (XL30 FEI, Hillsboro, Oregon, USA), equipped with a solid state backscattered electron (BSE) detector and a gaseous secondary electron (GSE) detector at a water vapor pressure of 1.5 Torr, spot size of 5 (software setting), and an acceleration voltage of 20 kV. The DISS5 digital image scanning system (Point Electronic, Halle, Germany) was used for image acquisition. For preparation, the samples were fixed with 4 % paraformaldehyde in PBS and sectioned using a vibratome. The tissue slices were contrasted by incubation in 1 % OsO_4 in PBS for 60 min and then washed thoroughly in ddH_2O to remove excess OsO_4. The samples were placed on a 35 mm Petri dish that was filled with 2 % agar in ddH_2O. The agar prevents the dehydration of the sample during imaging.

5.2.3. Results

The sapphire fibre was easy to use with sufficient flexibility and length for the perforations. In total, PIRL-FAST was performed on 23 porcine eyes and hereinafter evaluated. The laser sclerostomies were conducted *ab externo* to avoid intraocular instrumentation and minimize conjunctival trauma.

The total number of samples was split into four groups, in which the procedures were conducted with the same pulse energy setting. As pulse energies 150 µJ (N=4), 175 µJ (N=6), 200 µJ (N=7), and 250 µJ (N=6) were chosen. For a fibre with a diameter of 200 µm these pulse energies correspond in contact-mode to average fluences of 0.48 J/cm^2, 0.56 J/cm^2, 0.64 J/cm^2, and 0.8 J/cm^2, respectively. All groups were separately analyzed to quantify and compare the obtained diameters and collateral

damage areas. Within the scope of this first feasibility study, ten successive histological slides of the created sclerostomies were evaluated over a total distance of 400 µm (see figure 5.6). Since the sclera in porcine eyes measures around 800 µm, the analyzed distance corresponds to half of the sclera thickness.

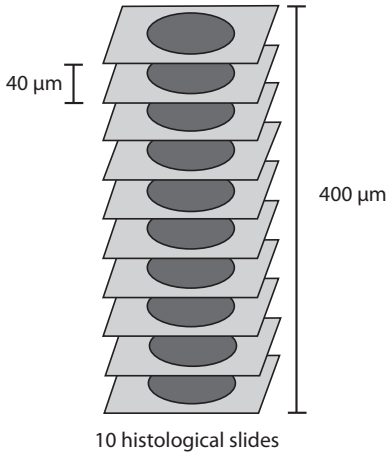

Figure 5.6. – Sketch of the geometries and distances between the histological slides. The perforation by PIRL-FAST is indicated by the grey cycles. Overall, ten histological slides with an interval of 40 µm were analyzed for each created PIRL-FAST. This corresponds to an entire length of 400 µm for each analyzed sclerostomy.

The created diameters and perforation areas of PIRL-FAST with associated standard deviations are shown in table 5.2 for the individual experimental groups. However, the measured values from histological sections give only an estimate of the produced hole size, since the samples are modified in size as well as shape during the histological processing [76].

For the different pulse energies, the mean diameters ranged from around 250 µm to 320 µm and the created areas from 19600 μm^2 to 28400 μm^2. In addition to the standard deviation, the p-value was calculated to test if the results show a significant difference between the experimental groups. The p-value indicates the probability with which a result is achieved by coincidence as good as in the conducted experiment. Typically, the significance level is set to 5 % for the p-value. If the p-value is smaller than this level, the result of the respective study is considered as significant.

Experimental group	**Pulse energy [µJ]**	**Mean Diameter of PIRL-FAST [µm]**	**Area of PIRL-FAST [µm^2]**
1	150	270 ± 90	19600 ± 5000
2	175	260 ± 60	23900 ± 6000
3	200	250 ± 60	22700 ± 7000
4	250	320 ± 90	28400 ± 8000

Table 5.2. – Diameters and areas of PIRL-FAST with the associated standard deviations for the experimental groups with the different pulse energies.

In table 5.3, the p-values of the comparison between the four experimental groups are listed.

	p-value Group 1 vs. Group 2	**p-value Group 1 vs. Group 3**	**p-value Group 1 vs. Group 4**	**p-value Group 2 vs. Group 3**	**p-value Group 2 vs. Group 4**	**p-value Group 3 vs. Group 4**
Area of PIRL-FAST	0.002	0.128	<0.001	1.000	0.021	0.001

Table 5.3. – P-values for comparison of the created PIRL-FAST areas between the various experimental groups. All p-values in comparison with group 4 were under $p< 0.05$. This showed a significant difference in size for the created areas of PIRL-FAST for this group. For all other groups no significant difference was obvious.

Since all p-values in comparison with group 4 at a pulse energy of 250 µJ were under $p<0.05$, this group showed with a significant difference the biggest area in comparison with all other groups. The distinction between group 2 and 3 with a p-value of 1 was not significant. Since the p-value for the comparison of group 1 and 3 was also $p>0.05$, no significant difference for all other groups was found.

In figure 5.7, representative histological images stained with H.E. of PIRL-FAST are presented for an applied pulse energy of 175 µJ and 150 µJ, respectively. The pink stained tissue in the histological images represents cellular tissue in sclera and the violet dots represent the cell nuclei. The perforation with PIRL at a pulse energy of 175 µJ was relatively circular and almost no collateral damage area was visible in terms of dark discoloration. The histological image of PIRL-FAST at a pulse energy of 150 µJ revealed signs of thermal damage and altered adjacent tissue.

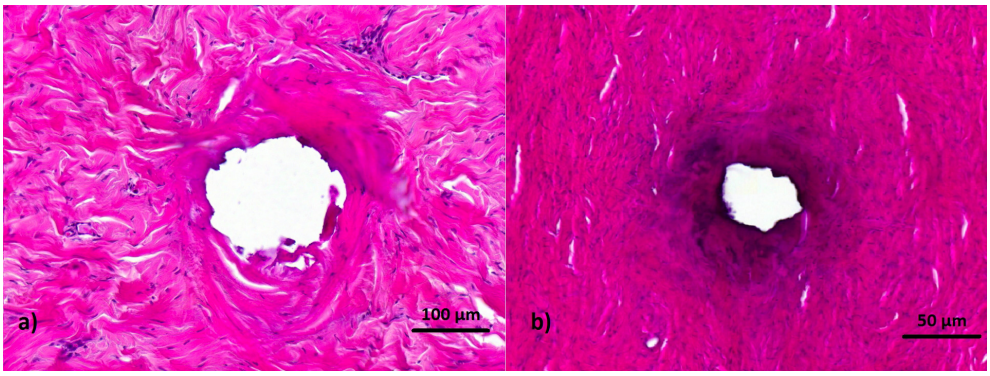

Figure 5.7. – Histological images of a PIRL-FAST created with a pulse energy of 175 µJ (a) at a 20-fold magnification and a pulse energy of 150 µJ (b) at a magnification of 10x. The dark discoloration in (b) indicates thermal damage and altered tissue.

For a systematical evaluation of PIRL-FAST, all areas in the histological images, which exhibit a destroyed cell structure with an insufficient differentiation or burn injuries were classified as collateral damage. As described before in figure 5.6, ten slides were analyzed over a distance of 400 µm in every sclerostomy. In every histological slide, the minimal and maximal thermal damage distance from the edge of perforation into the surrounding tissue was determined. In each case, a mean value with standard deviation was calculated of all minimal values and a separate one for all maximal values within an experimental group. From these two mean values, an average thermal damage distance was determined for each experimental group. An overview of the identified thermal damage distances is presented in table 5.4. Additionally, the area of collateral damage was calculated by marking the relevant areas of collateral damage in the CaseViewer software.

The minimal mean thermal damage distance within all conducted PIRL-FAST extended from 9±5 µm to 11±9 µm, and for the maximal mean thermal damage distance from 69±23 µm to 94±39 µm. The average thermal damage distance ranged from 38 µm to 53 µm. To further analyze the results, p-values were calculated to compare the differences between the areas of collateral damage in the four experimental groups (see table 5.5).

Sclerostomies created with a pulse energy of 250 µJ possessed a significant larger collateral damage zone compared to the other experimental groups, since all p-values in comparison with group 4 were under $p<0.05$. This result indicates a correlation between size of collateral damage and applied pulse energies.

Pulse energy [µJ]	**Mean minimal thermal damage distance [µm]**	**Mean maximal thermal damage distance [µm]**	**Average thermal damage distance [µm]**	**Area of collateral damage [µm^2]**
150	9 ± 5	72 ± 24	41	16448 ± 9978
175	6 ± 4	69 ± 23	38	15602 ± 12745
200	9 ± 7	80 ± 22	45	20225 ± 15983
250	11 ± 9	94 ± 39	53	31136 ± 14496

Table 5.4. – Extent of collateral damage for PIRL-FAST in dependency of the applied pulse energies. For each experimental group, a mean value with standard deviation was calculated of all minimal values and a separate one for all maximal values. From both values, an average thermal damage distance was determined. In addition, the area of the collateral damage was calculated with associated standard deviation.

	p-value Group 1 vs. Group 2	**p-value Group 1 vs. Group 3**	**p-value Group 1 vs. Group 4**	**p-value Group 2 vs. Group 3**	**p-value Group 2 vs. Group 4**	**p-value Group 3 vs. Group 4**
Area of collateral damage	1.000	1.000	<0.001	0.403	<0.001	<0.001

Table 5.5. – P-values for comparison of the areas of collateral damage created by PIRL-FAST between the various experimental groups. Only in comparison with group 4, all p-values were under $p<0.05$ and a significantly larger thermal damage was found.

To investigate the alteration of the surface structure of the perforated sclera, a single ESEM image was created. The ESEM image of PIRL-FAST conducted with a pulse energy of 175 µJ in figure 5.8 revealed intact collagen fibres and only minimal tissue changes in the edge region in form of amorphous surfaces demonstrating the gentle ablation of PIRL-FAST.

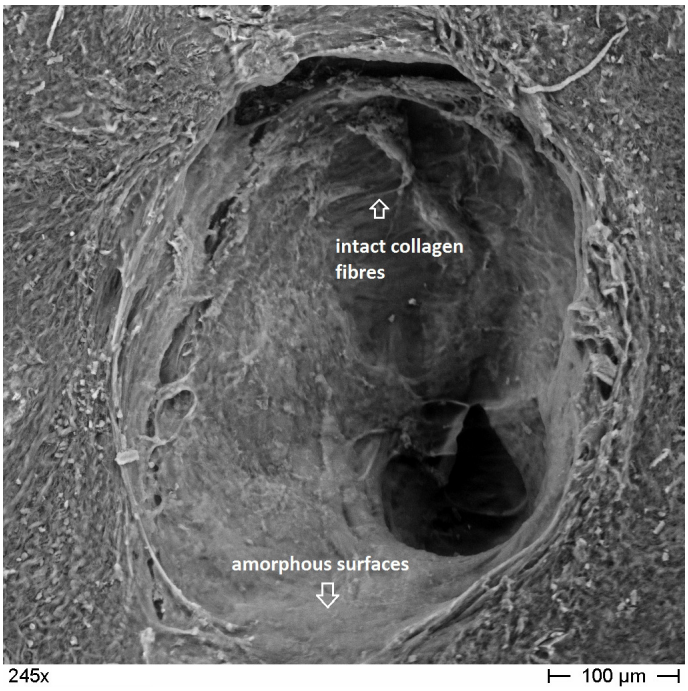

Figure 5.8. – Electron microscope image of a PIRL sclerostomy conducted with a pulse energy of 175 µJ at a magnification of 245x.

5.2.4. Discussion

The objective of this study was a feasibility analysis and a quantified assessment of the created opening area and collateral damage zones after a PIRL-FAST. The gold standard surgery for glaucoma patients with an increased intraocular pressure (IOP) is trabeculectomy [160]. However, this treatment can also cause several complications, wherefore new effective minimally invasive therapeutic approaches are of great interest. The PIRL-FAST enables a minimally invasive surgical intervention to lower the intraocular pressure (IOD) for glaucoma treatment. Since thermal effects and collateral damage to the adjacent tissue seems to affect the success rate of laser sclerostomies, the outcomes in this study are compared to other values for sclerostomy found in literature.

In this PIRL study, the lowest average thermal damage distance was 38 µm for PIRL-FAST with a pulse energy of 175 µJ and hence higher than expected from previous

experience. In earlier studies, PIRL cuts in cornea on fresh porcine globes had a smaller thermal damage zone in the adjacent tissue with an expansion in the range of 15 µm to 35 µm [44]. A reason for the bigger average thermal damage zone can be that the laser fibre was guided by free hand, since in certain areas more damage was visible, but also histological sections with no signs of thermal damage existed as presented in figure 5.7. A feed released automatically by a translation stage can ensure a constant speed for PIRL-FAST and probably improve the outcome in future experiments. Within all experimental groups with different applied pulse energies, only the group with the highest pulse energy of 250 µm showed a significantly increased size of the created PIRL-FAST and a bigger area of collateral damage compared to the other groups. This indicates that the size of the collateral damage correlates with the applied pulse energies.

Muller-Stolzenberg *et al.* [161] already described in 1991 a sclerostomy with an Excimer laser and reported on an average collateral damage zone of 140 µm. Jaffe *et al.* tested a high-power Argon laser to create a fistula and observed a thermal damage zone of 250 µm [162]. In comparison with the sclerostomies conducted with an Excimer and Argon laser, the presented test series with PIRL showed a smaller damage zone.

In Özler *et al.*, different infrared laser sclerostomies were compared [156]. In human tissue, a thermal damage zone of more than 100 µm was measured for a Nd:YAG laser coupled into a 600 µm fused silica fiber. Minimal thermal damage in the range of 20 µm was observed with a microsecond Er:YAG laser applying fluences between 3.6 J/cm^2 and 14.3 J/cm^2. However, Brinkmann *et al.* reported on a thermally altered zone varying from about 10 µm up to 500 µm for a sclerostomy in porcine eyes conducted with a microsecond Er:YAG laser at a fluence of 12 J/cm^2 [163]. In 1997, Kampmeier *et al.* [164] conducted further sclerostomies with an Er:YAG laser and a 550 µm quartz fiber in porcine eyes. In the latter study, relatively high pulse energies in the range of 10 mJ to 60 mJ with repetition rates from 5 to 17,5 Hz were applied. The created sclerostomies were analyzed via histology and Scanning Electron Microscopic Images. A homogeneous zone consisting of necrosis and wall ruptures had an extent of 25 µm. In case of PIRL-FAST no necrosis and wall ruptures were recognizable in the histological and electron microscopic analysis, but only a zone of altered cell structure without signs of necrosis was detected.

5.2.5. Conclusion

This study for the first time presents the application of the novel Picosecond Infrared Laser in combination with a fibre in sclerostomy for glaucoma treatment in porcine

eyes. PIRL-FAST with a sapphire fibre is a new minimally invasive instrument to create a stable connection from the conjunctiva to the anterior chamber. The obtained results from histological and electron microscopic investigations indicate an improvement in terms of reduced collateral damage in form of necrosis and wall ruptures compared to other promising laser sclerostomies such as Er:YAG laser applications in literature. This underlines the superiority of the PIRL regarding minimally invasive surgeries in glaucoma treatment. A correlation of applied pulse energies to the opening area of the sclerostomy and extent of collateral damage was indicated within a statistical analysis. Since the PIRL was already demonstrated as a successful tool for cutting distinct eye tissues with minimal collateral damage, this can pave the way for a new minimally invasive glaucoma surgery. After this first feasibility test, next necessary steps for PIRL-FAST are the analysis of optimal perforation size necessary for long-term drainage, wound healing, scarring and the pressure-lowering effect in further *in vivo* studies.

5.3. Conclusion

In this chapter, the DIVE process was applied in two proof-of-principle experiments for the treatment of glaucoma and otosclerosis. Especially the atraumatic ablation with PIRL can prove to be superior over traditional laser treatments and extent the field of applications for PIRL in ophthalmology and otorhinolaryngology. However, in both cases profound *in vivo* studies are necessary to evaluate the advantages in terms of improved healing outcomes for the new PIRL applications. In an important comparative wound healing study in skin with live rats, the results already demonstrated the substantial benefits of the PIRL. The scar area caused by PIRL incisions was significantly smaller than the scar area of the scalpel incisions.

6. Summary and Outlook

In medicine, lasers have not replaced mechanical tools and are still niche products in many medical disciplines in daily use. This raises the inevitable questions: Is laser surgery still in its infancy or will it remain a niche product in medical applications? Since lasers have been constantly increasing their range of applications for a wide variety of maladies over the last decades and were very successful in single disciplines such as ophthalmology, it can be assumed that lasers have a bright future ahead. In order to broaden the field of lasers in the future, the existing hurdles have to be identified, solved and the full potential of lasers better exploited.

A typical drawback in laser surgery is the excessive collateral damage to the adjacent tissue. This drawback is solved by the novel Picosecond Infrared Laser operating in the DIVE regime. The new PIRL reaches an unprecedented precision while simultaneously avoiding thermal and acoustic effects, shock wave propagation and ionization in the surgical zone. Another hurdle in laser surgery in several medical disciplines is often the low cutting speed. Thus, the current cutting speed in form of the ablation rate was evaluated for the PIRL in different soft tissues such as liver, skin, and cornea in the second chapter. For corneal surgery like cornea transplantation, the PIRL has already a sufficiently fast ablation rate, but for skin surgery an improvement will be necessary for a successful clinical use. Finally, the applicability of lasers is limited by optical breakdown. The maximum acceptable pulse energies in mJ to operate under the threshold of the laser-induced optical breakdown depend on the pulse duration and the spot size diameter. Typical acceptable pulse energies for pulse durations between 10 ps and 400 ps were in a range of sub-mJ up to approximately 12 mJ. With the identified optimal performance, the next generation PIRL scalpels can combine precision with minimal collateral damage and high cutting speed.

In the future, it will be necessary to develop new compact and reliable laser systems to improve the applicability of lasers in medicine; however also new specialized delivery optics can contribute to successfully establish laser applications. In chapter 3, a concept of a new surgical laser scalpel with a tapered fiber tip was presented. The initial idea of the new fibre tip design is to cut tissue with a geometrically optimized optical fibre tip shape, which not only guides laser light to the tissue, but also features a blade like shape. For this purpose, two shaped fibre tip designs were realized by

polishing two opposing sides of a sapphire fibre end tip with a 250 µm diameter under specifically tailored angles. The aim was to obtain a tapered fibre tip with a rectangular 25 µm x 250 µm endface and a tapered sharp fibre tip without a planar endface. Tissue cuts in skin and liver conducted with the shaped fibre tip designs showed no relevant difference between both to the naked eye. Cuts in soft tissue performed with a manually guided tapered fibre tip without a planar endface revealed a relative big cutting width and irregular cutting lines in Confocal Laser Scanning Microscope images compared to cuts of a scalpel. However, the new tip design enabled more precise cuts with regard to cutting width compared to other incisions conducted by other fibre tip designs found in literature.

Currently, a paradigm change in medical laser technologies can be observed moving pure cutting or diagnostic devices to a combination of both. The new term theragnostics describes this combination of therapy and diagnostics. The PIRL ablation with subsequent mass spectrometry analysis allows cutting and analyzing the ablated tissue with regard to its constituents. This is a huge potential for laser applications and enables not only the distinction of healthy and pathological tissue, but also the mapping of different regions within an organ such as distinct brain areas. An important first step within this chemical analytical method is the extraction of analytes from their natural environment. In chapter 4, protein extraction from tissue via laser ablation by PIRL and a conventional Er:YAG laser with microsecond pulse durations was compared. Although both lasers were capable to extract proteins in a similar weight range from soft tissues, the gentle PIRL-DIVE ablation process enabled to extract proteases with intact enzyme activity in contrast to the Er:YAG laser ablation. The intact enzyme activity indicates a fully maintained 3D-structure in terms of the tertiary structure of proteins, whereas in case of the microsecond laser a structural degradation occurred. This special feature of PIRL is not only interesting for later surgical applications and subsequent tissue recognition, but can also contribute as a new effective tool in fundamental proteomics research.

In some laser applications, current lasers already outperform conventional mechanical tools as for precision, easy handling, or collateral tissue damage in medicine. However, there is still room for further improvements, since the healing outcomes are limited in some treatments. In chapter 5, two further potential applications for the PIRL in the treatment of glaucoma and otosclerosis were evaluated. First proof-of principle experiments for stapedotomy to treat otosclerosis were conducted on human cadaver tissue. In this surgical procedure, a hole is created in the footplate within the middle ear to place a piston-shaped prosthesis in order to establish a flexible connection between the stapes bone and the footplate. The created perforation in stapes surgery conducted by PIRL showed superior results regarding precision and thermal damage in electron microscopy and histological examinations compared to a conventional Er:YAG laser.

Moreover, the gentle ablation of PIRL with strongly reduced shockwave effects can avoid previous problems such as inner ear damage. In the second feasibility test on porcine eyes in ophthalmology, PIRL was coupled into a fibre to create an opening into the sclera for glaucoma treatment, a so-called sclerostomy. An improvement in terms of reduced collateral damage in form of necrosis and wall ruptures was apparent in histological and electron microscopic images compared to other promising laser sclerostomies such as Er:YAG laser applications in literature. Both studies can expand the potential area of application for PIRL in the future, however extensive tests in living animals will be essential to prove the superiority of the PIRL over conventional lasers.

The current success in surgical procedures still depends strongly on the experience of the performing surgeon. Available surgical robots are actually telemanipulators operated by experienced surgeons. To obtain improved quality outcomes independent of the surgeon's personal expertise, the next generation of surgical robots will need noticeable more real-time information to better control the surgical procedure itself within the operating theaters. New endeavors to achieve not only the goal of single cell cutting precision, but also real-time diagnostics to effectively guide surgical robots during operations can advance robotic surgery beyond our present horizon. The PIRL technology in combination with mass spectrometry and further diagnostic and imaging methods such as Optical Coherence Tomography can contribute to these developments and pave the way for a bright future of lasers in medical applications.

A. Surgical Laser Scalpel with a Tapered Fiber Tip

A.1. CAD Model of Fibre

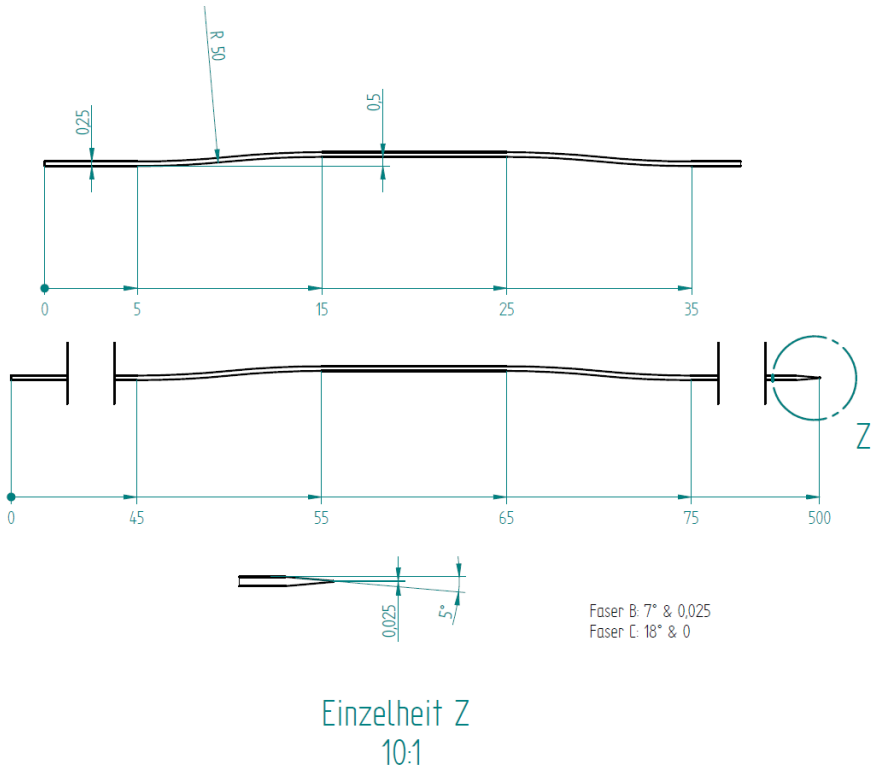

Figure A.1. – CAD model of the fibre for the ZEMAX simulation. The modeled fibres had a cylindrical shape with a diameter of 250 µm, a length of around 500 mm and was bend two times with a curvature of 50 mm to obtain a flattop beam profile.

A.2. Flattop Beam Profil within the Fibre before the Tapered Fibre Tip

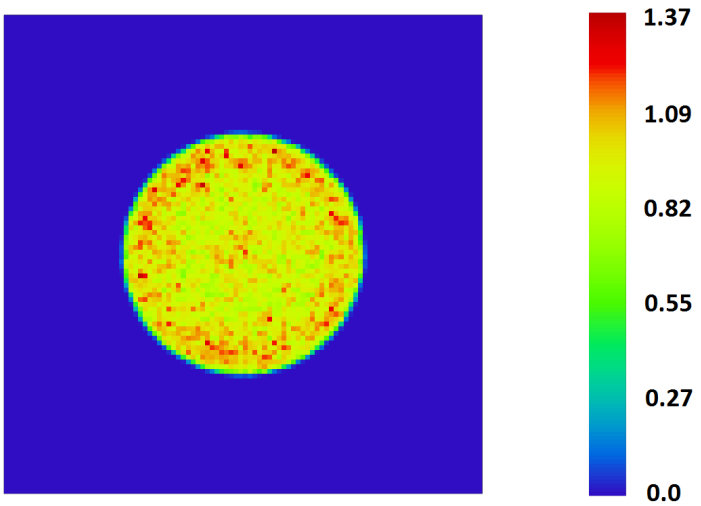

Figure A.2. – Laser light intensity distribution within the fibre before the tapered fibre tip. The intensity distribution has a flattop profile. The color bar represents arbitrary intensity units.

B. Proteome Analysis of Tissues in Bio-diagnostics: Comparison of Two Infrared Lasers

B.1. Laemmli buffer

Reagent	**Composition**	**Weight/volume**
Tris(hydroxymethyl)-aminomethan-Chloride	0.225 M	2.723 g/100 ml
Glycerol	50 vol%	50 ml
Bromphenol Blue	0.05 gw%	50 mg
Dithiothreitol (DTT) (freshly added before use)	0.25 M	3.86 g/100 ml
Sodium Lauryl Sulfate	5 gw%	5 g
Water		rest

Table B.1. – Laemmli buffer: 100 mL final volume, pH 6.8. For pH adjustment sodiumhydroxide was used.

B.2. Columns for LC-MS/MS analysis

	nanoACQUITY UPLC Symmetry C18 trap column (trap column)	**nanoACQUITY UPLC column BEH 130 C18 (separation column)**
Pore size [Å]	100	100
Particle size [µm]	5	1.7
Length [mm]	20	250
Inner diameter [µm]	180	75
Buffer	A: 0.1 % Formic Acid in HPLC-H_20 B: 0.1 % Formic Acid in Acetonitrile	A: 0.1 % Formic Acid in HPLC-H_20 B: 0.1 % Formic Acid in Acetonitrile

Table B.2. – Columns for LC-MS/MS analysis with a nano-ultra pressure liquid chromatography system(nano-UPLC, nanoACQUITY, Waters, Manchester, UK).

B.3. MALDI MS parameters

Parameter	Value
Measuring range [m/z]	800 to 1320
Laser intensity, [%]	40
Spectra per laser pulse	2000
Number of overall spectra per measurement	2000
Polarity	positive
Voltage of ion source 1 [kV]	20.00
Voltage of ion source 2 [kV]	18.10
Voltage on lens [kV]	8.80
Reflector voltage 1 [kV]	21.00
Reflector voltage 2 [kV]	11.00

Table B.3. – MALDI paraemters for recorded spectra via a TOF-mass spectrometer (Bruker UltraleXtreme Smartbeam II Laser, Bremen, Germany).

B.4. Sequences and protonated monoisotopic masses of angiotensin peptides

The sequences and protonated monoisotopic masses of angiotensin peptides were taken from Hildebrand *et al.* [121].

Peptide	**Sequence**	**Monoisotopic peptide mass $[M+H]^+$**
ANG-1-10	DRVYIHPFHL	1296.7
ANG-2-10	RVYIHPFHL	1181.7
ANG-3-10	VYIHPFHL	1025.6
ANG-4-10	YIHPFHL	926.5
ANG-5-10	IHPFHL	763.5
ANG-6-10	HPFHL	650.3
ANG-1-9	DRVYIHPFH	1183.6
ANG-1-8	DRVYIHPF	1046.5
ANG-1-7	DRVYIHP	899.5
ANG-2-8	RVYIHPF	931.5
ANG-3-8	VYIHPF	775.4
ANG-4-8	YIHPF	676.3

Table B.4. – Sequences and protonated monoisotopic masses of angiotensin peptides that were generated in the condensate of the aerosol obtained by irradiation of liver tissue with PIRL.

B.5. Negative Control of Angiotensin I

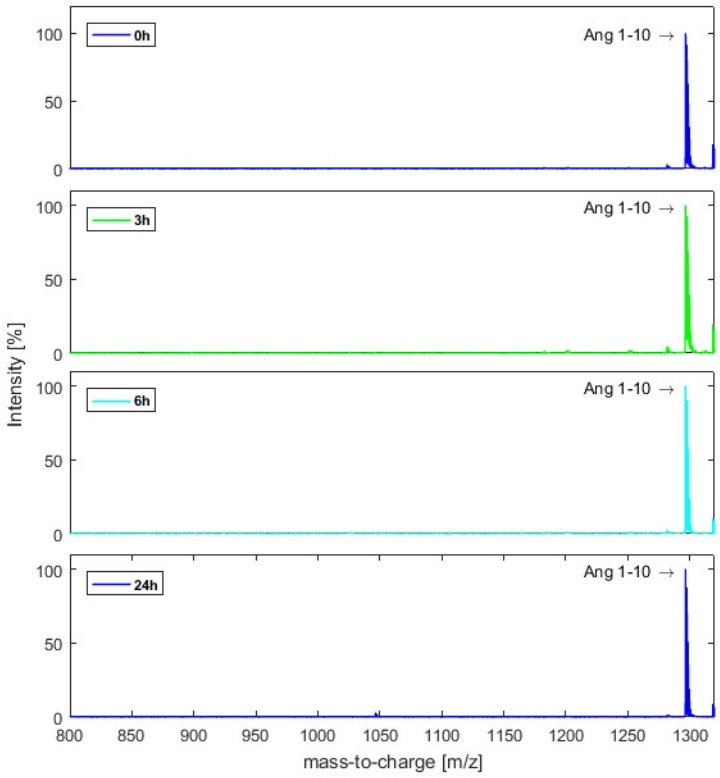

Figure B.1. – MALDI-TOF mass spectra of angiotensin 1-10 (c=10^{-5}) was diluted in purified water (18.2 MΩ·cm). Reaction products were detected by MALDI-TOF MS after 0h, 3h, 6h, and 24h. The obtained spectra displayed only intact Angiotensin I (Ang 1-10) at all time points and ensured that Angiotensin I (Ang 1-10) was not degraded by other environmental influences.

List of Figures

List of Tables

Bibliography

[1] M. Mahvash, L. M. Voo, D. Kim, K. Jeung, J. Wainer, and A. M. Okamura, IEEE Transactions on Biomedical Engineering **55**, 848 (2008).

[2] S. Saha, S. Pal, and J. A. Albright, Journal of biomechanical engineering **104**, 245 (1982).

[3] A. L. McKenzie, Physics in medicine and biology **29**, 619 (1984).

[4] B. Girard, K. Franjic, M. Cloutier, D. Wilson, C. M. L. Clokie, B. C. Wilson, and R. J. D. Miller, SPIE Proc Ser **6261**, 62612J (2006).

[5] M. H. Niemz, *Laser-Tissue Interactions*, 3rd ed. (Springer Science & Business Media, 2007).

[6] R. D. Gerste, in *Etablierte Operationsverfahren und neue Lasertechnik* (Springer, 2016) pp. 61–68.

[7] O. T. Tan, K. Sherwood, and B. A. Gilchrest, New England Journal of Medicine **320**, 416 (1989).

[8] R. Hibst and U. Keller, Lasers in Surgery and Medicine **9**, 338 (1989).

[9] D. E. Dolmans, D. Fukumura, and R. K. Jain, Nature Reviews Cancer **3**, 380 (2003).

[10] B. Choi and a. J. Welch, Lasers in surgery and medicine **29**, 351 (2001).

[11] M. J. C. van Gemert and A. J. Welch, Lasers in Surgery and Medicine **9**, 405 (1989).

[12] L. Svaasand, T. Boerslid, and M. Oeveraasen, Lasers in surgery and medicine **5**, 589 (1985).

[13] K. Franjic, M. L. Cowan, D. Kraemer, and R. J. D. Miller, Optics express **17**, 22937 (2009).

[14] L. V. Wang, *Photoacoustic Imaging and Spectroscopy* (CRC Press, 2009).

[15] R. Steiner, Laser and IPL Technology in Dermatology and Aesthetic Medicine , 23 (2011).

[16] M. Greenspan and C. E. Tschiegg, The Journal of the Acoustical Society of America **31**, 75 (1959).

[17] C. R. Hill, J. C. Bamber, and G. R. ter Haar, *Physical Principles of Medical Ultrasonics* (John Wiley & Sons, 2005).

[18] Z. E. Begui, The Journal of the Acoustical Society of America **26**, 365 (1954).

[19] S. News, Science **330**, 1612 (2010).

[20] E. Pastrana, Nature Methods **8**, 24 (2011).

[21] J. L. Boulnois, Lasers in Medical Science **1**, 47 (1986).

[22] A. J. Welch and M. J. Van Gemert, *Optical-thermal response of laser-irradiated tissue* (Springer Berlin, 2011).

[23] H. Newesely, Journal of oral rehabilitation **4**, 97 (1977).

[24] R. Srinivasan, Journal of Vacuum Science & Technology B: Microelectronics and Nanometer Structures **1**, 923 (1983).

[25] C. Downes, A. Collins, and R. Johnson, Biophysical Journal **25**, 129 (1979).

[26] J. Bille, in *Ultrashort Laser Pulses in Biology and Medicine* (Springer, 2008) pp. 53–73.

[27] F. H. Loesel, M. H. Niemz, J. F. Bille, and T. Juhasz, IEEE Journal of Quantum Electronics **32**, 1717 (1996).

[28] C. A. Puliafito and R. F. Steinert, IEEE Journal of Quantum Electronics **20**, 1442 (1984).

[29] A. Aristeidou, E. V. Taniguchi, M. Tsatsos, R. Muller, C. McAlinden, R. Pineda, and E. I. Paschalis, Eye and Vision **2**, 12 (2015).

[30] A. Vogel, Physics in medicine and biology **42**, 895 (1997).

[31] A. G. Doukas, D. J. McAuliffe, and T. J. Flotte, Ultrasound in Medicine and Biology **19**, 137 (1993).

[32] A. Tokmakoff, Science **317**, 54 (2007).

[33] M. L. Cowan, B. D. Bruner, N. Huse, J. R. Dwyer, B. Chugh, E. T. J. Nibbering, T. Elsaesser, and R. J. D. Miller, Nature **434**, 199 (2005).

[34] S. Ashihara, N. Huse, A. Espagne, E. T. J. Nibbering, T. Elsaesser, S. Ashihara, N. Huse, A. Espagne, E. T. J. Nibbering, and T. Elsaesser, The Journal of Physical Chemistry A **111**, 1 (2007).

[35] K. L. Vodopyanov, The Journal of Chemical Physics **94**, 5389 (1991).

[36] K. Franjic and D. Miller, Physical chemistry chemical physics : PCCP **12**, 5225 (2010).

[37] A. Vogel and V. Venugopalan, Chemical Rev. **103**, 577 (2003).

[38] L. Ren, W. D. Robertson, R. Reimer, C. Heinze, C. Schneider, D. Eggert, P. Truschow, N.-O. Hansen, P. Kroetz, J. Zou, and R. J. D. Miller, Nanotechnology **26**, 284001 (2015).

[39] S. Amini-Nik, D. Kraemer, M. L. Cowan, K. Gunaratne, P. Nadesan, B. A. Alman, and R. J. D. Miller, PloS one **5**, 1 (2010).

[40] A. Böttcher, T. S. Clauditz, R. Knecht, S. Kucher, W. Wöllmer, W. Wilczak, P. Krötz, N. Jowett, C. V. Dalchow, A. Münscher, and R. J. D. Miller, Laryngoscope **123**, 2770 (2013).

[41] A. Böttcher, S. Kucher, R. Knecht, N. Jowett, P. Krötz, R. Reimer, U. Schumacher, S. Anders, A. Münscher, C. V. Dalchow, and R. J. D. Miller, European Archives of Oto-Rhino-Laryngology **272**, 941 (2015).

[42] M. Hess, M. D. Hildebrandt, F. Müller, S. Kruber, P. Kroetz, U. Schumacher, R. Reimer, M. Kammal, K. Püschel, W. Wöllmer, and D. Miller, European archives of oto-rhino-laryngology **270**, 2927 (2013).

[43] S. Linke, L. Ren, A. Frings, J. Steinberg, W. Wöllmer, T. Katz, R. Reimer, N.-O. Hansen, N. Jowett, G. Richard, and R. Dwayne Miller, Der Ophthalmologe **111**, 523 (2014).

[44] S. J. Linke, A. Frings, L. Ren, A. Gomolka, U. Schumacher, R. Reimer, N. O. Hansen, N. Jowett, G. Richard, and R. J. D. Miller, PLoS ONE **10**, 1 (2015).

[45] N. Jowett, W. Wöllmer, A. M. Mlynarek, P. Wiseman, B. Segal, K. Franjic, P. Krötz, A. Böttcher, R. Knecht, and R. J. D. Miller, JAMA otolaryngology–head & neck surgery **139**, 828 (2013).

[46] N. Jowett, W. Wöllmer, R. Reimer, J. Zustin, U. Schumacher, P. W. Wiseman, A. M. Mlynarek, A. Böttcher, C. V. Dalchow, B. B. Lörincz, R. Knecht, and R. J. D. Miller, Otolaryngology–head and neck surgery **150**, 385 (2013).

[47] H. Petersen, F. Tavakoli, S. Kruber, A. Münscher, A. Gliese, N.-O. Hansen, S. Uschold, D. Eggert, W. D. Robertson, T. Gosau, S. Sehner, M. Kwiatkowski, H. Schlüter, U. Schumacher, R. Knecht, and R. J. D. Miller, Lasers in Surgery and Medicine **48**, 385 (2016).

[48] E. De Hoffmann and V. Stroobant, *Mass spectrometry: principles and applications* (John Wiley & Sons, 2007).

[49] R. A. Zubarev and A. Makarov, Anal Chem **85**, 5288 (2013).

[50] J. H. Gross, *Mass Spectrometry* (Springer, 2017) p. 753.

[51] J. Fenn, M. Mann, M. Chin-kai, W. Shek-fu, and C. Y. O. Whitehouse, Science **246**, 64 (1989).

[52] F. Hillenkamp and M. Karas, Analytical chemistry **63**, 1193 (1991).

[53] M. Vogeser, U. Kobold, and D. Seidel, Deutsches Arzteblatt-Arztliche Mitteilungen-Ausgabe A **104**, 2194 (2007).

[54] U. Garg and H. Hammett-Stabler, *Clinical Applications of Mass Spectrometry* (New York: Humana Press, 2010).

[55] B. Fatou, P. Saudemont, E. Leblanc, D. Vinatier, V. Mesdag, M. Wisztorski, C. Focsa, M. Salzet, M. Ziskind, and I. Fournier, Scientific reports **6**, 25919 (2016).

[56] D. Cornett, M. Reyzer, P. Chaurand, and R. Caprioli, Nature Methods **10**, 828 (2007).

[57] W. Stummer, U. Pichlmeier, T. Meinel, O. D. Wiestler, F. Zanella, and H. J. Reulen, Lancet Oncology **7**, 392 (2006).

[58] A. Zumbusch, G. R. Holtom, and X. S. Xie, Physical Review Letters **82**, 4142 (1999).

[59] T. Meyer, M. Chemnitz, M. Baumgartl, T. Gottschall, T. Pascher, C. Matthaeus, B. F. M. Romeike, B. R. Brehm, J. Limpert, A. Tuennermann, M. Schmitt, B. Dietzek, and J. Popp, Analytical Chemistry **85**, 6703 (2013).

[60] T. Meyer, O. Guntinas-Lichius, F. von Eggeling, G. Ernst, D. Akimov, M. Schmitt, B. Dietzek, and J. Popp, Head and Neck **35** (2013), 10.1002/hed.23139.

[61] T. Meyer, N. Bergner, C. Bielecki, C. Krafft, D. Akimov, B. F. M. Romeike, R. Reichart, R. Kalff, B. Dietzek, and J. Popp, Journal of Biomedical Optics **16**, 21110 (2011).

[62] J. Balog, L. Sasi-Szabó, J. Kinross, M. R. Lewis, L. J. Muirhead, K. Veselkov, R. Mirnezami, B. Dezso, L. Damjanovich, A. Darzi, J. K. Nicholson, and Z. Takáts, Science translational medicine **5**, 194ra93 (2013).

[63] J. Zhang, J. Rector, J. Q. Lin, J. H. Young, M. Sans, N. Katta, and J. Liu, Science Translational Medicine **9**, eaan3968 (2017).

[64] P. Steffen, M. Kwiatkowski, W. D. Robertson, A. Zarrine-Afsar, D. Deterra, V. Richter, and H. Schlüter, Journal of Proteomics **134**, 5 (2016).

[65] M. Kwiatkowski, M. Wurlitzer, A. Krutilin, P. Kiani, R. Nimer, M. Omidi, A. Mannaa, T. Bußmann, K. Bartkowiak, S. Kruber, S. Uschold, P. Steffen, J. Lübberstedt, N. Küpker, H. Petersen, R. Knecht, N.-O. Hansen, A. Zarrine-Afsar, W. Robertson, R. Miller, and H. Schlüter, Journal of Proteomics **134**, 193 (2016).

[66] Y. Lu, C. L. Pieterse, W. D. Robertson, and R. J. D. Miller, Analytical chemistry, submitted (2017).

[67] J. Zou, C. Wu, W. D. Robertson, L. V. Zhigilei, and R. J. Miller, Journal of Chemical Physics **145**, 204202 (2016).

[68] M. Wurlitzer, E. Hessling, K. Rinas, M. M. Fuh, H. Petersen, F. Ricklefs, S. Maier, S. Kruber, N.-O. Hansen, R. J. D. Miller, and H. Schlüter, Journal of Neurology, submitted (2017).

[69] J. Zou, F. Talbot, A. Tata, L. Ermini, K. Franjic, M. Ventura, J. Zheng, H. Ginsberg, M. Post, D. R. Ifa, D. Jaffray, R. J. D. Miller, and A. Zarrine-Afsar, Analytical Chemistry **87**, 12071 (2015).

[70] J. Dahmen, C. Otte, M. Fuh, S. Maier, M. Schlüter, S. Antoni, and N. Hansen, in *16. Jahrestagung der Deutschen Gesellschaft für Computer- und Roboter Assistierte Chirurgie (Curac)* (2017) pp. 1–5.

[71] M. H. Goetz, F. Baptista, J. P. Fischer, C. Messer, N. Suhm, and J. F. Bille, Proc. SPIE **2323**, 218 (1995).

[72] J. T. Walsh and T. F. Deutsch, Lasers in surgery and medicine **9**, 314 (1989).

[73] T. G. Barton, M. Christ, H.-J. Foth, and K. Hormann, in *Proc. SPIE*, Vol. 2323 (1995) pp. 185–195.

[74] M. Christ, T. G. Barton, K. Hormann, and H.-J. Foth, in *SPIE*, Vol. 2327 (1994) pp. 394–401.

[75] F. Pene, E. Courtine, A. Cariou, and J.-P. Mira, Critical Care Medicine **37**, S50 (2009).

[76] J. T. Walsh, T. J. Flotte, R. R. Anderson, and T. F. Deutsch, Lasers in surgery and medicine **8**, 108 (1988).

[77] R. J. Lane, R. Linsker, J. J. Wynne, A. Torres, and R. G. Geronemus, Archives of Dermatology **121**, 609 (1985).

[78] T. S. Alster and J. R. Lupton, Dermatologic clinics **19**, 453 (2001).

[79] S. F. Badylak, Seminars in cell & developmental biology **13**, 377 (2002).

[80] R. K. Shori, A. A. Walston, O. M. Stafsudd, D. Fried, and J. T. Walsh, Special Topics J. Quantum Electronics **7**, 959 (2001).

[81] J. P. Cummings and J. T. Walsh, Applied Physics Letters **62**, 1988 (1993).

[82] R. L. Bronaugh, R. F. Stewart, and E. R. Congdon, Toxicology and Applied Pharmacology **62**, 481 (1982).

[83] W. R. Galey, H. K. Lonsdale, and S. Nacht, Journal of Investigative Dermatology **67**, 713 (1976).

[84] N. J. Vardaxis, T. A. Brans, M. E. Boon, R. W. Kreis, and L. M. Marres, Journal of anatomy **190**, 601 (1997).

[85] M. von Zglinicki, T. Lindberg, G. M. Roomans, and B. Forslind, Acta Derm Venereol **73. Jg.**, S. 340 (1993).

[86] R. E. Neuman and M. A. Logan, Journal of Biological Chemistry **186**, 549 (1950).

[87] D. A. Parry and A. S. Craig, in *Ultrastructure of the connective tissue matrix* (Martinus Nijhoff Publishers, 1984) 3rd ed., pp. 34–64.

[88] S. Middleton, Veterinary Clinics of North America - Food Animal Practice **26**, 557 (2010).

[89] M. Pircher, E. Götzinger, R. Leitgeb, A. Fercher, and C. Hitzenberger, Optics express **11**, 2190 (2003).

[90] F. E. Fantes and G. O. Waring, Lasers in Surgery and Medicine **9**, 533 (1989).

[91] R. Kaufmann and R. Hibst, Lasers in Surgery and Medicine **19**, 324 (1996).

[92] F. H. Loesel, P. Brockhaus, J. P. Fischer, M. H. Götz, F. Noack, and J. F. Bille, Proc. SPIE **2323**, 227 (1994).

[93] B. Girard, *An Evaluation of the Biophysical Effects of Ultrafast Lasers on Osseous Tissues* (2007).

[94] H. Hussein, in *Optical and Laser Technology in Medicine* (International Society for Optics and Photonics, 1986) pp. 59–67.

[95] S. Thomas, J. Pensel, W. Meyer, and F. Wondrazek, in *Laser lithotripsy* (Springer Berlin Heidelberg, 1988) pp. 151–156.

[96] V. Bredikhin, V. Kamensky, N. Sapogova, V. Elagin, M. Shakhova, L. Snopova, and N. Bityurin, Applied Physics A **122**, 181 (2016).

[97] D. S. Kuznetsova, M. M. Karabut, V. V. Elagin, M. A. Shakhova, V. I. Bredikhin, O. S. Baskina, L. B. Snopova, A. V. Shakhov, and V. A. Kamensky, Optics and Photonics Journal **5**, 1 (2015).

[98] N. Sapogova, V. Bredikhin, N. Bityurin, V. Kamensky, V. Zhigarcov, and V. Yusupov, Biomedical Optics Express **8**, 104 (2017).

[99] D. Kuznetsova, V. Elagin, M. Karabut, M. Shakhova, V. Bredikhin, L. Snopova, A. Shakhov, N. Sapogova, N. Bityurin, V. Bagratashvili, and V. Kamensky, Journal of Innovative Optical Health Sciences **09**, 1650011 (2016).

[100] A. J. Costello, D. E. Johnson, and D. M. Bolton, Lasers in surgery and medicine **12**, 121 (1992).

[101] K. Stock, T. Stegmayer, R. Graser, W. Förster, and R. Hibst, Lasers in Surgery and Medicine **44**, 815 (2012).

[102] J. B. Wachtman and D. G. Lam, Journal of the American Ceramic Society **42**, 254 (1959).

[103] R. W. Waynant, M. N. Ediger, and M. Fink, Journal of Laser Applications **2**, 45 (1990).

[104] I. H. Malitson and M. J. Dodge, Journal Of The Optical Society Of America **62**, 1405 (1972).

[105] C. T. McCarthy, M. Hussey, and M. D. Gilchrist, Damage Assessment of Structures Vi **293-294**, 769 (2005).

[106] P. Picotti, B. Bodenmiller, and R. Aebersold, Nature Methods **10**, 24 (2012).

[107] R. Aebersold and M. Mann, Nature **537**, 347 (2016).

[108] R. M. Caprioli, T. B. Farmer, and J. Gile, Analytical Chemistry **69**, 4751 (1997).

[109] Aldridge, W. N., R. C. Emery, and B. W. Street, Biochemical Journal **77**, 326 (1960).

[110] S. Trimpin, S. M. Weidner, J. Falkenhagen, and C. N. McEwen, Analytical Chemistry **79**, 7565 (2007).

[111] S. G. Park and K. K. Murray, Analytical Chemistry **84**, 3240 (2012).

[112] F. Donnarumma, F. Cao, and K. K. Murray, Journal of the American Society for Mass Spectrometry **27**, 108 (2016).

[113] F. Donnarumma and K. K. Murray, Journal of Mass Spectrometry **51**, 261 (2016).

[114] M. Kwiatkowski, M. Wurlitzer, M. Omidi, L. Ren, S. Kruber, R. Nimer, W. D. Robertson, A. Horst, R. J. D. Miller, and H. Schlüter, Angewandte Chemie - International Edition **54**, 285 (2015).

[115] B. C. Steel, D. R. McKenzie, M. M. Bilek, N. J. Nosworthy, and C. G. dos Remedios, Biophysical Journal **91**, L66 (2006).

[116] J. Rykl, J. Thiemann, S. Kurzawski, T. Pohl, J. Gobom, W. Zidek, and H. Schlüter, Journal of hypertension **24**, 1797 (2006).

[117] J. R. Wiśniewski, A. Zougman, N. Nagaraj, and M. Mann, Nature Methods **6**, 359 (2009).

[118] C. C. Wu and J. R. Yates, Nature biotechnology **21**, 262 (2003).

[119] B. Domon, Science **312**, 212 (2006).

[120] M. J. Peach, Physiological reviews **57**, 313 (1977).

[121] D. Hildebrand, P. Merkel, L. F. Eggers, and H. Schlüter, PLoS ONE **8**, e64027 (2013).

[122] R. Nelson, M. Rainbow, D. Lohr, and P. Williams, Science **246**, 1585 (1989).

[123] M.-Z. Huang, S.-S. Jhang, C.-N. Cheng, S.-C. Cheng, and J. Shiea, The Analyst **135**, 759 (2010).

[124] J. J. Shea, Annals of Otology, Rhinology & Laryngology **67**, 932 (1958).

[125] W. Arnold and R. Häusler, *Otosclerosis and Stapes Surgery* (Karger, 2007).

[126] U. Fisch, Otology & Neurotology **4**, 112 (1982).

[127] R. C. Perkins, The Laryngoscope **90**, 228 (1980).

[128] Z.-Z. Li, L. Reinisch, and W. P. Van de Merwe, Lasers in Surgery and Medicine **12**, 79 (1992).

[129] S. Jovanovic, U. Schonfeld, V. Prapavat, A. Berghaus, R. Fischer, H. Scherer, and G. J. Muller, Lasers in Surgery and Medicine **21**, 341 (1997).

[130] D. M. a. Kamalski, I. Wegner, R. a. Tange, R. Vincent, I. Stegeman, G. J. M. van der Heijden, and W. Grolman, Otology & Neurotology **35**, 1046 (2014).

[131] A. Huber, T. Linder, and U. Fisch, Otology and Neurotology **22**, 311 (2001).

[132] R. Häusler, P. J. Schär, H. Pratisto, H. P. Weber, and M. Frenz, Acta Oto-Laryngologica **119**, 207 (1999).

[133] W. Szyfter, D. Mielcarek-kuchta, D. Mi, and M. Anna, Otology & Neurotology, **34**, 29 (2012).

[134] A. P. Timoshenko, A. Oletski, J. M. Prades, A. Asanau, C. Martin, P. Bertholon, and C. Martin, Acta Oto-Laryngologica **129**, 217 (2009).

[135] E. Z. Stucken, K. D. Brown, and S. H. Selesnick, Otology & Neurotology **33**, 1297 (2012).

[136] S. G. Lesinski, Lasers in Surgery and Medicine **10**, 448 (1990).

[137] W. Szyfter, D. Mielcarek-Kuchta, D. Miętkiewska-Leszniewska, J. Łączkowska-Przybylska, and A. Młodkowska, European Archives of Oto-Rhino-Laryngology **272**, 61 (2015).

[138] S. Jovanovic, U. Schönfeld, R. Fischer, M. Döring, V. Prapavat, G. Müller, and H. Scherer, Lasers in Surgery and Medicine **23**, 7 (1998).

[139] B. M. Lippert, S. Gottschlich, C. Külkens, B. J. Folz, H. Rudert, and J. a. Werner, Lasers in surgery and medicine **28**, 11 (2001).

[140] C. Parrilla, J. Galli, A. R. Fetoni, M. Rigante, and G. Paludetti, Otolaryngology - Head and Neck Surgery **138**, 507 (2008).

[141] T. Keck, H. Bürner, and G. Rettinger, The Laryngoscope **115**, 1627 (2005).

[142] C. Arnoldner, B. Schwab, and T. Lenarz, Otology & Neurotology **27**, 458 (2006).

[143] S. Resnikoff, D. Pascolini, D. Etya'ale, I. Kocur, R. Pararajasegaram, G. P. Pokharel, and S. P. Mariotti, Bulletin of the World Health Organization **82**, 844 (2004).

[144] R. D. Gerste, Deutsches Arzteblatt **105**, A (2008).

[145] T. M. Shaarawy, M. B. Sherwood, R. Hitchings, and J. G. Crowston, *Glaucoma: Medical diagnosis & therapy* (Elsevier Ltd, 2009) pp. 307–315.

[146] J. R. Soohoo, L. K. Seibold, N. M. Radcliffe, and M. Y. Kahook, Canadian Journal of Ophthalmology **49**, 528 (2014).

[147] B. Bill, Anders; Svedbergh, Acta ophthalmologica **50**, 295 (1972).

[148] A. Bill, Experimental Eye Research **25**, 291 (1977).

[149] H. A. Quigley, The New England Journal of Medicine **328**, 1097 (1993).

[150] C. I. Phillips, British Journal of Ophthalmology **40**, 136 (1956).

[151] A. G. Iwach, H. D. Hoskins, M. V. Drake, and C. J. Dickens, Ophthalmology **100**, 356 (1993).

[152] P. Bettin and P. Khaw, *Glaucoma Surgery* (Karger, 2017).

[153] T. Gherezghiher, W. F. March, M. C. Koss, and R. E. Nordquist, Archives of Ophthalmology **103**, 1543 (1985).

[154] W. F. March, D. Bernitsky, T. Gherezghiher, M. Koss, J. Hays, and R. Nordquist, Glaucoma **7**, 43 (1985).

[155] W. F. March, T. Gherezghiher, M. C. Koss, R. P. Shaver, W. D. Heath, and R. D. Nordquist, Arch Ophthalmol **103**, 860 (1985).

[156] S. A. Oezler, R. A. Hill, J. J. Andrews, G. Baerveldr, and M. W. Berns, Investigative ophthalmology & visual science **32**, 2498 (1991).

[157] B. D. S. Allan, P. P. Van Saarloos, A. V. Russo, R. L. Cooper, and I. J. Constable, Eye **7**, 47 (1993).

[158] J. A. McAllister and P. O. Watts, Eye **7**, 656 (1993).

[159] M. L. McHam, D. L. Eisenberg, J. S. Schuman, and N. Wang, Ophthalmic Surgery, Lasers and Imaging Retina **28**, 55 (1997).

[160] P. T. Khaw and D. Siriwardena, The British journal of ophthalmology **83**, 1 (1999).

[161] N. Muller-Stolzenburg, M. von Haebler, C. Erb, and H. J. Buchwald, Investigative ophthalmology & visual science **32**, 941 (1991).

[162] G. J. Jaffe, G. A. Williams, W. F. Mieler, and R. L. Radius, American journal of ophthalmology **106**, 391 (1988).

[163] R. Brinkmann, G. Droeger, D. Mohrenstecher, and R. Birngruber, Lasers in Ophthalmology III **2632**, 10 (1996).

[164] J. Kampmeier, M. Klafke, R. Hibst, S. Wierschin, E. Schütte, and R. Steiner, Klinische Monatsblätter für Augenheilkunde **211**, 48 (1997).

The following publications have been generated in the course of this dissertation.

Paper 1
Comparative study of wound healing in rat skin following incision with a novel picosecond infrared laser (PIRL) and different surgical modalities.
H. Petersen, F. Tavakol, S. Kruber, A. Münscher, A. Gliese, N.-O.Hansen, **S. Uschold**, D. Eggert, W. Robertson, T. Gosau, S. Sehner, M. Kwiatkowski, H. Schlüter, U. Schumacher, R. Knecht, R. J. D. Miller, Lasers in Surgery and Medicine, 48(4):385-391, 2016.

Paper 2
Homogenization of tissues via picosecond-infrared laser (PIRL) ablation: Giving a closer view on the in-vivo composition of protein species as compared to mechanical homogenization.
M. Kwiatkowski, M. Wurlitzer, A. Krutilin, P. Kiani, R. Nimer, M. Omidi, A. Mannaa, T. Bussmann, K. Bartkowiak, S. Kruber, **S. Uschold**, P. Steffen, J. Lübberstedt, N. Küpker, H. Petersen, R. Knecht, N.-O. Hansen, A. Zarrine-Afsar, W. Robertson, R.J.D. Miller, H. Schlüter, Journal of Proteomics, 134:193-202, 2016.

Additional work in this thesis is based on the following submitted or accepted papers and manuscripts in preparation:

Paper 3
Measurement of Ablation rates in different soft tissues for a novel Picosecond Infrared Laser (PIRL).
S. Maier, D. Eggert, S. Kruber, N.-O. Hansen, J. Mehlan, H. Petersen, M. M. Fuh, H. Schlüter, and R. J. D. Miller, in preparation.

Paper 4
Proteome Analysis of Tissues in Bio-diagnostics: Comparison of Two Infrared Lasers.
A. Krutilin[1], **S. Maier**[1], R. Schuster, N.-O. Hansen, S. Kruber, M. Kwiatkowski, W. Robertson, R. J. D. Miller and H. Schlüter, Analytical Chemistry, in preparation.

[1] authors contributed equally.

Paper 5
Picosecond Infrared Laser (PIRL) application in stapes surgery - first experience in human temporal bones.
H. Petersen[2], A. Gliese[2], Y. Stober, **S. Maier**, N.-O. Hansen, S. Kruber, D. Eggert, M. Tóth, T. Gosau, H. Schlüter, K. Püschel, U. Schumacher, R. J. D. Miller, A. Münscher, C. Dalchow, Otology & Neurotology, accepted 2017.

Paper 6
Pikosekundenlaser- Faser-assistierte Sklerostomie (PIRL- FAST): Ein erster Machbarkeitsnachweis.
J. Mehlan, **S. Maier**, N.-O. Hansen, T. Gosau, D. Eggert, M. Spitzer, H. Petersen, S. J. Linke, and R. J. D. Miller, Der Ophthalmologe, accepted 2017.

Additional conference proceedings, patent and posters have been generated in the course of this dissertation:

Paper 7
Wound Healing Study and Ablation Rate Measurements with the Novel Picosecond Infrared Laser (PIRL).
S. Maier, N.-O. Hansen, S. Kruber, T. Gosau, D. Eggert, A. Gliese, H. Petersen, H. Schlüter, R. J. D. Miller, CLEO San Jose, Paper ATu3A.5, 2017.

Paper 8
Eine Machbarkeitsuntersuchung der massenspektrometrischen Gewebeanalyse mittels OCT-navigierter PIR-Laserablation.
J. Dahmen, C. Otte, M. Fuh, **S. Maier**, M. Schlueter, S. Antoni , N.-O. Hansen, R.J.D. Miller, H. Schlüter, A. Schlaefer, 16. Jahrestagung der Deutschen Gesellschaft für Computer- und Roboter Assistierte Chirurgie (CURAC), 112-116, 2017, *2nd Paper Awards Prize.*

Patent
LASER SURGERY APPARATUS FOR CONTACT LASER SURGERY.
R. J. D. Miller, **S. Uschold**, N.-O. Hansen, S. Kruber, European patent, EP 306 7005 B1.

[2] authors contributed equally.

Poster 1
A proteomic workflow for characterization of human skin biopsies by using picosecond infrared laser (PIRL).
P. Kiani, D. Eggert, T. Bussmann, J. H. Reuter, **S. Uschold**, N.-O. Hansen, R. J. D. Miller, H. Schlüter, 49. Jahrestagung der Deutschen Gesellschaft für Massenspektrometrie, 2016.

Poster 2
Stapedotomie mit dem Pikosekunden-Infrarot-Laser (PIRL) - erste Erfahrungen am humanen Felsenbein.
A. Gliese , H. Petersen, Y. Stober, **S. Maier**, N.-O. Hansen, T. Gosau, A. Münscher, M. Tóth, C. Dalchow, R. J. D. Miller, 88. Jahresversammlung der Deutschen Gesellschaft für HNO-Heilkunde, Kopf- und Hals-Chirurgie, 2017, *2nd Poster Awards Prize in the category Experimental.*

Poster 3
Picosecond infrared laser - fibre-assisted-sclerostomy (PIRL-FAST): A first proof of principle analysis.
J. Mehlan, **S. Maier**, N.-O. Hansen, T. Gosau, D. Eggert, M. S. Spitzer, H.Petersen, U. Schumacher, S. J. Linke, R. J. D. Miller, The Association for Research in Vision and Ophthalmology (ARVO) Annual Meeting, 2017.

Acknowledgment

It is my great pleasure to conclude my thesis with this acknowledgment, and to thank all the wonderful people I had the chance working together over the last couple of years.

First of all, I want to express my deepest gratitude to my supervisor Dwayne Miller, who gave me the chance to enter the exciting world of science in his group. His enthusiasm and out-of-the-box thinking inspired me all the way driving me continuously out of my comfort zone. In addition, a special thanks goes to my second advisor Florian Grüner, whose critical questions and advice greatly helped me during my PhD work.

I would like to thank all my colleagues in the Miller Group for the interesting discussions and wonderful working atmosphere. Especially, I would like to thank my post-docs Nils-Owe Hansen and Wesley Robertson for their steady advice and proof reading of my thesis. I am also grateful to my close colleagues in the PIRL-group - Lourie Pieterse, Frederik Busse, Andrey Krutilin and Peter Krötz for their steady support in daily challenges. Further, I'm deeply thankful to my long-time office mates Ara Choudhuri and Haider Zia for fruitful discussions going beyond the science world. I also want to deeply thank Heinrich Schwoerer for all his support in the last year of my PhD. Especially, Sebastian Kruber has to be mentioned as the coolest of all colleagues. He has an incredible humor and made me laugh even in the darkest moments of my PhD time.

I would like to offer my special thanks to our collaborators at the UKE campus. In particular, many thanks to Prof. Hartmut Schlüter and his current and former group members Parnian Kiani, Marcel Kwiatkowski, Marcus Wurlitzer, and Manka Marceline Fuh, who provided continuous support in mass spectrometry analysis. I would like to acknowledge Hannes Petersen and Alexandra Gliese, with whom it was a great pleasure to work together in several studies. Furthermore, I would like to thank Juliane Mehlan and Stephan Linke for the great collaboration in surgical applications for the PIRL in ophthalmology. I am very thankful to Dennis Eggert for his support in microscopy imaging. Moreover, I would like to thank our project managers of the ERC grant SUREPIRL Wolfgang Wöllmer, Nathan Jowett and once again Hannes Petersen for their tireless efforts to establish interdisciplinary collaborations and practical advises in medical questions.

I would like to thank the members of the technical groups - Friedjof Tellkamp, Martin Kollewe, Hendrik Schikora, Jan-Philipp Leimkohl, Djordje Gitaric and Josef Gonschior - who provided great help in engineering and electrical tasks.

Besides those already mentioned, there are many other colleagues I am deeply grateful: Dagmar Schröder-Huse, Frauke Kleinwort, Ulrike Krieger, Tania Hartin, Kathja Schroeder, Carolin Wodars, Andre Hein, Diana Hoppe, Ute Kaluza and Christine Fricke, who always gave my a helping hand. Wolfgang Tröger at Max-Planck Innovation, who always had a valuable advice when needed. Gisbert Mantei, the good soul of CFEL.

My thanks also go to all my PhD fellows within the International Max-Planck Research School for Ultrafast Imaging (IMPRS-UFAST). I had a wonderful time over the last few years. Thanks to our coordinators Anja Bleidorn, Sonja Utermann, and Julia Quante.

I also want to cordially thank Caroline Hahn, Frederike Ahr, and Nele Müller, who I met at the DESY Campus and spent valuable hours in my free time.

I am grateful to my old school friends Anja, Marina, and Amelie, who accompanied me more than half my life-time. You are fabulous and the best friends that anyone could wish for.

My deep gratitude goes to my whole family, including the Maierei, who always gave unconditional support. Especially, I would like to thank my parents, Monika and Hans, for their love.

I owe my deepest gratitude to my beloved husband Andreas Richard Maier, who is my greatest supporter and always believes in me.

Eidesstattliche Versicherung

Declaration on oath

Hiermit erkäre ich an Eides statt, dass ich die vorliegende Dissertationsschrift selbst verfasst und keine anderen als die angegebenen Quellen und Hilfsmittel benutzt habe.

I hereby declare, on oath, that I have written the present dissertation by my own and have not used other than the acknowledged resources and aids.

Hamburg, den

_____

Stephanie Maier